DIGITAL SHEAROGRAPHY FOR NONDESTRUCTIVE TESTING (NDT): DETERMINATION OF SMALLEST DETECTABLE DEFECT AND IMPROVEMENT OF ITS VISIBILITY

by

BICHENG GUO

A dissertation submitted in partial fulfillment of the
requirements for the degree of

DOCTOR OF PHILOSOPHY IN MECHANICAL ENGINEERING

2024

Oakland University
Rochester, Michigan

Doctoral Advisory Committee:

Lianxiang Yang, Ph.D., Chair
Gary Barber, Ph.D.
Marco Gerini Romagnoli, Ph.D.
Hejie Lin, Ph.D.
Lunjin Lu, Ph.D.

To my mother and father, I can't repay you for being wise, and for nurturing, you are always healthy and happy is my greatest wish. When the thesis is about to be completed, my mood cannot be calm. From the beginning of the project to the smooth completion of the thesis, how many respectable teachers, classmates, and friends have given me speechless help, please accept my sincere thanks here

ACKNOWLEDGMENTS

I am grateful for the advice of my supervisor, Dr. Lianxiang Yang, a respectable, reliable, and resourceful scholar. Thanks for providing me with valuable and dependable guidance in each stage of the writing in this thesis. Under his inspiring instruction, I completed my dissertation. His academic observation enlightens me not only in this thesis but also in my future study. Moreover, I want to thank all my committees who helped me understand the theory and result.

I would also like to thank all the professors of my academic committee, include Prof. Gary Barber, Prof. Marco Gerini Romagnoli, Prof. Hejie Lin and Prof. Lunjin Lu, for their academic advising, help and support.

Lastly, I would like to thank all my colleagues, professors, and facilities who supported me throughout my entire study at Oakland University.

Bicheng Guo

PREFACE

Digital speckle pattern interferometry (DSPI, also known as digital holography) and digital speckle pattern shearing interferometry (DSPSI, also known as digital shearography) are two examples of digital speckle interferometric measuring techniques. These methods are frequently used to find internal defects in a variety of fields, including aerospace, automative, and other technologies. The demands placed on materials are continually rising as technology advances. New materials must be stronger, tougher, lighter, have a greater strength-to-weight ratio, be flexible in design, resistant to fatigue and corrosion, and easy to mold. Based on that, the industry is gradually using metal alloy, glass fiber reinforced plastic (GFRP), and carbon fiber reinforced plastic (CFRP). However, the discovery of these materials is progressively emerging as a popular topic of conversation. Nondestructive testing is a relatively new technology adopted by industry. Among all Nondestructive testing (NDT) techniques, the DSPSI is widely accepted because of its benefits of high sensitivity, high precision, full-field measurement, non-contact, stable, and real-time. Digital shearography records the first order derivative of deformation. The anomalies and delamination information will form "butterfly" fringe pattern on the shearogram. Therefore, anomalies and delamination information will be visible and identifiable in the images captured using digital shearography. On the other hand, based on the theory of digital shearography and elastic thin plastic deformation theory, when the thin plate is made of isotropic material, the deformation relationship under large and small loads within the elastic range can be considered to be linear as well as the defects and delamination. However, the coefficients of these linear relationships are different from each other, the information of global deformation and defect information can separate.

The sensitivity and visibility of DSPSI observation would, however, be impacted in real-world applications by factors such boundary conditions, properties of material, magnitude of loading, loading methods, and the depth of defects. A comprehensive model needs to be established to pre-evaluate the depth and size of detectable defects that can be detected. It can be found that conventional research is researched under specific working conditions, such as only describing the technique related to one or two parameters, the specific test materials or the certain loading method. Based on that, a systematic and comprehensive analysis of the various parameters that affect the sensitivity of digital shearography is necessary to be established.

The first purpose of this doctoral thesis is to develop a comprehensive mathematical model to describe the sensitivity of digital shearography by combining the theory of elastic thin plate deformation and digital shearography with all of the parameters. In this part, the effect of the depth of the surface, size of the defect, the magnitude of the load applied to the specimen, the shape of the defect, and the boundary conditions on the sensitivity of digital shearography will be determined.

Secondly, based on this model, a novel experimental method was developed to improve the visibility of digital shearography. In this method, removing the information caused by global deformation and retaining the defect information to increase smallest detectable defect visibility. Also, conventional techniques for improving visibility of small detectable defects will first be analyzed, and the necessity of developing novel method will be discussed. According to the development process, global deformation is eliminated through novel approaches which are segmented fitting, the point coefficient method, and the surface coefficient methods. Based on that, after experimental verification, it was found that the point coefficient method is suitable for defect detection of specimens with uniform thickness, and the surface coefficient method is suitable for defect detection of complex deformation. The achievement of these two goals not only greatly improves the visibility of small detectable defect of digital sheaorgraphy, but also greatly reduces the cost of pre-testing and increases the application scope of digital sheaorgraphy. It also allows inexperienced engineers to quickly and clearly discover defect information. At last, this PhD dissertation solves the problems of undetermined mathematical models of digital shearography and effectively improves the sensitivity of digital shearography.

ABSTRACT

DIGITAL SHEAROGRAPHY FOR NDT: DETERMINATION OF SMALLEST DETECTABLE DEFECT AND IMPROVEMENT OF ITS VISIBILITY

by

BICHENG GUO

Adviser: Lianxiang Yang, Ph.D.

Sensitivity is a key parameter for using NDT technology. Determining what factors affect the sensitivity of NDT and establishing the model to facilitate engineers to select the appropriate system parameters and the loading magnitude are very important in the practical applications. In the past decade, Digital shearography has been widely used as a NDT tool for detecting delaminations and debonding defects in various composite materials, such as glass fiber reinforced polymer (GFRP), carbon fiber reinforced polymer (CFRP), Honeycomb structures, etc. Digital shearography is a laser interferometric technique and able to measure the first derivatives of deformation, i.e. strain information. It is suited well for NDT because defects generate strain concentration after a loading. As an NDT method, the sensitivity of digital shearography is an important parameter to measure the technology's defect detection capabilities. However, due to various limitations, the sensitivity research of digital shearography is still in its infancy. First, this technique lacks a numerical model to offer a theoretical foundation for determining the minimum detectable delamination/debonding limits and the detectable depth of defects. Secondly, because a shearogram is a fringe pattern which is composed

of both global deformation and defect information. smaller defect information is easily lost in the fringe patterns from global deformation. This research conducts in-depth study around determining the sensitivity of digital shearography and improving the defect visibility to meet the practical needs of helping engineers quickly select loads and quickly identify defects.

To solve these problems, the main research work and innovation results are as follows:

(1) In response to the first problem, this research presents a methodology of digital shearography for determining the size of the smallest detectable defect and its depth under various loading magnitudes for the purpose of nondestructive testing. First, a mechanical model based on the thin plate theory to calculate the expected bending of close-to-surface defects was proposed; the model built a relationship among the deformation caused by a defect, the size and the depth of the defect, as well as the load and the material properties. Second, the relationship between the relative deformation measured by shearography and the deformation induced by a defect was established based on the optimized shearing amount and the sensitivity of digital shearography. Based on these analyses, relationships between the size of the smallest detectable defect and the depth under different load amounts were established for different defect shapes.

(2) A demonstration of the sensitivity limit of digital shearography is shown on the basis of the sensitivity model, and the search for strategies to improve digital shearography is undertaken. After research, while keeping the

equipment consistent, the material unchanged, and the loading conditions the same, the best way to improve the sensitivity of digital shearography is to increase the contrast between defect information and background information. This method can make defects information clearer. Based on that, the second purpose was to examine methods for improving sensitivity found in previous studies and to discuss the advantages and disadvantages of all methods and developed the segment fitting method. According to the previous discussion, it can be found that the most common method is to make a fitting plane to represent the global deformation by unwrapping fringe pattern to build the continuous shearogram, and then subtracting the plane to increase the contrast. Secondly, the continuous shearogram of complex deformations makes it challenging to choose the fitting equation. Based on this, a piecewise fitting method is proposed. This method is based on the conventional fitting method, which is fitted based on the phase change between each fringes on the shearogram. Because the phase values between each fringe are linearly distributed, this method does need to consider the fitting equation selection. The new planes then need to be subtracted from the original image to remove the global deformation, thus preserving the defect.

(3) The second innovation of this research is the development of a practical and effective method to experimentally removes fringe patterns caused by the global deformation that makes small defects directly visible, which improves the non-destructive testing capabilities of digital shearography, thereby simplifying defect detection and visualization. For shearographic Non-

Destructive Testing (NDT), the phase distributions of two interferogram under different loads P1 and P2 are recorded. This novel approach involves recording one additional phase distribution of an interferogram at a load between P_1 and P_2, e.g. $P_{1'}$. Two phase maps of shearograms can be generated, corresponding to the two loads $\Delta_2 = (P_{1'}-P_1)$ and $\Delta_1 = (P_2-P_1)$, respectively. Because of the nondestructive nature of the testing, the magnitude of the loads P_1 and P_2 is small, and the 1st derivative of global deformation of the test part is assumed to be linear. Therefore, a linear coefficient C based on the two shearograms can be determined. The information from global deformation is then removed by subtracting the shearogram generated with the small load Δ_2 multiplied by the correlation coefficient C from the one obtained with the relatively large load Δ_1. This technique is further improved by calculating a complete surface linear coefficient C_{ij}, which improves the detail processing of the deformation of samples with complex geometry and mechanical properties.

Experimental verification was conducted based on specimens with prefabricated defects of different sizes and different loading conditions to verify the proposed mathematical model and experimental methods to eliminate global deformation. Experimental results show that the developed model can provide useful estimates for digital shearography NDT, and in particular can help test engineers estimate the size of the smallest detectable defect and the depth of the defect under corresponding load magnitude. Also, the experimental coefficient method can effectively evaluate a variety of structures and also be verified to remove global deformation, which improves defect detection capabilities and increases visualization of the digital shearography.

TABLE OF CONTENTS

TABLE OF CONTENTS—Continued

LIST OF FIGURES

LIST OF ABBREVIATIONS

CFRP	Carbon fiber reinforced plastic
GFRP	Glass fiber reinforced plastic
DSPI	Digital speckle pattern interferometry
DSPSI	Digital speckle pattern shearing interferometry
CCD	Charged-coupled Device
CMOS	Complementary metal–oxide–semiconductor
PZT	Piezo-electrical transducer
TPS-DS	Temporal Phase-Shift Digital Shearography
SPS-DS	Spatial Phase-Shift Digital Shearography
FT	Fourier transform
WIFT	Windowed Inverse Fourier Transform

CHAPTER ONE

INTRODUCTION AND SCOPE OF WORK

1.1 Introduction

The electrons in the atom take in energy and then go to a higher energy level, the energy will be released in the form of photons as the process of returning to a low energy level is being carried out. A laser is a device that emits photons in a beam with the advantage of excellent monochromaticity, excellent directionality, and excellent coherence during the laser possesses, due to the fact that the photon optical properties in this photon beam are extremely consistent. When a laser is used to irradiate the surface of an object, the information that is present on the surface of the object will be encapsulated in characteristics such as the phase intensity of the laser. In order to acquire information about the target, it is possible to process laser light that has been encoded with information using either mathematical or optical techniques. On account of this, lasers find widespread application in a variety of sectors, including measurement control and communications [1]. Lasers are utilized in a broad variety of measurement technologies, including wavefront interferometry, holographic interferometry, speckle measurement, and Moiré measurement which take advantage of the monochromaticity and good coherence of lasers. Conventional optical measurement technology [2] has steadily developed in the direction of equipment, automation, and economy in measuring instrument engineering. This development has been brought about by the introduction of new technologies, such as computer technology and new optical detectors, as well as new materials. Laser interferometry technology was developed on the basis of light wave interference due to the fact that lasers have excellent interference qualities. The phenomenon known as interference fringes occurs when two beams of light that have the same frequency, a constant phase difference, non-orthogonal vibration directions, and an optical path difference that is less than the coherence length meet in the same medium and overlap. In the area where the beams overlap, the light intensity is distributed according to a certain rule, and this distribution is identified as interference fringes. Laser interference technology is able to measure changes in characteristics such as displacement, length, and surface form [3], which is based on the idea of interferometry and uses a laser as a benchmark. It is advantageous in that it does not require contact, it is highly sensitive, and it is highly precise.

When it comes to industries like aircraft and aerospace, it is absolutely necessary to place all of the components that are manufactured through a comprehensive inspection and determine whether or not they are suitable for operational deployment before they are put into service. Additionally, honeycomb core sandwich composites and composites such as glass/carbon fiber reinforced plastic (GFRP and CFRP) have better strength-to-weight ratios, great resilience to corrosion and fatigue, and are utilized extensively in the aerospace and automotive industries. However, these sorts of materials are prone to producing disbonds between the inner core and outer skin for honeycomb structures and delaminations between the laminated layers for GFRP and CFRP as a result of impact loading, aging, defecty manufacturing, and other factors. Several non-destructive testing (NDT) techniques have already been utilized in order to check for defects [4-6]. Methods such as X-ray, near field millimeter wave, ultrasonic, and speckle pattern interferometry are examples of conventional non-destructive testing techniques. It is difficult for the industrial community to make use of the X-ray technology due to its size, cost, and the speed at which it measures. The near field millimeter-wave method is limited by the sensitivity of variations in the standoff distance, which makes it more suitable for testing low loss dielectric materials. On the other hand, the ultrasonic technique requires a scanning process that takes a significant amount of time. On the other hand, the optical approaches, such as thermography, holography, electronic speckle pattern interferometry (ESPI), and shearography, are becoming increasingly popular as potential candidates for new industrial non-destructive testing (NDT) tools due to the fact that they are non-contact, non-contaminating, and have a wide field of view [7-14]. Shearography is a whole field, extremely sensitive, and resilient laser-based approach for measuring deformation [14–16] which is also a technique that is used in conjunction with speckle pattern interferometry. A significant amount of progress has been made in the field of shearography during the course of the last few decades. Since it was first proposed in the 1970s, the utilization of digital shearography for the purpose of deformation measurements has garnered a significant amount of acceptance [16-18]. Consequently, shearography emerges as a suitable tool for non-destructive testing (NDT) of compound materials, which is a coherent-optical approach that is comparable to Holography and ESPI. Also, due to the fact that it directly measures strain information, digital shearography offers a number of benefits for industrial applications. (1) A rigid body movement generates a displacement, but no strain, thus, shearography is relatively insensitive to environment interruptions and it is more practical for industrial application; (2) defects in objects usually induce strain concentrations, thus, it is easier to reveal defects with strain anomalies than with displacement anomalies; (3) shearography uses a self-reference interferometric system which has low requirement for laser coherent length and enables the use of economical and practical diode laser or multi diode lasers if a larger area is inspected. Digital Shearography has become one of the most effective non-destructive testing (NDT) tools for composite materials, particularly honeycomb structures [19,20], due to the enormous advantages that it offers.

1.2 Development and research status of Digital shearography

Leendertz first presented the fundamentals of speckle interference in 1970. He stated that items with rough surfaces could be shot with a laser to create speckles, and that reference light could be introduced to record the patterns of speckle interference both before and after the object deforms. Speckle interference patterns before and after deformation can be compared to determine the object surface's deformation information. The Electronic Speckle Pattern Interferometer (ESPI), developed by Leendertz and Buttes in 1971, was utilized to process the speckle interference patterns that had been captured by cameras [21, 22].

Digital shearography (also known as shearography or Speckle Pattern Shearing Interferometry) was first proposed in 1973 by Leendertz and Buttes [23]. Digital shearography is distinct from electronic speckle interferometry in that it splits the light coming from the measured object's surface into two beams, shears one of them, leaves the other unprocessed, and then combines the two beams. On the camera's surface, they reconverge and create a speckle interference pattern. The deformation distribution information on the object's surface is obtained by comparing the variations in the speckle interference pattern before and after the item is deformed. Digital shearography is more resistant to interference from the outside environment since it is a self-interference technology that doesn't need the addition of extra reference light. This method was refined and a real-time digital shearography system (commonly referred to as a generation of shearography) was established in 1982 by Y.Y. Hong. This technology requires a wet chemical development procedure, yet it has very good resolution. However, digital shearography's practical applications are severely limited by this laborious technique.

Shearography from this era was also known as TV sheared speckle interference technology (also known as TV Shearography) after the 1990s since TV monitors were being used as display devices. To assess item strain in 1990, C. Joenathan used double-beam lighting, phase shift technology, and a TV camera to capture photos. The signal is recorded by speckle analysis method and shown on the monitor. By enabling real-time observation of the detection results, this technology expands its potential industrial applications. Nevertheless, the limited spatial resolution of this technology is a clear disadvantage that restricts the use of digital shearography.

As the time moved into the twenty-first century, CCD and CMOS camera technology advanced. Digital shearography that records images digitally and is digitized by two image acquisition devices [24]. Real-time computer visualization of the material deformation is possible by deducting the speckle intensity data captured by the camera which refers to this technique as the intensity method. Phase shift technology is introduced since the digital recording device digitizes the image, increasing the sensitivity of the digital shearography measuring system and simplifying its operation. This enables the development of user-friendly, industrial inspection-ready equipment based on the sheared speckle interference principle.

1.3 The purpose and significance of this research

Due to the superiority of digital shearography, the main application of this technology is to detect the debonding of honeycomb structures and the delamination of GFRP and CFRP composites [26-28]. Despite the many advantages of digital shearography, successful detection depends on the distribution of surface deformations caused by defects and minimal measurable deformation of the digital shearography. However, sensitivity and visibility of digital shearography is the often-discussed issues. Digital shearography sensitivity and visibility are used to describe the technology's ability to detect whether there are defects or delaminations in the specimen, as well as the minimum deformation caused by defects that can be monitored under fixed boundary conditions and loading conditions. The deformation caused by defects is a complex parameter related to loading size, loading method, shearing amount, defect size, depth, shape, etc. [29].

Over the past two decades, quite a few researchers have studied nondestructive testing of shear at different sizes and/or depths under different loading methods. E.C. Krutour, R.M. Groves, et al. In 2011, the modeling of the opto-mechanical measurement system, including the shear speckle meter, the loading technique and the response of the measured object, and the comparison of simulation results with experimental results were reported. This method is suitable for understanding the response of components under load and predicting anomalies such as defects [30]. The following year (2012), G. De Angelis et al. reported a new numerical experimental model to detect the size and depth of flat-bottomed holes in metallic and laminated composite structures through digital shearography based on the dynamic response of defects to applied stress [31]. Another numerical experimental model for testing defective materials using digital shearography based on thermal loading was reported by D. Akbari et al. 2013[32]. X. Chen et al. reported a hybrid approach based on experimental and computational studies using digital shearography results and finite element analysis software and/or Matlab to predict internal defects. (2015), Y. Fu et al. (2017) and J.F. Vandenrijt et al. et al. (2019), respectively [33-35].

Along with these considerations, the first objective of this PhD dissertation is to create a mathematical model by merging the theory of elastic thin plates deformation with the theory of digital shearography. The digital shearography is used in this model to quantitatively illustrate the relationship between the size and depth of the lowest detectable defect in non-destructive testing of various magnitude of loads. This relationship is examined in relation to the size of the defect. Deformation differential equations and deformation solutions for various defect forms under specified boundary conditions are utilized in this process. In order to ascertain the precision possessed by the model, experiments based on vacuum loading were carried out. Within this model, comprehensive numerical equations are constructed for the purpose of determining the size of the smallest detectable defect as well as the depth based on the minimum measurable deformation or relative deformation of the digital shearogram.

After gaining an understanding of the visibility and sensitivity of digital shearography through the modelling process, it is possible to identify the smallest defect that can be detected. Furthermore, it is important to note that the presence of internal defects in the material create an unequal deformation of the specimen when the material is subjected to load. In particular, this non-uniform deformation takes place in close proximity to defects, which provides vital information regarding the characteristic and properties of the defects. In shearographic Non-Destructive Testing (NDT), defects are found by identifying anomalies in the surface deformation caused by internal defects under a small load. Because shearography measures the first derivative of the deformation, these defects generate butterfly fringe patterns on the surface. Also, the butterfly fringe pattern is often masked by global deformation for small defects, which result Furthermore, for small defects, the butterfly fringe pattern is often masked by the overall deformation, which makes it more difficult to find and detect the defects. It is important to note that the key to successful detect defect by digital shearography is to increase the contrast between information from defect-induced deformation and global deformation. As long as the defect signal is large enough to be detected (for example, the ratio of defect signal to background signal is greater than 2), defect visualization is straightforward. The technological requirements are particularly severe as a result of this limitation, and operators are required to possess significant capabilities in order to validate the location of the defect. In order to accomplish this, it is necessary to discover a technique that may enhance the sensitivity and visualization capabilities of digital shearography under fixed conditions [34-36].

Therefore, in order to increase the sensitivity of digital shearography and its visibility to express defect information, it is necessary to find a method to extract defect information. There are two main methods for extracting defect information. One approach is to minimize noise to improve the clarity and effectiveness of information expression. Another approach is to eliminate global deformation to enhance the visibility of defect information. Current noise reduction research exploits spatial deformation for second-, third-, and fourth-order differentiation to reduce noise and improve defect diagnosis. Lopez et al. used numerical differentiation in phase diagrams to reduce noise through stroboscopic illumination or intensity modulation [37]. However, this approach may exclude higher frequency signal components or integrate them into the global deformation data, resulting in incomplete and potentially misleading information. Furthermore, with this approach, as the number of fringes increases, it becomes increasingly challenging to determine the center location of a fringe compared to determining its edge.

On the other hand, the main and most popular method is through remove the global deformation and retain the defect information to increase the defect visibility. In this direction, several approaches have been used across various domains to reduce global deformation. The key strategy is to create a simulated surface representing the information caused by global deformation of the sample. This can be obtained by (a) fitting a surface to the unwrapped shearography data without defects, (b) using the same loading on a defect-free reference object, or (c) using finite element modeling. An increasingly popular alternative approach (d) relies on machine learning to identify the difference between information from global deformation and defects. After that, the global deformation is separated with defect information. Then, by subtract the global deformation information, the global deformation is then removed, and a surface representing the defect information is constructed [38-48]. Tao uses Abaqus displacement data to create a fitted plane of global deformation. Establishing a connection between the experimental data and the fitted plane can eliminate the global deformation [43]. Deepan adopts B-spline interpolation technique to construct the fitting plane [44]. Fomitchov conducted an experiment where a replacement reference plate was inserted into the device to replace the initially defective plate to simulate global deformation [45]. Tao used polynomial fitting as a means to perform similar phase correction, with the aim of optimizing the image of the sample by reducing defects and minimizing errors [46]. A drawback of this approach is the need to refer to the damage panel to extract defect deformations. This process may generate additional errors, which may result in the inadvertent loss of defect information and impossible for practical application. Additionally, the act of capturing two images simultaneously results in a reduction in camera resolution. Another approach involves comparing defect information with plane information and then using machine learning techniques based on this theoretical framework. With extensive training, defect information can be obtained more accurately. Hofmann et al. The contrast-to-noise ratio method was optimized to quantitatively assess the contrast between defects and image background [47]. However, this method requires a large amount of experimental data, requires extensive mechanical training, and is only effective for a single type of material. Since the above methods have certain limitations, the polynomial regression equation fitting method has become the simplest and most commonly used method. Templeton [48] constructed a fitting plane through a polynomial regression function. This method aims to reduce the global deformation effect by subtracting the regression curve fitting plane from the deformation plane.

Therefore, the second core point of this article is to extract defect information by removing global deformation so that it can be expressed more clearly. In this part, the research addresses the issues presented in conventional approaches. Firstly, all previous methods rely on a continuous phase map obtained after unwrapping: a continuous phase map often reduces the contrast between defect and background information, making smaller defects harder to detect. Secondly, the continuous phase map may be irregular under complex deformations, complex surface fitting or interpolation processes difficult to execute. Lastly, the use of machine learning techniques can help remove the information from global deformation, but this approach requires the collection of large amounts of data, and its application is often limited to the substrate material used for model training. In contrast, this proposed novel approach for the removal of the information from global deformation is quick, practical, and broadly applicable: it relies on the direct analysis of a shearogram. For example, if the resolution of the hardware is 8-bit, which is composed of multiple fringes with gray levels varying from 0 to 255, each fringe will have the gray level range between 0 to 255, while the continuous phase map is 0 to 255 for whole map, thus the shearogram can display more detailed information. Based on that, this work presents an efficient and practical methodology that preserves only defect information after experimentally eliminating fringe patterns associated with global deformation in digital shearography. This approach records the phases of relatively large and small loads within the elastic deformation in the same loading process, it records one more phase map than conventional digital shearography. When compared to the conventional global deformation elimination technology, this approach eliminates errors brought about by different loading processes and different specimen selections. Since the measurement is performed during the elastic deformation stage, the deformation amount of the specimen has a linear relationship. Therefore, the linear coefficients based on two shearograms can be determined through the relationship between loading and 1st of deformation. After that, the coefficient “c” of the defect and coefficient “C” from the global deformation can be obtained which are different from each other. The relatively large load global deformation phase map without defect information is obtained by multiplying the small load shearogram with “C”. The global deformation is then removed by subtracting the image using the original relatively large load shearogram. This method not only improves image quality and reduces errors caused by sample replacement, but also verifies the feasibility of the experimental method. In addition, this method reduces the difficulty for engineers to find defects and improves work efficiency.

1.4 Dissertation structure arrangement

The first chapter of this dissertation provides an overview of the background and development of digital shearography briefly. The background information and completed research justify the need for this paper’s research. The relationship between the sensitivity of the digital shearography technique and defect-induced deformation is briefly described, and the contributions made by other researchers in this field are discussed. A novel mathematical model was created to explain how different parameters affect digital shearography's sensitivity. Next, how to increase digital shearography's sensitivity which includes its capacity to exhibit defects under specific working conditions will be go over. Based on the work of previous researches and technique for image processing technique in this field, this paper proposes a novel technique to reduce the error rate and enhance the representation of defect information, namely the experimental coefficient method.

The fundamental theory of digital shearography is presented in Chapter 2, which introduces the history, fundamental principles, and practical uses of laser speckle of digital shearography. Additionally, the fundamentals of phase shifting technology, which are reviewed, and temporal phase shift technique are described in more detail.

In order to illustrate the connection between the sensitivity of shearography and the deformation brought on by defects, the elastic thin plate deformation theory is explored in the third chapter in conjunction with the theory of shearography. This chapter discusses the force, moment, strain, stress, and other variables in all directions of the thin plate during elastic deformation. The Sophie Germain equation is produced by introducing Hooke's law and the notion of network plane. Conversely, under fully constrained boundary conditions, the elastic deformation of thin plates of various forms is investigated and inferred. Because the anomalies deformation measured by digital shearography can be regarded as a thin plate, and its deformation is minimal under fully constrained boundary conditions, if digital shearography can measure defect information under this boundary condition, the defect can also be detected under other boundary conditions.

The smallest observable defect's size and depth are determined and demonstrated using a comprehensive mathematical model developed in Chapter 4. This comprehensive mathematical model was used to establish the relationship between the minimum defect size under certain conditions and the sensitivity of shearography. The relationship between loading size, the defect's shape, depth of the defect, properties of material, and shearography's sensitivity are also covered in this chapter.

Based on the findings of Chapter 4, Chapter 5 enhances the visibility of digital shearography and creates an algorithm to remove global deformation. Firstly, the conventional approach to removing global deformation will be examined and explained.

The pros and cons of the conventional approach will be also examined and discussed. Furthermore, a segmented fitting method based on the conventional fitting method is developed to remove global deformation. By fitting the fringe pattern based on pixel values, this approach creates a fitting plane. To eliminate the global deformation, the image is then removed from the original fringe pattern.

The experimental coefficient approach is described in Chapter 6 as a means of removing global deformation. This novel point coefficient method removes global deformation information by recording the phases of relatively large and small loads within the elastic deformation in the same loading process, it records one more phase map than conventional digital shearography. When compared to the conventional global deformation elimination technology, this approach eliminates errors brought about by different loading processes and different specimen selections. Furthermore, the point coefficient method is suggested based on this approach to detect the defect information in homogenous thickness specimen. This technique helps to improve and magnify the information of defects. The purpose of this project is to increase the efficiency and precision of digital shearography in identifying defects or delamination in various materials. The surface coefficient approach is also proposed due to the rise of complex deformation scenarios and the presence of noise. Using this technique, the coefficients for the complete surface can be obtained. Compare to the point coefficient method, surface method is suggested to applied in removing global deformation under complex deformation conditions.

Chapter 7 concludes with a summary of the entire work and looks ahead.

CHAPTER TWO

WORK BASIC THEORY OF DIGITAL SHEAROGRAPHY

2.1 Review of shearography methodology

The stringent criteria for product quality and dependability have resulted in the requirement for a Non-Destructive Testing (NDT) method that is very effective, operates in real time, covers the entire area, and does not involve any contact being made [49]. Optical methods, which include thermography, holography, electronic speckle pattern interferometry (ESPI), and shearography (also known as speckle pattern shearing interferometry), are becoming increasingly attractive as potential candidates for new industrial non-destructive testing (NDT) tools. This is due to the fact that these optical methods are non-contacting, non-contaminating, and have a wide field of view. ESPI is one of the optical techniques that has been identified, and it is well-known for its ability to quantify tiny deformations. One of the capabilities of ESPI is the ability to provide a whole field deformation measurement of a test object in many dimensions while maintaining an exceptionally high level of measurement sensitivity. On the other hand, ESPI has stringent requirements for the environment in which measurements are taken, such as the isolation of vibrations and the regulation of temperatures. Because of these restrictions, the uses of ESPI are restricted to only laboratory environments. It is necessary to have an optical technology that is both more resilient and easier to apply in order to fulfill the criteria of the industrial applications in the field. In situations like this, ESPSI will be an another way can be selected. ESPSI is a coherent-optical measurement and testing method that is comparable to ESPI. However, because to its relative insensitivity to other environmental disturbances, ESPSI offers a number of benefits that are particularly useful for industrial applications. Digital shearography measures the gradient of deformation rather than the deformation itself as monitored by ESPI. The direct measurement of strain information that ESPSI provides is the reason why shearography is becoming an increasingly essential non-destructive testing (NDT) tool in the industrial sector.

Leendertz and Butters were the first to disclose the foundations of speckle pattern shearing interferometry in 1973 [50]. Shearography was subsequently accepted as the term associated with this technique. This method was further enhanced by Y.Y. Hung in 1982, when he constructed a shearography system that was suitable for practical use [51]. It was after the publication of a number of good results that the shearography approach started to gain an increasing amount of attention from both the academic sector and industry. This led to the rapid growth of technology in the decades that followed. From the year 1982 up until the present day, there have been three generations of shearography, which are characterized by recording devices: Shearography may be broken down into three generations: the first generation, which consists of photographic shearography from 1980 to 1990; the second generation, which includes television shearography, also known as electronic shearography, from 1990 to 2000; and the third generation, which includes digital shearography from 2000 to the current day. As the recording medium, the first generation of shearography, also known as photographic shearography, makes use of either thermoplastic emulsion, which is reusable, or photographic emulsion, which is not reusable. Both of these types of media have a resolution that is extremely high. On the other hand, photographic shearography necessitates a wet chemical development procedure that is both time-consuming and laborious, which significantly restricts its testing speed and application. The second generation of shearography, known as TV shearography, is characterized by the utilization of analytic video cameras as recording devices and the utilization of a television monitor as the display device. Once the optical wave front has been converted into an analytical signal, it is then presented on an analytical monitor. This process is known as TV shearography. This approach makes it possible to display the sharographic measurement result in real time, which expands the range of uses that this technique can potentially have in the industrial sector. Due to the fact that video cameras have a lower spatial resolution than their photographic counterparts, the spatial resolution of TV shearography is significantly lower than that of photographic shearography. The third generation of shearography, known as digital shearography, makes use of a digital camera as the recording device. This camera is often a Charge-Coupled Device (CCD) camera or a Complementary Metal Oxide Semiconductor (CMOS) camera. Through the utilization of digital recording equipment, the image is converted into a digital format. This makes it possible to implement a phase-shift approach, which has the potential to boost the measurement sensitivity of shearography devices by a factor of 10.

Because strains are a function of displacement gradients, shearography is a technique that directly measures displacement gradients. Consequently, digital shearography provides information regarding strain in a direct manner. As a detection tool, it is more practical than other nondestructive testing procedures, and strain anomalies are easier to identify than displacement anomalies compared to ESPI. This is due to the fact that defects in objects typically create strain concentrations. Furthermore, due to the fact that rigid-body motion does not result in strain, shearography is considered to be insensitive to such motion, which eliminates the requirement of utilizing specific devices for vibration isolation. Shearography is useful in ordinary industrial activities, as demonstrated by this significant advantage, which demonstrates the effectiveness of shearography. The most important applications of digital shearography are non-destructive testing (NDT) and the numerical determination of the out-of-plane term dw/dx (in the x-shearing direction) or dw/dy (in the y-shearing direction) [52-69]. Recently, the business sector has voiced a growing demand for the rapid detection of defects in real time.

In spite of the fact that shearography is capable of directly measuring first derivative of deformation, the shearogram typically includes both in-plane and out-of-plane components. This means that the application of shearography for strain measurement in industry is still restricted. It is possible to obtain the pure out-of-plane component dw/dx (or dw/dy) by performing a certain alignment of the beam that is utilized for illumination. On the other hand, it is not possible to determine the pure in-plane strains du/dx (or dw/dy) by relying solely on the alignment of the illumination angle. For the purpose of measuring the components of the two-dimensional deformation tensor (du/dx, du/dy, dv/dx, and dw/dy), a few researchers have attempted to illuminate the surface of the object in a direction that is almost parallel to itself. On the other hand, the findings that were obtained are only applicable to certain working conditions [63-65]. In 1996, Steinchen and Yang reported that the application of two independent illumination beams made it possible for the first time to utilize shearography to measure the pure in-plane components du/dx, du/dy, and dw/dx, dw/dy that were formed by general loadings which was the first time that shearography was used to measure these components. In this article, a novel method is provided that makes use of also use temproal phase-shift digital shearography to accomplish the successful measurement of strain directly. Pure in-plane strain as well as out-of-plane strain may be directly measured using this method, and the measurement can be taken from a single speckle pattern image. When this occurs, the measuring speed of phase-shift digital shearography is no longer restricted by the phase-shift steps; rather, it is solely constrained by the capabilities of the image sensor. Because of this, it is now able to do whole field, direct strain measurement while dynamic loading is being applied thanks to the utilization of an ultra-high speed CCD camera.

2.2 Principle of digital shearography

Expanding the laser beam and projecting it onto the surface of the rough item in order to create speckles is the fundamental principle behind the measurement technique known as sheared speckle interference technology. A reflection of the speckle light is produced by the surface of the item that is being measured, and the light that carries the information about the speckle is then transmitted through the imaging lens to the camera image plane of digital shearography. By passing the light through the dichroic prism, the identical beam of light is split into two equal beams, and the reflector is responsible for reflecting both of these parts. The light that is reflected by one of the mirrors is used as the reference light, and the light that is reflected by the other mirror is deflected by the other mirror, which results in the introduction of a shear amount. On the surface of the image capture equipment, the two beams of light will interfere with one another, which will result in the formation of a speckle interference pattern. It is possible to gain information regarding the distribution of the surface deformation of the item that is being measured by studying the changes that occur in the speckle interference pattern both before and after the deformation. Initially, the sheared mirror was utilized in order to induce shearing amount in the shearing system. On the other hand, the magnitude of shearing amount that was produced by this technology, was problematic to modify. Altering the tilt mirror angle of the sheared mirror was necessary in order to make the necessary adjustments to the shearing amount. In the present day, the shearing systems that are most frequently utilized are the Michelson shearing system, the Mach-Zehnder shearing system, and other similar systems [70].

In most cases, the deformation of the surface of the item that is being measured may be broken down into three distinct directions of deformation: the X and Y directions within the plane, and the Z direction out from the plane [71, 72]. Shearography is mostly utilized for the purpose of determining the out-of-plane deformation distribution information in the Z direction of the surface of the item that is being measured. However, when two laser beams of different wavelengths are utilized to illuminate the object under test from various directions, mathematical processes can also be used to determine the in-plane deformation information of the object under test through phase diagrams. This is possible since the laser beams are illuminated from different directions.

In the next Figure, Figure 1.1, a representation of the measurement principal diagram of the conventional Michelson digital shearography system will be found, which is used to measure out-of-plane deformation. The digital shearography system will receive the speckles that are produced as a result of diffuse reflection when the laser is used to irradiate the rough surface of the object that is being measured. By tilting mirror 1 at a very small angle, the system can cause two non-parallel rays of light scattered from two adjacent object points (P_1 and P_2) to interfere with each other. As the object surface is diffusely reflective, the interference of the scattered rays yields a random pattern known as speckle pattern.

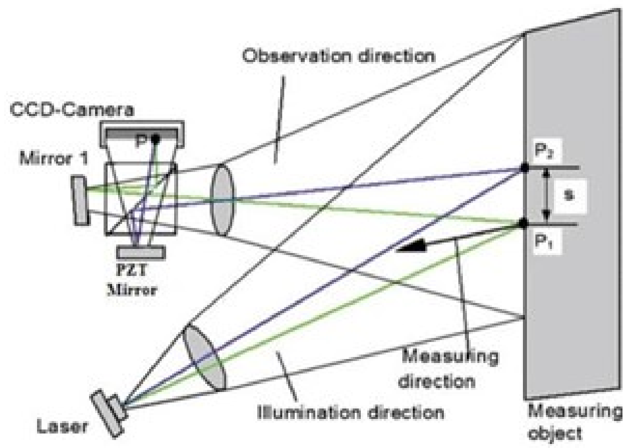

Figure 1.1 Schematic of ESPSI

In digital shearography, the light waves reflected from two points on the surface of an object are sheared by tilting the angle of the mirror. The recorded intensity is digitized and stored in the computer. The following exponential function can describe the wavefronts of the two points.

$$U_1 = a_1 e^{i\theta_1} \tag{1.1}$$

$$U_2 = a_2 e^{i\theta_2} \tag{1.2}$$

In equations (1.1) and (1.2), θ_1 and θ_2 respectively represent the random phase angle of the light wave from the surface point of the object, and a_1 and a_2 are the light amplitudes. Therefore, the total light field on the image plane is:

$$U_{tot} = U_1 + U_2 = a_1 e^{i\theta_1} + a_2 e^{i\theta_2} \quad (1.3)$$

Afterwards, using the intensity after loading minus the absolute value of the intensity before loading, the interference fringe pattern related to the change in relative phase difference Δ can be obtained. The process is shown in Figure 1.2, and the interference fringes are shown in Figure 1.3.

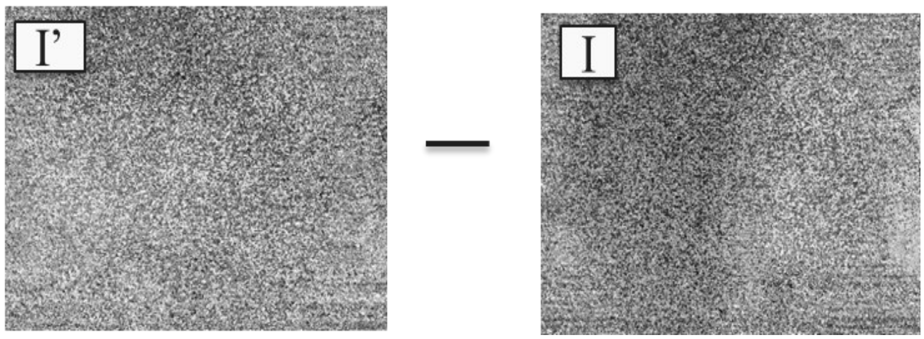

Figure 1.2. Intensity subtraction

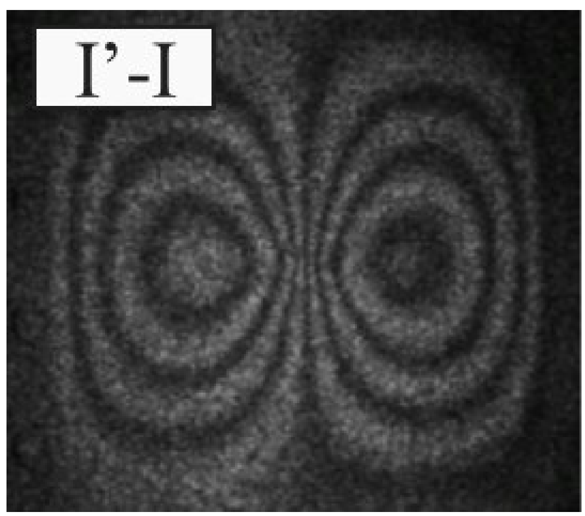

Figure 1.3 ESPSI Interferometric fringe pattern

The intensity can be expressed by:

$$I = U_{tot}U_{tot}^* = (a_1e^{i\theta_1} + a_2e^{i\theta_2})(a_1e^{-i\theta_1} + a_2e^{-i\theta_2}) \tag{1.4}$$

$$I = (a_1{}^2 + a_2{}^2) + 2a_1a_2Cos(\theta_1 - \theta_2) = A + BCos（\varphi） \tag{1.5}$$

In equation 1.4 and 1.5, $\mathbf{U_{tot}}^*$ is is the complex-conjugate of $\mathbf{U_{tot}}$ and $\boldsymbol{\varphi} = \boldsymbol{\theta_1} - \boldsymbol{\theta_2}$. After deformation, the intensity can be expressed as:

$$I = A + BCos(\varphi + \Delta) \tag{1.6}$$

From Figure 1.1, the fringe pattern can be obtained by subtraction of the absolute value of the intensity, as shown in the following equation:

$$|I_s| = |I' - I| = B|Cos(\varphi + \Delta) - Cos(\varphi)| \tag{1.7}$$

Where $\Delta = \mathbf{2n\pi}$, (n=0, 1, 2, 3...). When $\mathbf{I_s} = \mathbf{0}$, the fringe pattern will change from bright to dark. The relative phase difference Δ before and after loading can be expressed as:

$$\Delta = (\varphi_1' - \varphi_2') - (\varphi_1 - \varphi_2) = (\varphi_1' - \varphi_1) - (\varphi_2' - \varphi_2) = \Delta_1 - \Delta_2 \tag{1.8}$$

In equation (1.8), $\boldsymbol{\varphi_1}$ and $\boldsymbol{\varphi_2}$ are the phase difference of the two beams before loading, and $\boldsymbol{\varphi_1'}$ and $\boldsymbol{\varphi_2'}$ represent the phase difference of the two beams after loading. The first derivative of deformation of can be evaluated by the relative phase difference.

$$\Delta = \Delta_1 - \Delta_2 = \frac{2\pi}{\lambda}(\sin(\alpha) * \delta x + (1 + \cos(\alpha)) * \delta w) \tag{1.9}$$

If the angle between the illumination direction and the observation direction of the CCD-camera is equal to or close to zero, then the relationship between the relative phase change and the strain components can be expressed as equation (1.10). In equation (1.9) and (1.10), there are no in-plane terms ($\frac{\partial \mathbf{u}}{\partial \mathbf{x}} = \frac{\partial \mathbf{u}}{\partial \mathbf{y}} = \frac{\partial \mathbf{v}}{\partial \mathbf{x}} = \frac{\partial \mathbf{v}}{\partial \mathbf{y}} = \mathbf{0}$), which means only out-of-plane deformation occurs as the shearing is applied along the x-direction.

$$\Delta_{x} = \frac{4\pi\delta x}{\lambda} * \frac{\partial w}{\partial x} \tag{1.10}$$

2.3 Speckle interference pattern phase extraction technology

The phase change is precisely measured in a method that utilizes digital shearography. It is possible to obtain the out-of-plane deformation of the surface of the item that is being measured by measuring the phase change that occurs on the surface of the object that is being measured [9]. As a result, one of the most important aspects of the technique known as speckle interferometry is the process of collecting phase information from the speckle interferogram. Various technologies for phase extraction include the following approaches: intensity real-time subtraction technology, temporal phase shift technology, multi-channel spatial phase shift technology, and spatial carrier technology, which are the ways that are most widely employed.

Through the process of subtracting the grayscale values of the phase image that was acquired by the camera, it is possible to generate a fringe that resembles a butterfly fringe pattern. In addition to being easy to compute and quick, this method allows you to directly view the distribution of the deformation of the object that is being measured within the software package. On the other hand, the edge resolution obtained is not very good since the method does not handle and eliminate different noise defects present in the image being processed. In spite of the fact that certain image processing techniques are utilized in order to eliminate some noise from the acquired butterfly fringe pattern, it is still possible that some new errors will be introduced throughout the process of eliminating noise from the image. For example, in the case of filtered fringes, the fringe pattern may be different from the fringe pattern that originally existed. There is a change in the phase distribution information as a result of the fringe pattern's position shifting. Due to this reason, this method is typically only utilized for qualitative identification when defect detection is being performed.

Obtaining the phase is often accomplished through the use of either time phase shift technology or spatial phase shift technology. This is done in order to generate butterfly fringe patterns of lower quality. When compared to the other technologies, the temporal phase shift technology is distinguished by its utilization of error averaging in time and in the real measurement system. Additionally, the aperture is quite large, and the camera collects more information, resulting in improved fringe quality. The multi-channel spatial phase shift technology and the spatial carrier technology are both included in the classification of spatial phase shift technology. Quick detection is one of the advantages that multi-channel spatial phase shifting technology possesses among these technologies. However, because of its convoluted optical path, difficult adjustment, and expensive device cost, implementation of this technology is extremely uncommon in practice. In order to directly extract the phase information from an image, the spatial carrier technology makes use of the Fourier transform technology. As a result, the number of images that are required to obtain the phase information is reduced, the detection speed of the system is increased, and it is more commonly utilized in real-time defect detection at industrial sites.

The temporal phase shift technology, the multi-channel spatial phase shift technology, and the spatial carrier technology will be the primary topics of discussion in this part which are the technologies that are utilized in actual measurements the most frequently.

2.3.1 Temporal Phase shift technique

The temporal phase shift technique is the phase extraction method that is utilized the most frequently in sheared speckle interference phase extraction. It also offers the highest accuracy of phase extraction outcomes. In this technique, a fixed phase value is successively introduced to the image that is being captured on the surface of the camera, and then the image is collected while the item being measured remains relatively unchanged. This method was initially proposed by Carré in the year 1966, and Bruning was the one who introduced it into the field of optical detection. At the moment, the approach that is utilized the most frequently is the one in which a piezoelectric ceramic (PZT) is connected to a mirror in the shearing section. The movement of the piezoelectric ceramic is controlled by the introduction of a predetermined voltage, which results in the introduction of a fixed phase shift value. The piezoelectric ceramic drive device provides a number of benefits, including a high displacement resolution, a quick reaction, a small size, a relatively low price, and the absence of heat generation. Specifically, it is a substance that is capable of transforming mechanical energy and electrical energy into equivalent forms. Because its single-step displacement can reach the nanoscale level, it has been widely used in the introduction of phase shift in digital shearography [73] which has led to its widespread application.

A typical Michelson-based digital shearography that makes use of piezoelectric ceramics to introduce a temporal phase shift is depicted in Figure 2.1, which may be found below that. In order to illuminate the object, a laser beam that has been extended with the help of a beam expander is used. It is the digital shearography that receives the reflection of speckles that are caused by diffuse reflection from rough surfaces. In the digital shearography, a mirror causes a tiny deflection in order to introduce the shearing amount and control the direction in which the shearing occurs. A new speckle pattern is created on the surface of the camera target as a result of interference from two diagrams that are not aligned properly. Through introduced the computer algorithm, the voltage that is delivered into the piezoelectric ceramic may be controlled, then, the piezoelectric ceramic is connected to one of the mirrors.

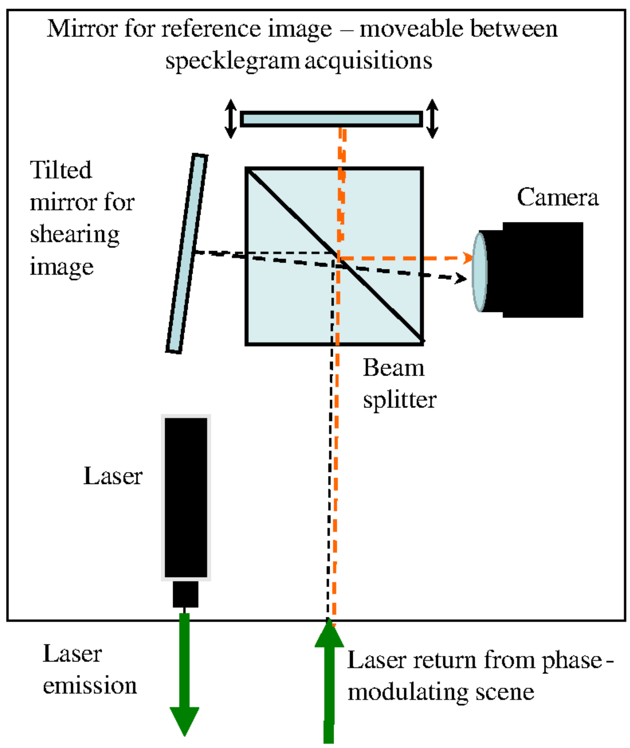

Figure 2.1 Michelson-based time phase shift digital shearography system

The phase distribution of the object's deformation can be derived by subtracting the phase images that were taken before and after the loading process. In the temporal phase shift technology, the phase diagram of the item that is being measured both before and after loading is frequently acquired by means of a phase shift algorithm that consists of multiple steps. The three-step phase shift method, the four-step phase shift algorithm, and the five-step phase shift algorithm are all examples of phase shift algorithms that are often employed. Both the three-step phase shift algorithm and the four-step phase shift algorithm are utilized in practice on a somewhat regular basis [10, 74]. The following is primarily an introduction to the fundamentals of three-step phase shift and four-step phase shift.

2.3.1.1 3+3 temporal phase shift technique

According to the previous expression, each three-step interference pattern collected by the camera can be expressed by the following equation (1.5).
Here, I (x,y) is the intensity value of the speckle pattern recorded by the camera. φ (x,y) is the unknown phase difference between two mutually sheared lights, also A and B are also unknown parameters. As can be seen from the above equation, in the obtained speckle interference intensity map, in addition to the known light intensity, there are three unknown parameters, so at least three equations are needed to solve it.

By introducing multiple $\frac{2}{3}\pi$ into one of the two mutually sheared light beams, a series of speckle pattern intensity values with different phase values can be obtained. Each phase shift amount is: 0, $\frac{2}{3}\pi$, $\frac{4}{3}\pi$, then the speckle interference pattern collected by the camera can be expressed as:

$$\begin{aligned} I_1 &= A + B\mathrm{Cos}(\varphi) \\ I_2 &= A + B\mathrm{Cos}(\varphi + 120^{o}) \\ I_3 &= A + B\mathrm{Cos}(\varphi + 240^{o}) \end{aligned} \tag{2.1}$$

Moving the piezoelectric ceramic by a certain amount of displacement is what brings about the introduction of the phase quantity that is already known. Since the piezoelectric ceramic is responsible for controlling the moving distance of the reflector, the optical path of the light reflected by the reflector changes, and a specific phase amount can be introduced at this time. In this case, it will take, $\alpha = \frac{2}{3}\pi$, which will allow us to obtain the displacement value that the matching piezoelectric ceramic should vary.

By using the equations shown above, it is able to determine the phase value of the speckle interference pattern that is produced when two photons that are sheared in opposite directions interact with one another on the surface of the camera target by equation (2.2).

$$\varphi = \frac{\sqrt{3}(I_3 - I_2)}{2I_1 - I_2 - I_3} \tag{2.2}$$

Loaded and measured the object, and use the same method to introduce multiple, $\frac{2}{3}\pi$ and collect the interference results respectively. Calculate the collected image groups to obtain the relative phase value φ after the object is deformed, and compare the phase values of the object under test before and after deformation. By subtracting, the deformation phase distribution of the measured object can be obtained, which is shown in Equation 2.3.

$$\Delta = \varphi' - \varphi \tag{2.3}$$

<u>2.3.2. 4+4 temporal phase shift technique</u>

The four-step phase shift algorithm is currently the most commonly used temporal phase shift algorithm due to its simple calculation and high quality of calculation results. The basic principle is similar to the three-step phase shift algorithm. When the measured object remains stationary, the phase shift amount introduced to the measured object each step, the phase shift amounts of each step are: 0, $\frac{1}{2}\pi$, π , $\frac{3}{2}\pi$. According to the content of the previous section, it can be known that the speckle interference pattern collected each time can be expressed as:

$$\begin{gathered} I_1 = A + B * \mathrm{Cos}(\varphi) \\ I_2 = A + B * \mathrm{Cos}(\varphi + 90^o) \\ I_3 = A + B * \mathrm{Cos}(\varphi + 180^o) \\ I_3 = A + B * \mathrm{Cos}(\varphi + 270^o) \end{gathered} \tag{2.4}$$

The piezoelectric crystal (PZT) mirror is the key to realizing the phase shift necessary to introduce the known additional phase [9]. Then, after four phase shifts, the phase difference can be calculated as:

$$\varphi = \arctan\frac{I_4 - I_2}{I_1 - I_3} \tag{2.5}$$

After deformation, another four phase-shift steps and four speckle pattern images are taken, and the phase difference after deformation can be found. The relative phase change due to deformation can then be calculated using $\Delta = \varphi' - \varphi$. Then, the deformation gradient can be evaluated using the phase-deformation relationship.

2.3.2 Spatial Phase shift technique

According to the previous section, in order to obtain information about the surface deformation of the measured object, fixed phase shift values multiple times while the measured object is stationary will be introduced in digital shearography. However, in actual detection, the state of the object under test may change in real time. In this case, using temporal phase shift technology may produce large errors. The spatial phase shift technology continuously introduces a certain phase shift value to the light reflected by the measured object in spatial [76-79]. It only needs a single image to perform Fourier transform on the image and obtain it from the Fourier transform. The phase information on the surface of the measured object is calculated from the results. Therefore, the spatial phase shift technology can be used to obtain the deformation information of the measured object when the measured object dynamically transforms [80]. Spatial phase shift technology can be subdivided into two major categories: multi-channel spatial phase shift technology and spatial carrier technology. Spatial carrier technology will be mainly introduced because of its wide application.

Frequency carrier technology is a conventional technology that has been used in the telecommunications field for many years. The signal information carried is usually modulated by a high-frequency carrier frequency in these applications. The frequency carrier spatial phase-shift method provides higher spatial resolution because it does not require dividing the recorded image into sub-images. Along with these considerations, the spatial phase-shifting process has become the primary trend of future development in digital shearography. In the frequency carrier spatial phase-shift method, the Fourier transform and Windowed Inverse Fourier Transform are two key points to convert the image from the spatial domain to the Fourier domain and back to the time domain.

The Fourier transform (FT) is helpful in decomposing images into trigonometric components (sine and cosine). This tool utilizes the capacity to describe virtually all components in the world through waveforms as a function of space, and time among other variables. The sum of simple sinusoidal is used to mathematically describe different wave functions in the universe. With specific modifications, the Fourier transform is used to mathematically decompose and deconstruct signals from deformities into their sinusoidal components will describe in the following section. FT has been used to separate the spectra on spatial domain frequency in advanced phase-shift techniques.

Then, the Window Fourier transform will also be described, which transfers the information back to the time domain. As mentioned in the FT description, it provides a wave signal representation for multiple global functions. The effectiveness of WIFT is based on an analysis of a select portion of the signal that comes from an object. According to the studies of Dr. Tauler and Walczak, interesting local information is a part of the whole field information. The WIFT is applied to extract this part signal through a window function g(t) [76]. The WIFT can be shifted to other locations of the field of view to cover all the desired time domains. The significant role played by the WIFT in the development of phase-shift measurements shall thus be evaluated alongside the further developments in shearography in the subsequent sections. For example, the paper applied a Mach-Zehnder from Dr. G Pedrini in Figure 2.2 as an example. [81]. In this setup, the light beam from the laser He-Ne expands on the rough object surface. The diffused light reflected from the object's surface is collected by the imaging lens and then enters Mach-Zehnder Interferometer, used as the shearing device. In the Mach-Zehnder Interferometer, the shearing amount and carrier frequency on the spatial frequency domain can be changed by tilting the angle of one mirror of the system. After tilting the mirror angle, the two-beam wavefront equation is expressed as:

$$U_{1m}(x,y) = |U_{1m}(x,y)|e^{i\varphi(x,y)} \tag{2.6}$$

$$U_{2m}(x,y) = |U_{2m}(x+\Delta x, y+\Delta y)|e^{i\varphi(x+\Delta x,y+\Delta y)-2\pi i f_m x} \quad (2.7)$$

In equation (2.6) and (2.7), $\mathbf{U_1}$ and $\mathbf{U_2}$ are the beams from the reference object and testing object, $\Delta\mathbf{x}$ and $\Delta\mathbf{y}$ represent the shearing distance in the x and y directions. In addition, the $\mathbf{f_m}$ is the carrier frequency introduced by the mirror tilting angle. The way to find $\mathbf{f_m}$ can be shown in equation (2.8).

$$f_m = \frac{\sin\beta}{\lambda} \quad (2.8)$$

So the total intensity recorded by the CCD camera are shown in the equation (2.9)

$$\begin{aligned} \mathrm{I_m} &= (\mathrm{U_{1m}} + \mathrm{U_{2m}}) * (\mathrm{U_{1m}}^* + \mathrm{U_{1m}}^*) \quad (2.9) \\ &= \mathrm{U_{1m}} * \mathrm{U_{1m}}^* + \mathrm{U_{2m}} * \mathrm{U_{2m}}^* + \mathrm{U_{1m}} * \mathrm{U_{2m}}^* + \mathrm{U_{2m}} * \mathrm{U_{1m}}^* \end{aligned}$$

In equation (2.9), the * is expressed as the complex conjugate. The Fourier Transform was applied to convert the image from the spatial domain to the Fourier domain. After Fourier Transform, the equation (2.10) can be changed as:

$$\begin{aligned} \mathrm{F}(I_m) &= U_{1m}(f_x, f_y) \otimes U_{1m}^*(f_x, f_y) + U_{2m}(f_x, f_y) *\otimes^* (f_x, f_y) \quad (2.10) \\ &+ U_1(f_x, f_y) \otimes U_2^*(f_x, f_y) + U_2(f_x, f_y) \otimes U_1^*(f_x, f_y) \end{aligned}$$

In the equation (2.10), × is the convolution operation, then let

$$U_1(f_x, f_y) = F(u1) \quad (2.11)$$

$$U_2(f_x, f_y) = F(u2) \quad (2.12)$$

After that, the Fourier spectrum can be found. For example, in the Dr. G Pedrini setup with a slit aperture, the spectrum's shape is rectangular, which can be changed by the shape of the aperture [81]. From Figure 2.3, the spectrum expressed the terms in the equation (2.12) in three parts because of the different spatial frequencies. The center spectrum is low frequency, term and contains the information from the background. On the other hand, the two side spectra contain the phase information of the recorded interferograms which are located at $(\boldsymbol{f_0}, \mathbf{0})$ and $(-\boldsymbol{f_0}, \mathbf{0})$. Along with these considerations, the Windowed Inverse Fourier Transform (WIFT) is applied to find phase distributions by the equation (2.13):

$$\varphi_m' + 2\pi x f_m = \arctan\frac{\mathrm{Im}[u_1 u_2^*]}{\mathrm{Re}[u_1 u_2^*]} \tag{2.13}$$

The relative phase difference is also expressed:

$$\Delta\varphi_m = \varphi - \varphi' \tag{2.14}$$

After that, based on the equation (2.14)

$$\Delta\varphi_m = \frac{2\pi\delta x}{\lambda} d \cdot s \tag{2.15}$$

Along with the condensations, the relative phase difference are found, and follow the in-plane displacement theory and enroll sensitivity vector s form the equation (2.16), the gradient can be expressed as:

$$\frac{\partial w}{\partial x} = \frac{\lambda}{2\pi(1 + cos(\alpha))\delta x} \Delta\varphi_m \tag{2.16}$$

$$\frac{\partial w}{\partial y} = \frac{\lambda}{2\pi(1 + cos(\alpha))\delta y} \Delta\varphi_m \tag{2.17}$$

So the x and y direction deformation gradient can be calculated. To summarize, in this way, the shearogram can be evaluated from a pair of speckle pattern images taken before and after loading. Thus, the acquisition rate is limited by the phase shift step length but only by the camera's capabilities.

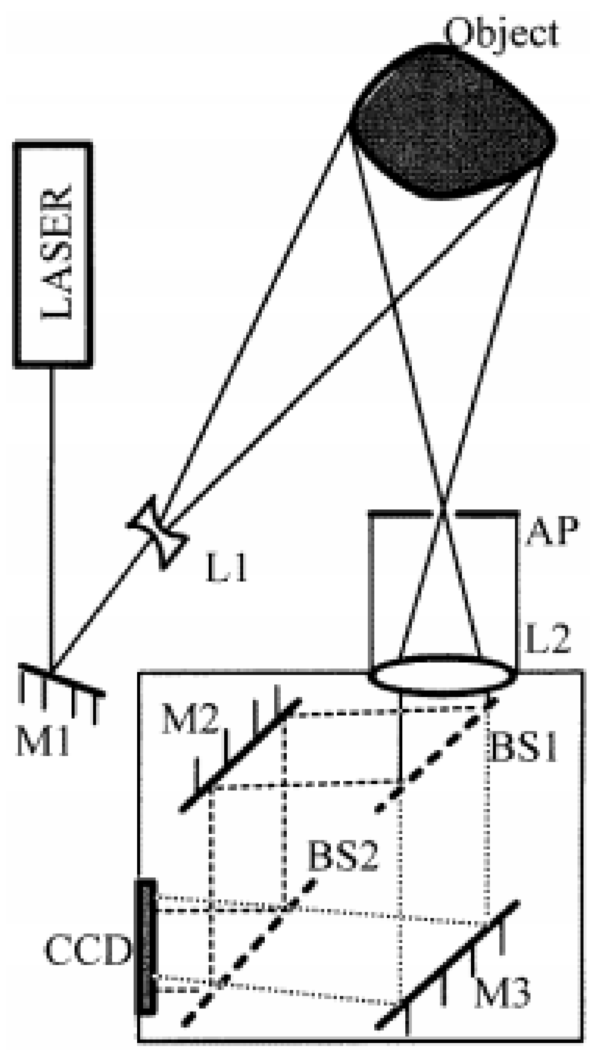

Figure 2.2 Experimental set-up of shearography with spatial carrier frequency using a Mach–Zehnder interferometer

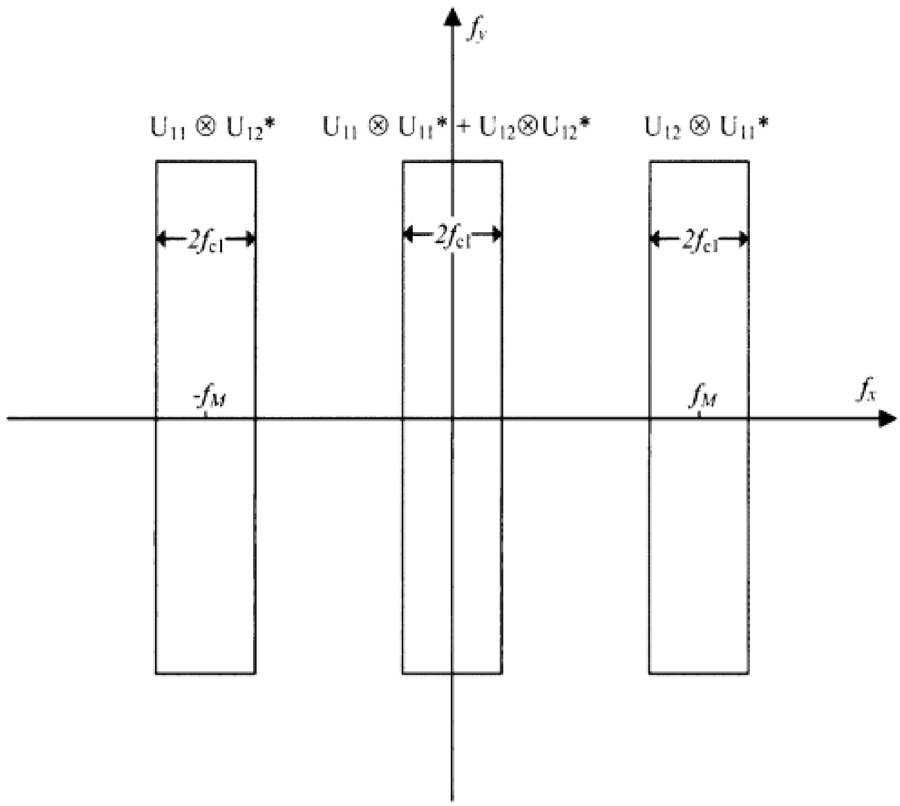

Figure 2.3. Spectrum of Recorded Speckle Pattern Image2.2. Results

2.4 Measuring Sensitivity

A significant amount of promise has been proven by digital shearography in terms of detecting material defects, particularly in composite materials. Researchers and engineers raise the question, "How small of a material defect can be detected by this technique?" (also known as "what is the smallest detectable defect by digital shearography") quite frequently. This is the question that is asked the most frequently. According to NDT, this is referred to as the measurement sensitivity. The notion of measuring sensitivity for non-destructive testing (NDT) using digital shearography one of the difficult development directions. It is related to the sensitivity of phase measurement, the shearing amount and shearing direction, the magnitude and the method of loading, the depth of defects, and the properties of material. All of the components that have an effect on the measurement sensitivity, and all parameters will be analyzed and discussed in this chapter, as well as the relationships that exist between these several aspects.

2.4.1 Sensitivity for phase measurement

Through the utilization of the phase shift approach, digital shearography is able to ascertain the relative phase change A, which in turn calculates the relative deformation dw. Along with these considerations, the sensitivity for measuring the relative deformation dw is primarily dependent on the sensitivity for detecting phase determination. In theory, the phase shift technique has the potential to achieve a sensitivity value of $2\pi/256$ for phase determination, provided that the hardware resolution employed is 8 bits. The phase determination sensitivity in speckle interferometry, on the other hand, is between $2\pi/30$ and $2\pi/10$ due to speckle noise [82]. This is considered to be rather practical. A measuring sensitivity of $2\pi/10$ should be possible, according to experimental investigation, despite the fact that the phase determination sensitivity is dependent on a variety of factors, including the PZT that is utilized, the hardware resolution, the various phase shift technique algorithms, the noise in the phase map, and the smoothing methods that are utilized [27].

The sensitivity for determination of the relative deformation 5w is thus given by:

$$\delta w = \frac{\lambda}{4\pi}\frac{2\pi}{10} = \frac{\lambda}{20} \tag{2.19}$$

2.4.2 Shearing amount

Relative deformation means the deformation difference between two points separated by a shearing amount. Obviously, the relative deformation depends greatly on the shearing amount.

The relative deformation dw is likewise minimal when a small shearing amount is employed, and the measuring sensitivity to the relative deformation is low so that the shearing amount can be measured accurately. Nevertheless, the outcome of the measurement is rather near to the first derivative of deformation, often known as strain information. It is possible to readily identify a defect using digital shearography with a tiny shearing amount if the defect causes a strain concentration when it is subjected to a tiny force. On the other hand, a great number of small defects do not result in the formation of a strain concentration when subjected to a small load, and in most cases, a large load cannot be utilized in applications that are situated in the real world. In these circumstances, it is recommended that a shearing amount that is relatively big be chosen in order to achieve a high level of measurement sensitivity to the relative deformation.

A measurement that has a significant shearing amount being applied to it is sensitive to relative deformation not just at the location of the defect, but also at the area of the material that is surrounding it. Along with this considerations, the measurement results contain information about the global deformation and the defect, which makes it difficult to determine the extent of the defect and determine its location. The measurement findings of the composite panel while it was subjected to thermal load are displayed in Figure 2.14. There is one huge disbond and two very modest disbonds contained within the panel. An investigation was conducted on the panel using a modest shearing amount (0.5 mm) and a large shearing amount (5 mm), respectively. In both of the investigations, the thermal loads were nearly identical to one another. Only the large disbond and the middle size disbond were discovered when the little shearing amount was used; nonetheless, the location and size of the defects were displayed in a clear manner. For the selection of the large magnitude of shearing amount, the large disbond as well as two lesser disbonds were seen. The magnitude of the disbonds, on the other hand, was not very evident due to the fact that the information from the defect and the material that was surrounding it was scattered.

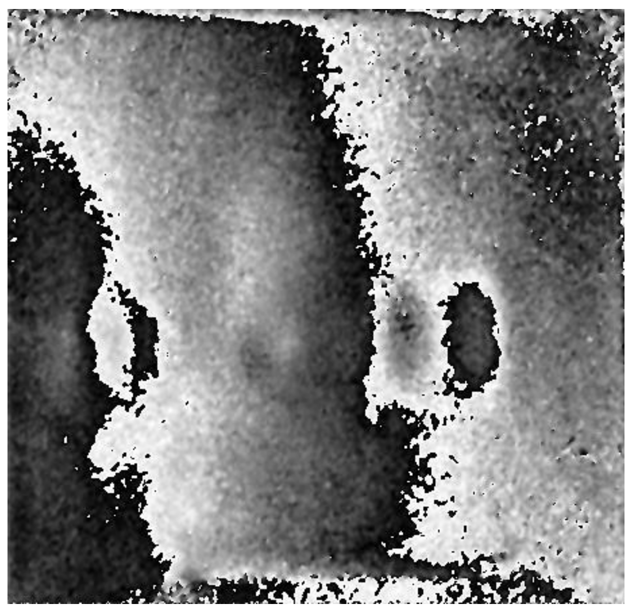

(a) Using a big shearing amount (5 mm)

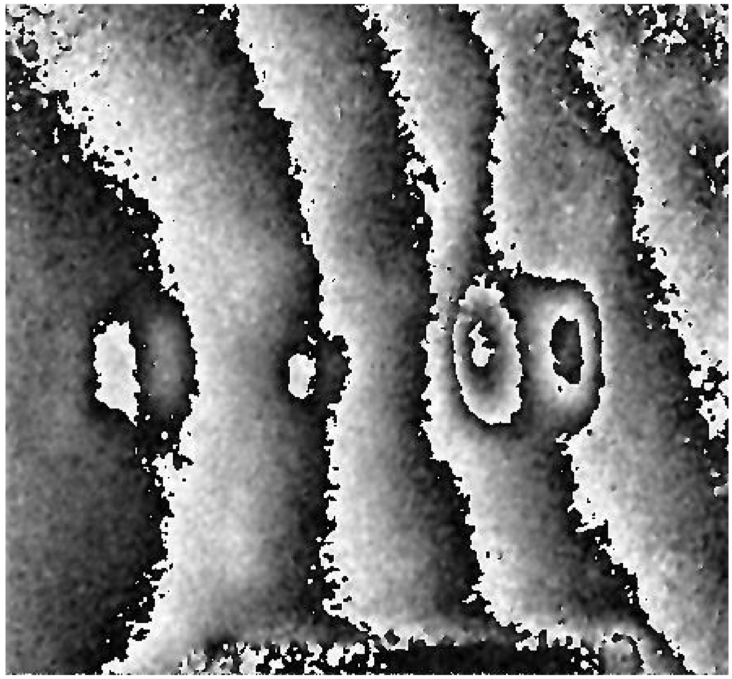

(b) Using a small shearing amount (0.5 mm)

Figure 2.4 Digital shearograms of a composite panel under thermal load: (a) using a small shearing amount (5 mm), (b) using a big shearing amount (0.5 mm)

On the one hand, it is obvious that one ought to choose a tiny shearing amount in order to acquire strain information; on the other hand, one ought to make use of a large shearing amount in order to acquire a high measurement sensitivity. The subject of what the appropriate magnitude of shearing amount is one that is routinely raised by researchers and engineers from time to time. In the subsequent portion of this section, the idea of a crucial magnitude of shearing amount will be presented to the reader. The shearing amount at which the measuring setup offers the highest possible level of sensitivity is referred to as the crucial shearing amount. When the shearing amount exceeds the critical amount, the sensitivity for measuring relative deformation will no longer grow because the essential amount is the critical amount. In order to provide an explanation for this idea, Figure 2.5 illustrates a link between the shearing amount, the relative shearing amount, and the magnitude of deformation that occurs over a defect area. As the shearing amount increase, it is obvious that the relative deformation will also increase. After the shearing amount has reached half of the area of deformation, also known as the half of the defect diameter, the relative deformation, on the other hand, does not continue to increase. During this magnitude of shearing amount, the maximal relative deformation, denoted by dw_{max}, is equivalent to the maximal deformation, denoted by w_{max}. Within the context of this dissertation, the shearing amount in question is referred to as the key shearing amount. For the vast majority of industrial applications, the absolute minimum defect diameter that must be detected is already established.

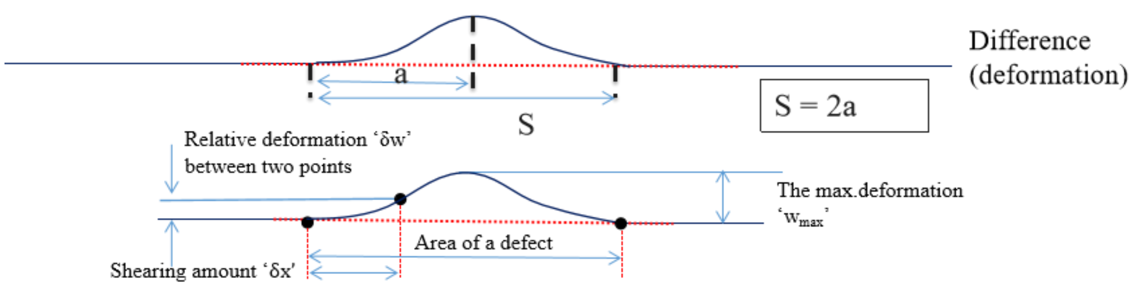

Figure 2.5 Relationship among the deformation, the relative deformation, and the shearing amount at a defect area

Magnitude of shearing amount is best determined by selecting the half diameter of the minimal defect as the optimal selection. This value makes it possible to locate problems that are more significant than the minimal defect with relative ease. The magnitude of shearing amount that is being used has the highest level of sensitivity for the minimum defect, and engineers and researchers who are engaged in shearographic inspection will find this value to be of great use.

2.4.3 Shearing direction

Among the characteristics that affect the application of shearography, the shearing direction significantly influences the sensitivity of shearography. The first derivative of deformation in different shearing directions are shown in the following equations:

$$\Delta_y = \frac{2\pi}{\lambda}\left(1+\cos(\alpha)\right)\frac{\partial w}{\partial y} = \frac{4\pi\delta y}{\lambda} * \frac{\partial w}{\partial y} \tag{2.20}$$

$$\Delta_x = \frac{2\pi}{\lambda}\left(1+\cos(\alpha)\right)\frac{\partial w}{\partial x} = \frac{4\pi\delta x}{\lambda} * \frac{\partial w}{\partial x} \tag{2.21}$$

If a defect has a circular shape, the shearing direction plays no role for defect detection because an anomaly of the relative deformation presents a uniform appearance in all directions. However, if a defect has a narrowly rectangular form, the shearing direction plays an important role for defect detection because an anomaly of the relative deformation is obviously different in all directions. Figure 2.6 a show a quadratic plate with one round groove and three narrow rectangular grooves oriented in different directions on the backside. For example, it is difficult to find a defect through x-directional shearing if the defect of the test object has a large cross-section in the x-direction, but a tiny cross-section in the y-direction. From Figure 2.6 b, the bottom defects are undetectable when a certain shearing amount is given in the x-direction; however, as shown in Figure 2.6 c, the bottom defects are detected when shearing is in the y-direction. Based off these results, a single shearing direction test is not sufficient. Testing two orthogonal shearing directions for the same object is necessary.

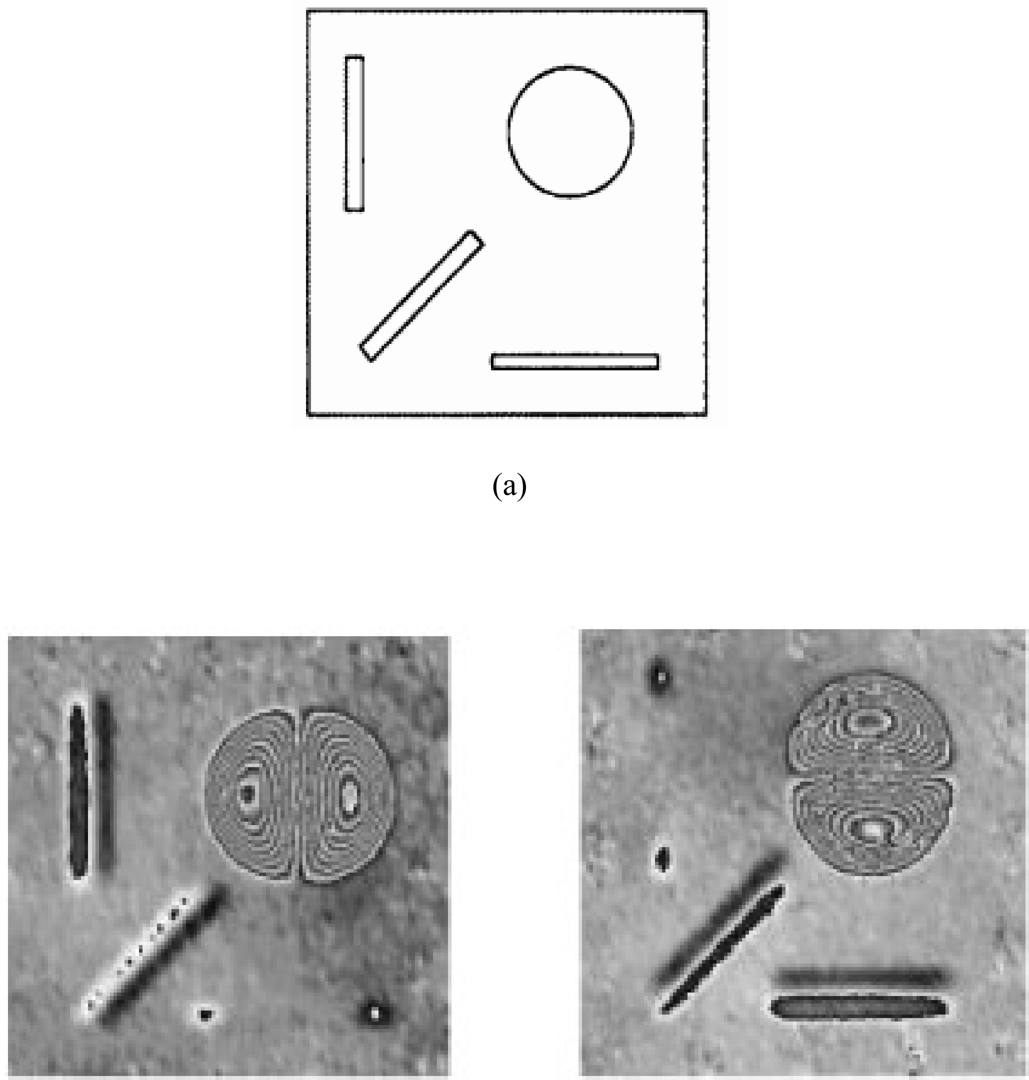

(a)

(b) (c)

Figure 2.6 Digital shearograms with different shearing direction: (a) The shape and the location of the four grooves, (b) digital shearogram with a horizontal shearing direction; the horizontal groove appears blurred; (c) digital shearogram with a vertical shearing direction; the vertical notch appears blurred as well.

2.5 Filtering method of interference phase diagram

Due to the fact that speckle is a form of noise, shearography is a technique that makes advantage of the random distribution features of speckles in order to encode the surface information of the object that is being measured and to acquire the surface information of the object that is being measured through calculation. At the same time as the shearography system is being utilized to identify the item that is being measured, a number of systematic and random mistakes are also being introduced. In most cases, it is required to filter the phase diagram that is produced as a result of the measurement in order to make the results of the measurement more understandable and to make future processing easier [83]. Techniques such as mean filtering [84], median filtering [85], phase filtering, and frequency domain low-pass filtering [86] are examples of filtering methods that are implemented often. Figure 2.7 depicts the findings of an observation made using shearography for a composite material that contains three defects. Figure 2.7(a) depicts the result that has not been filtered, while Figure 2.7(b) depicts the result that has been filtered. After filtering, the defect information is expressed more clearly, and lesser problems are easier to see, according to comparison. This is something that can be identified after filtering. The importance of filtering is demonstrated by the Figure 2.7.

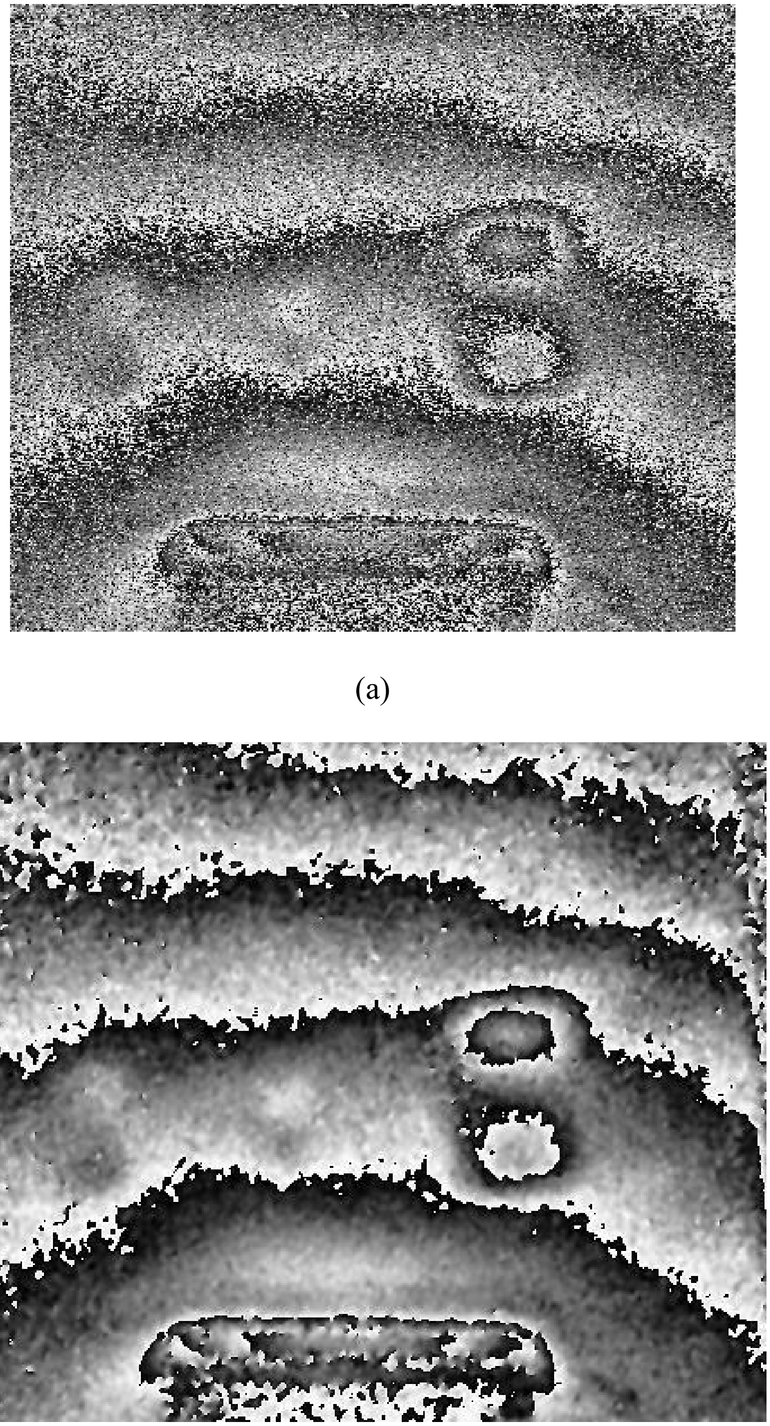

(a)

(b)

Figure 2.7 Flitter result comparison (a) unfiltered data (b) filtered data

One of the most used linear filtering methods is called mean filtering. For the purpose of replacing the initial value of the modified point, mean filtering method makes use of the average value of the points that are located around the central pixel. This technique is effective for dealing with high-frequency noise, in addition to having the benefits of straightforward computation and a rapid speed. inhibiting effect. Having said that, this technique will also result in the image being blurry, and the filtering process will result in a significant percentage of the image's information being destroyed. The size of the template that is being used is directly related to the amount of detail that is being lost. As the size of the template increases, some of the details are lost. When it comes to the phase image of speckle interference, the position of the fringe jump has a direct impact on the accuracy of subsequent processing. Filtering the impact of speckle is done in order to gain better fringe details. Therefore, the ideal phase map of the speckle interference cannot be achieved by utilizing mean filtering instead of any other method.

The technology of median filtering is a nonlinear signal processing technique that is founded on the philosophy of sorting statistical data. The gray value of each pixel is determined by this method by taking into account the median value of the gray value of all the pixels that are contained within a neighborhood window consisting of that point. Also, this technique has the ability to get rid of isolated noise locations. The median filtering technique does not involve statistical analysis of the image throughout the filtering process, and it does not cause the image to become blurry. Nevertheless, this technique is mostly utilized for the purpose of eliminating salt and pepper noise because it has a poor filtering ability for Gaussian noise. Due to the fact that this technique is a nonlinear technology, it has a limited capacity to maintain the linear phase information that is present in the phase diagram representation of speckle interference. Because of the poor calculation speed of this method, the results of the filtering process are not as smooth as those obtained using other methods.

There is another type of linear filtering that is known as Gaussian filtering. When compared to median filtering, which has a limited capacity to filter out Gaussian noise, Gaussian filtering has a more effective capacity to filter out Gaussian noise. The Gaussian filter is a technique that is similar to the mean filter in that it is also a weighted averaging of the entire image. The value of the target pixel is determined by the result of the weighted average of the values of the other pixels in the area surrounding the target pixel in the image. On the other hand, Gaussian smoothing possesses anisotropy as one of its features. Following the use of the filter, the image's distinctive characteristics will be extinguished.

When applied to the digital shearography, frequency-domain low-pass filtering is responsible for performing the Fourier transform. The low-frequency components of the spectrum can be retrieved from the spectrum through the control of the transfer function of the filter. Remove a portion of the high-frequency noise from the image while preserving the global information contained within it. Low-pass filtering in the frequency domain can be further broken into three categories, namely the ideal low-pass filter, the exponential low-pass filter, and the Butterworth low-pass filter. These classifications are determined by the transfer function of the filter. Regarding low-pass filters that operate in the frequency domain, the filtering capability is directly proportional to the cutoff frequency; however, the details that correlate to this frequency are severely lost.

The phase filtering technology is a technique that preprocesses the image in order to guarantee the jump information of the speckle interference pattern. This is done in order to overcome the problem of phase image peak information loss that is caused by other filtering technologies. Because the information at the transition point of the speckle interferogram is discontinuous, the technology of phase filtering has to turn the discontinuous information into continuous information so that it can be processed. Through the application of Euler's equation, this technique is able to expand the phase information of the phase diagram on the unit circle of the complex plane. As a result, discontinuous transitions are transformed into continuous information. Following this, filter the information of the real part and the imaginary part of the complex plane, respectively, using techniques such as mean filtering, median filtering, and other similar techniques, in order to produce new complex number information. The filtered phase map can be obtained by recovering the newly filtered information with the filtering process. Both the jump information of the speckle interference phase diagram and the noise information of the phase image may be efficiently filtered away by this method, which will not have any impact on the jump information.

During the actual process of filtering, phase technology is frequently utilized to save the jump information of the speckle interference pattern. Subsequently, several filtering techniques are utilized in order to filter the speckle interference phase pattern in accordance with the requirements.

2.6 Research on speckle interferogram phase unwrapping technology

The filtering result of the digital shearography is a wrapped map that contains the phase information of the surface of the measured object that is wrapped inside the range. The diagram of the digital shearography shows that the phase distribution in the Figure is a sawtooth discontinuous distribution. This can be seen by considering the diagram. Every time the phase rises, the phase information of the next pixel drops to zero and then rises again, this time from zero to twice the phase. In order to access the information on the surface deformation of the object that is being measured, it is necessary to first unwrap the phase information that has been wrapped around the object. This will allow you to obtain the real distribution of the first derivative of the surface deformation of the object that is being measured [87, 88]. At the moment, unwrapping technology is not only utilized for the purpose of resynthesizing continuous information of phase maps, but it is also widely utilized in synthetic aperture radar and grating cloud pattern assessment, in addition to other applications.

Phase diagram wrapping technology's fundamental idea can be summed up as follows: beginning at a specific phase starting point, compare the phase values of nearby pixels. The phase change is continuous within the same range $[0,2\pi]$. A jump in the phase value is said to occur here when the phase difference between neighboring pixels is greater than a threshold. An integer multiple of the phase value of the preceding pixel can be added or subtracted, depending on the transition scenario, to determine the phase information of the subsequent pixel. This is how phase information that is discontinuous is transformed into continuous phase information. The surface deformation of the observed item can be derived by integrating or processing this continuous phase information in another way [89].

Local unwrapping algorithms and global fitting unwrapping algorithms are the two categories that can be used to classify how unwrapping algorithms are currently classified. Path algorithm and region expansion algorithm are two subcategories that can be further split under the local unwrapping algorithm. Path-based unwrapping is the algorithm that is utilized the most frequently among these algorithms. Based on a path that has already been created, this method assesses the phase values of neighboring pixels along the path. It is possible to consider that the phase value of the pixel has changed over time if the difference in phase values between the two pixels is greater than a particular threshold. As far as the jump is concerned; by adding or subtracting an integer multiple of the following pixel, it is possible to determine the phase value of the subsequent pixel in this scenario. To solve the original wrapped phase image, this technique has the advantage of being quick, but it also has higher quality requirements. It is possible to break the path algorithm into the following categories, based on the many preset paths: the center-radiation path algorithm, the queue spiral path algorithm, the split line path algorithm, etc.. Pull lines will appear, however, if the original wrapped phase image that needs to be solved still contains a significant amount of noise. This is because the noise's impact will be conveyed along the solution path while the solution is being performed. It is possible to prevent the effects of noise from propagating along the solution path by employing the region expansion technique in this condition. In order to acquire the unwrapped diagrams, the primary idea of this algorithm is to first unwrap various parts in a distinct manner, then to re-wrap the areas that have been unwrapped and finally add them back into the original image. Reliability-guided region expansion algorithm is a method that is frequently utilized. Calculating fringe contrast, the phase second-order partial derivative approach, and other methods are some examples of the subcategories that can be applied to the process of getting the dependability of image pixels. The global fitting algorithm is an algorithm that does not depend on any particular path. The global fitting technique that is based on the least squares method is not going to be impacted by the noise in the image, and it has a greater calculation accuracy than the other algorithms. Phase prediction processing is recommended to minimize the error by adjusting existing noise points or significant error areas. There are a greater number of applications for it when the image quality is not good. This algorithm's primary objective is to minimize the total phase value of each pixel before and after unwrapping, as well as the true phase value of the pixel, and the gradient change for each pixel. The objective function of least squares is designed in such a way that the difference between the phase value of each pixel before and after unwrapping and its actual value is as close to zero as possible.

2.7 Summary of this chapter

This chapter provides a concise introduction to the generating principle and characteristics of speckle, as well as a concise introduction to the statistical characteristics of the phenomenon. Additionally, the parameters that influence the sensitivity of shearography are examined in this article. Following that, the fundamental idea behind digital shearography as well as the connection between phase value and deformation were presented. After that, a number of phase extraction technologies that are frequently utilized are thoroughly discussed, with a particular emphasis on temporal phase shift and spatial carrier phase shift technologies. Additionally, the fundamentals of these technologies, as well as their benefits and drawbacks, are studied. The final step is to present the phase image processing methods that are often employed. The primary focus is on presenting the many types of phase diagram filtering methods and phase image wrapping algorithms, as well as the advantages and limitations associated are discussed.

CHAPTER THREE

BASIC THEORY OF ELASTIC THIN PLATE

3.1 Plate Theory

Because defects on the object test by the digital shearography always close to the surface, and the distance between the surface to defect can be consider as a thin plate. Although, there are some defects in deeper inside the specimen, the thin plate theory will be more adaptable to determine the sensitivity of digital shearography An element of structural design that is flat and has a thickness that is relatively tiny in comparison to the surface dimensions is called a plate. Fig. 3.1 shows that the thickness is measured in a direction that is normal to the central surface of the plate. The thickness is typically constant, although it can be varied [90].

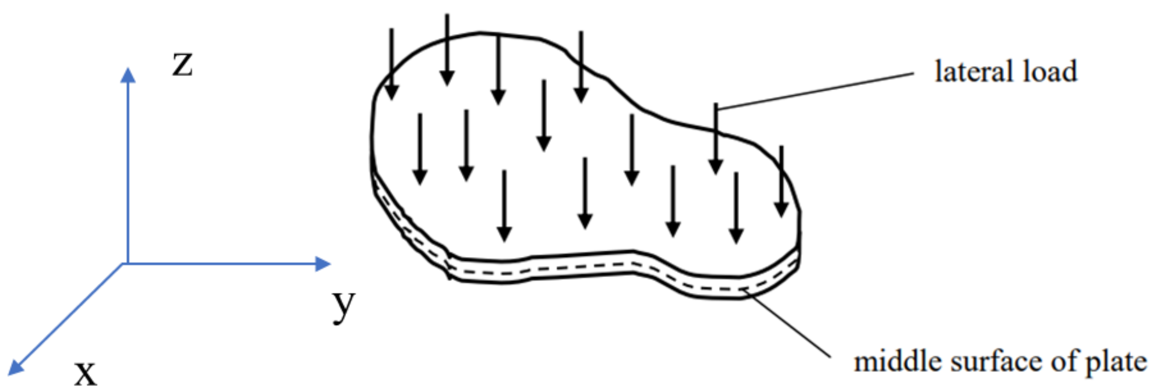

Figure 3.1 A plate

The theory of two-dimensional plane stress can be used to solve problems with plates that are solely subjected to in-plane loading. On the other hand, plate theory is primarily concerned with lateral loading instead of axial force. In the plate theory, the stress components are allowed to change along the thickness of the plate, which allows for the possibility of bending moments (Fig. 3.2). This is one of the contrasts between the plane stress theory and the plate theory.

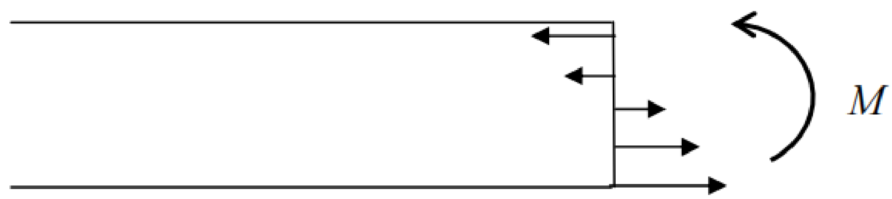

Figure. 3.2: Stress distribution through the thickness of a plate and resultant bending moment

Therefore, let's begin with the theory of plates and beams. Plate theory is an approximation theory, which means that assumptions are made and the general equations of elasticity in three dimensions are lowered because of such assumptions. One could say that it is quite similar to the beam theory, but with an additional dimension. This theory proves to be accurate because the plate is relatively thin (as described in beam theory) and the deflection is minimal compared to the thickness of the plate. When it comes to plates, things are more complicated than when it comes to beams. As seen in Figure 6.4, the plate not only bends, but it also has the potential to undergo torsion, which means that it can twist.

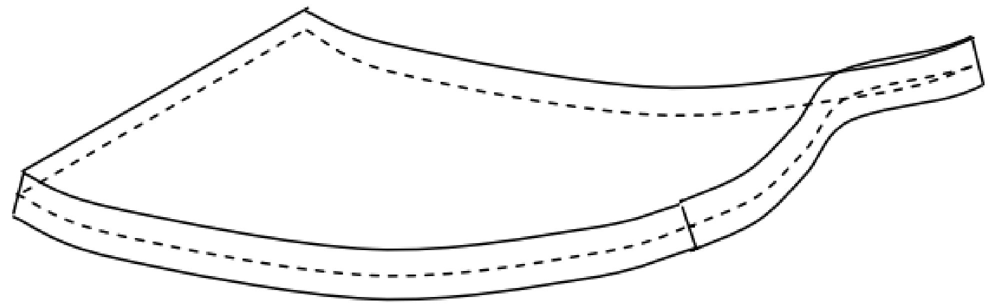

Figure. 3.3: Torsion of a plate

A discussion of the assumptions that underpin plate theory will be presented in the following sections. In order to create a right-handed set, the mid-surface of the plate should be positioned in the x-y plane, and the z-axis should pass in the direction of the thickness. Figure 3.4 illustrates the stress components that are manifesting themselves on a typical piece of the plate.

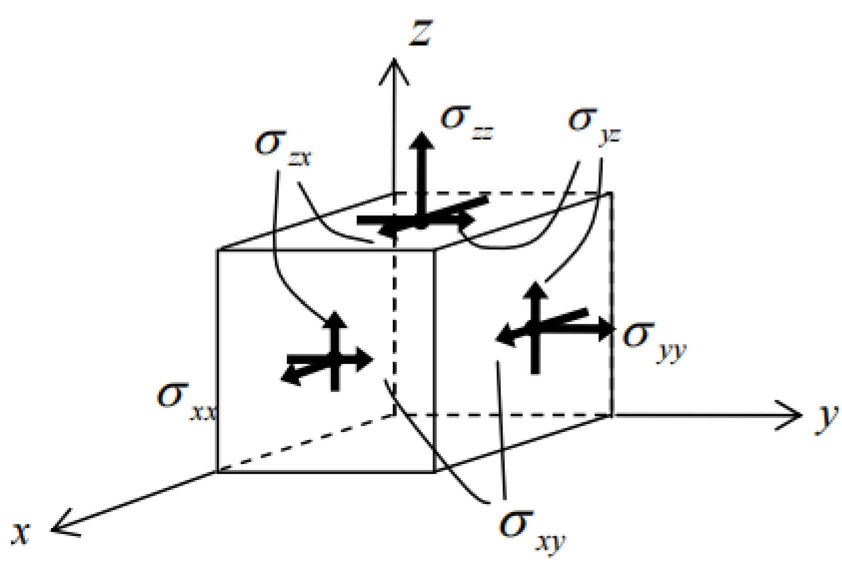

Figure. 3.4: Stresses acting on a material element

Along with this consideration, three assumptions were presented for the purpose of analyzing the elastic plate deformation theory. These three presumptions serve as the foundation for either the Kirchhoff Plate Theory or the Classical Plate Theory. The mid-plane is considered to be a "neutral plane" as the foundational assumption. The third assumption is that vertical strain is not taken into account, and the second assumption is that line elements will continue to be normal to the mid-plane.

This is the initial assumption, which states that the center plane of the plate does not experience any in-plane stress or strain. It is decided to in the event that the plate is bent, the material that is located above and below this mid-plane will undergo in-plane deformation. When it comes to plate theory, the mid-plane serves the same purpose as the neutral axis does when it comes to beam theory.

In the second assumption, the assumption set line elements that are lying perpendicular to the middle surface of the plate remain perpendicular to the middle surface during deformation, as shown in Figure 3.5; this is comparable to the assumption that "plane sections remain plane" in the beam theory.

As a final assumption, during the process of deformation, line components that are perpendicular to the mid-surface do not experience any change in length. This ensures that ε_{zz} is equal to zero over the entire plate. To reiterate, this is comparable to an assumption that is made by the beam theory.

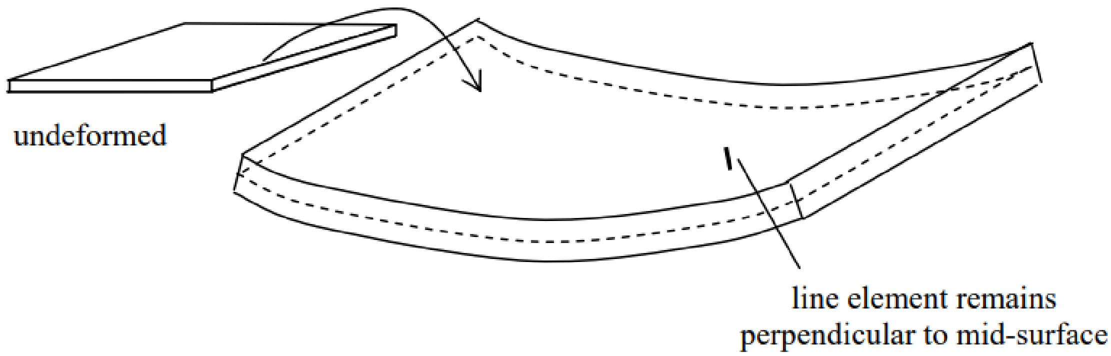

Figure. 3.5: Deformed line elements remain perpendicular to the mid-plane

The Notation and Stress Resultants will be covered in the subsequent sections of this article. Once the stresses have been integrated across the thickness of the plate, the stress resultants can be determined. On this part, three different types of force will be discussed: the moment, the out of plane force, and the in-plane force. It is necessary to talk about two bending moments and one twisting moment, and two shearing forces which are out of plane. The tension on the surface was caused by three different types of in-plane forces: two conventional in-plane forces and one shearing in-plane force.

Then, the in-plane normal forces and bending moments is discussed, which are listed in Figure 3.6. The force equation are conclude in equation (3.1) to (3.4)

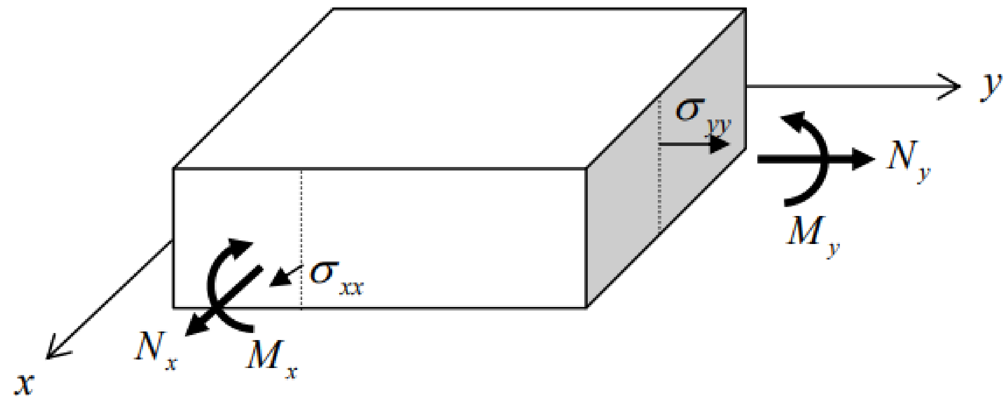

Figure 3.6 In-plane normal forces and bending moments

$$N_x = \int_{-\frac{h}{2}}^{\frac{h}{2}} \sigma_{xx} dz \tag{3.1}$$

$$N_y = \int_{-\frac{h}{2}}^{\frac{h}{2}} \sigma_{yy} dz \tag{3.2}$$

$$M_x = -\int_{-\frac{h}{2}}^{\frac{h}{2}} z\sigma_{xx} dz \tag{3.3}$$

$$M_y = -\int_{-\frac{h}{2}}^{\frac{h}{2}} z\sigma_{yy} dz \tag{3.4}$$

The in-plane shear force and twisting moments are shown in Figure 3.7 and equation (3.5) to (3.6).

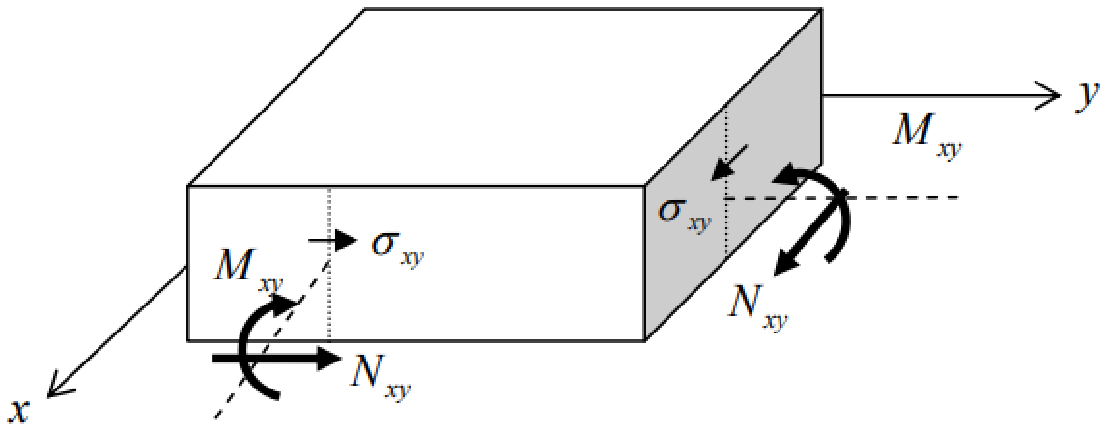

Figure 3.7 In-plane shear force and twisting moments

$$N_{xy} = \int_{-\frac{h}{2}}^{\frac{h}{2}} \sigma_{xy} dz \tag{3.5}$$

$$M_{xy} = \int_{-\frac{h}{2}}^{\frac{h}{2}} z\sigma_{xy} dz \tag{3.6}$$

The Out-of-plane shear force and twisting moments are shown in Figure 3.8 and equation (3.7) to (3.8).

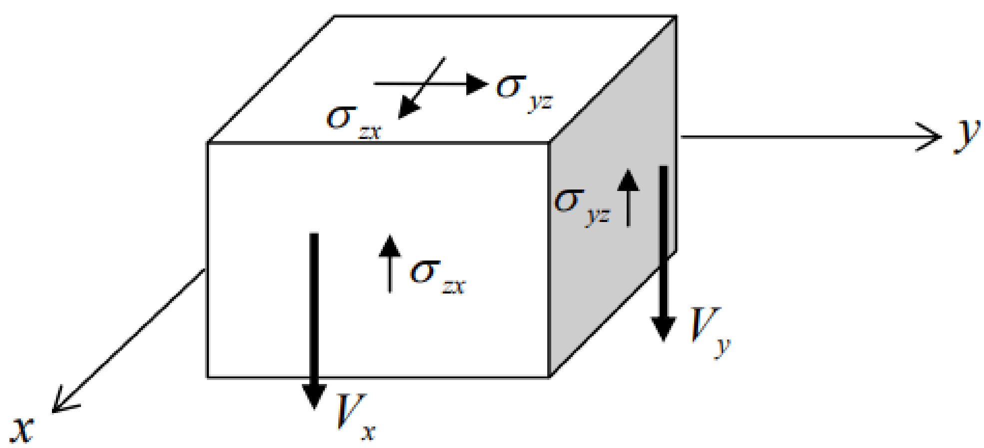

Figure 3.8 Out-of-plane shear force

$$V_x = -\int_{-\frac{h}{2}}^{\frac{h}{2}} \sigma_{zx} dz \tag{3.7}$$

$$V_y = -\int_{-\frac{h}{2}}^{\frac{h}{2}} \sigma_{yz} dz \tag{3.8}$$

Note that the above "forces" and "moments" are actually forces and moments per unit length. This allows one to have moments varying across any section – unlike in the beam theory, where the moments are for the complete beam cross-section. If one considers an element with dimensions $\triangle$x and $\triangle$y , the actual moments acting on the element are $M_x \triangle y$, $M_y \triangle x$, $M_{xy} \triangle x$ and, $M_{xy} \triangle y$. and the forces acting on the element are $V_x \triangle y$, $V_y \triangle x$, $N_x \triangle y$, $N_y \triangle x$, $N_{xy} \triangle x$ and $N_{xy} \triangle y$. The in-plane forces, which are comparable to the axial forces proposed by the beam theory, do not play a significant part in the majority of the subsequent discussion. Additionally, it is essential to take them into consideration in order to develop more precise theories of plate bending because they are helpful in the analysis of buckling of plates.

3.2 The Moment-Curvature Equations

3.2.1 From Beam Theory to Plate Theory

According to the beam theory, the strain varies linearly over the thickness. This is because the beam theory is based on the assumption that plane parts will remain planar and that one may ignore the transverse strain. Assuming that y is positive and pointing upward, the equation for the beam is ε_{xx}=-y / R, where R is the radius of curvature and R is positive when the beam bends "up." The equation $\varepsilon_{xx} = -y \frac{\partial v^2}{\partial x^2}$ can be expressed in terms of the curvature, which is $\frac{\partial v^2}{\partial x^2} = \frac{1}{R}$, where v measures the deflection. The beam theory assumptions are largely the same for the plate, which results in strains that are proportional to the distance from the neutral (mid-plane) surface, z,. Consequently, this results in stresses xx and yy that fluctuate in a linear fashion (zz is also assumed to be zero, just like in the beam theory).

<u>3.2.2 Strains in a Plate</u>

After that, the strains that are found in a plate are investigated. In the beginning, a full strain-state will be investigated, and after that, this will be simplified down to a number of approximate answers. Take for example a line element that is parallel to the x axis and has a length of △x. Allow the element to move in the manner depicted in Figure 3.9. When the curvature in the previous section is discussed, the symbol w is introduced to represent the displacement of the mid-surface. However, the symbol w (x, y, z) are employed to represent the general vertical displacement of any particle in the plate. Assume that the equivalent displacements in the x and y directions are denoted by the letters u and v. Both the original length of the element and its distorted length are denoted by the symbol’s dS and ds, respectively. By applying Pythagoras' theorem, which is listed in equation 3.9, the unit change in length of the element, also known as the precise normal strain, may be determined.

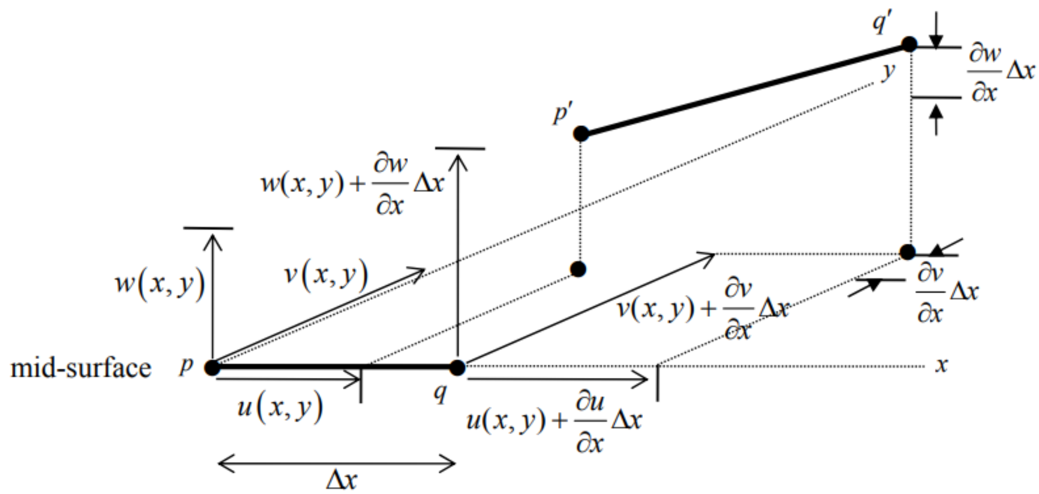

Figure 3.9 Deformation of a material fiber in the x direction

$$\varepsilon_{xx} = \frac{ds - dS}{dS} = \frac{|p'q'| - |pq|}{|pq|} = \sqrt{(1 + \frac{\partial u}{\partial x})^2 + (\frac{\partial v}{\partial x})^2 + (\frac{\partial w}{\partial x})^2} - 1 \tag{3.9}$$

The displacement gradients are small, $\varepsilon \ll 1$, so the squares and products of these terms may be neglected $\frac{\partial u}{\partial x}, \frac{\partial u}{\partial y}, \frac{\partial u}{\partial z}, \frac{\partial v}{\partial x}, \frac{\partial v}{\partial y}, \frac{\partial v}{\partial z}, \frac{\partial w}{\partial z}$ will be ignored. However, for the moment, the squares and products of the slopes will be retained, as they may be significant. For example, for the same order as the strains, under certain circumstances, only $(\frac{\partial w}{\partial x})^2$, $(\frac{\partial w}{\partial y})^2$, and $\frac{\partial w}{\partial y}\frac{\partial w}{\partial x}$ will be considered. Based on that, the equation (3.9) will be (3.10).

$$\varepsilon_{xx} = \sqrt{1 + 2\frac{\partial u}{\partial x} + (\frac{\partial w}{\partial x})^2} - 1 \tag{3.10}$$

Then, by enroll the math theory, which $\sqrt{1+x} \approx 1 + \frac{x}{2}$ when x<<1, the squares and products of these terms may be neglected . Based on that, the normal strain can be found in equation (3.11) to (3.13).

$$\varepsilon_{xx} = \frac{\partial u}{\partial x} + \frac{1}{2}(\frac{\partial w}{\partial x})^2 \tag{3.11}$$

$$\varepsilon_{yy} = \frac{\partial v}{\partial y} + \frac{1}{2}(\frac{\partial w}{\partial y})^2 \tag{3.12}$$

$$\varepsilon_{zz} = \frac{\partial w}{\partial z} \tag{3.13}$$

After that, consider next the angle change for line elements initially lying parallel to the axes, which displayed in Figure 3.10. In the Figure 3.10, θ change will be show the shearing strain which is angel rpq to r'p'q' in z direction. The change after deformation, the change in the initial right angle called γ. Because analysis in elastic stage, the $\gamma = \frac{\pi}{2} - \theta$. Because the math theory small $\gamma = sin\gamma = cos\theta$.

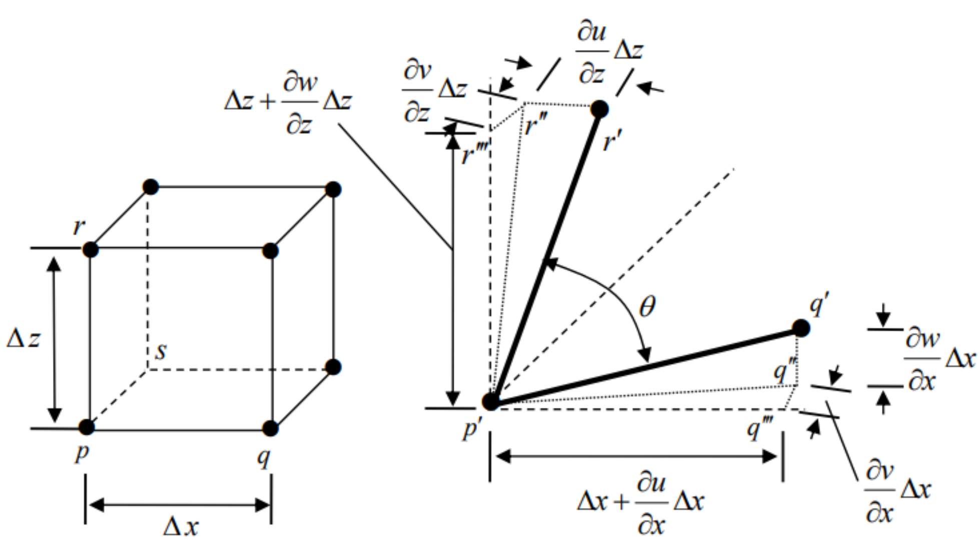

Figure 3.10: The deformation of Fig. 3.9, showing shear strains

Then take the dot product $\overrightarrow{p'q'}$ & $\overrightarrow{p'r'}$, which show in equation (3.14).

$$cos\theta = \frac{|p'q'''||r''r'| + |q'''q''||r'''r'| + |q''q'||p'r'''|}{|p'q'||p'r'|} \tag{3.14}$$

$$= \frac{\left(\Delta x + \frac{\partial u}{\partial x}\Delta x\right)\left(\frac{\partial u}{\partial z}\Delta z\right) + \left(\frac{\partial v}{\partial x}\Delta x\right)\left(\frac{\partial v}{\partial z}\Delta z\right) + (\frac{\partial w}{\partial x}\Delta x)(\Delta z + \frac{\partial w}{\partial z}\Delta z)}{\Delta x\sqrt{(1+\frac{\partial u}{\partial x})^2 + (\frac{\partial v}{\partial x})^2 + (\frac{\partial w}{\partial x})^2}\Delta z\sqrt{(1+\frac{\partial w}{\partial z})^2 + (\frac{\partial u}{\partial z})^2 + (\frac{\partial v}{\partial z})^2}}$$

The displacement gradients are small, $\varepsilon \ll 1$, so the squares and products of these terms may be neglected, which are $\frac{\partial u}{\partial x}, \frac{\partial u}{\partial z}, \frac{\partial v}{\partial x}, \frac{\partial v}{\partial z}$, and $\frac{\partial w}{\partial z}$. Based on the $cos\theta$ can be expressed in equation (3.15).

$$cos\theta = \frac{\partial u}{\partial z} + \frac{\partial w}{\partial x} + \frac{\partial v}{\partial x}\frac{\partial v}{\partial z} \tag{3.15}$$

So, the shearing strain will be expressed in equation (3.16) to (3.18)

$$\varepsilon_{xy} = \frac{1}{2}(\frac{\partial u}{\partial y} + \frac{\partial w}{\partial x} + \frac{\partial v}{\partial x}\frac{\partial v}{\partial z}) \tag{3.16}$$

$$\varepsilon_{xz} = \frac{1}{2}(\frac{\partial u}{\partial z} + \frac{\partial w}{\partial x}) \tag{3.17}$$

$$\varepsilon_{yz} = \frac{1}{2}(\frac{\partial v}{\partial z} + \frac{\partial w}{\partial y}) \tag{3.18}$$

The Von Kármán Strains hypothesis as a new hypothesis will be proposed in the next part. This hypothesis is proposed in order to better understand the elastic deformation of the thin plate. To present the presumptions that underpin the conventional plate hypothesis, the assumption that line elements normal to the mid-plane remain inextensible implies that:

$$\varepsilon_{zz} = \frac{\partial w}{\partial z} = 0 \tag{3.19}$$

Along with these considerations, it can be deduced that w is equal to w(x,y), which means that all particles at a specific (x,y) coordinate experience the same vertical displacement over the thickness of the plate. The assumption that line elements perpendicular to the mid-plane remain normal to the mid-plane after deformation then implies that $\varepsilon_{xz} = \varepsilon_{yz} = 0$. Based on the strain equations will be expressed as equation (3.20) to (3.25)

$$\varepsilon_{xx} = \frac{\partial u}{\partial x} + \frac{1}{2}(\frac{\partial w}{\partial x})^2 \tag{3.20}$$

$$\varepsilon_{yy} = \frac{\partial v}{\partial y} + \frac{1}{2}(\frac{\partial w}{\partial y})^2 \tag{3.21}$$

$$\varepsilon_{zz} = 0 \tag{3.22}$$

$$\varepsilon_{xy} = \frac{1}{2}(\frac{\partial u}{\partial y} + \frac{\partial w}{\partial x} + \frac{\partial v}{\partial x}\frac{\partial v}{\partial z}) \tag{3.23}$$

$$\varepsilon_{xz} = 0 \tag{3.24}$$

$$\varepsilon_{yz} = 0 \tag{3.25}$$

Afterwards, the strain can be subdivided. Strain can be divided into membrane strains and bending strains. Because Von Kármán Strains hypothesis, $\varepsilon_{xz} = 0$ and w=w(x,y), from equation (3.17), the new relationship will be expressed in equation (3.26) and (3.27).

$$\frac{\partial u}{\partial z} = -\frac{\partial w}{\partial x} \tag{3.26}$$

$$u(x,y,z) = -z\frac{\partial w}{\partial x} + u_0(x,y) \tag{3.27}$$

The $u_0(x,y)$ is the displacement in the mid-plane. In terms of the mid-surface displacements u_0, v_0 ,w_0 , then, the new relationship is equation (3.28) to (3.30). After that, the strain equation can updated with mid-plane theory, which expressed in equation (3.31) to (3.33).

$$u = u_0 - z\frac{\partial w_0}{\partial x} \tag{3.28}$$

$$v = v_0 - z\frac{\partial w_0}{\partial y} \tag{3.29}$$

$$w = w_0 \tag{3.30}$$

$$\varepsilon_{xx} = \frac{\partial u_0}{\partial x} + \frac{1}{2}(\frac{\partial w_0}{\partial x})^2 - \mathrm{z}\frac{\partial^2 w_0}{\partial x^2} \tag{3.31}$$

$$\varepsilon_{yy} = \frac{\partial v_0}{\partial y} + \frac{1}{2}(\frac{\partial w_0}{\partial y})^2 - \mathrm{z}\frac{\partial^2 w_0}{\partial y^2} \tag{3.32}$$

$$\varepsilon_{xy} = \frac{1}{2}(\frac{\partial u_0}{\partial y} + \frac{\partial v_0}{\partial x}) + \frac{1}{2}(\frac{\partial w_0}{\partial x}\frac{\partial w_0}{\partial y}) - \mathrm{z}\frac{\partial^2 w_0}{\partial x \partial y} \tag{3.33}$$

Small strains, which are typical for the mid-surface, are the first terms to be discussed. In situations when the plate bending is rather significant (when the rotations are approximately 10 to 15 degrees), it is necessary to take into consideration the second terms, which involve squares of displacement gradients and are non-linear. It is the membrane strains that are referred to when these first two phrases are combined. Flexural strains, also known as bending strains, are the last terms, which take into account second derivatives and are associated with curvatures. Under conditions in which the bending is not very large (when the rotations are less than about 10 degrees), one has (removing the subscript "0" from w). Finally, when the mid-surface strains are neglected, according to the final assumption of the classical plate theory, one has the updated strain equation will be updated again, which is shown in equation (3.34) to (3.36). The schematic of the theory expressed in Figure 3.11.

$$\varepsilon_{xx} = -\mathrm{z}\frac{\partial^2 w_0}{\partial x^2} \tag{3.34}$$

$$\varepsilon_{yy} = -z\frac{\partial^2 w_0}{\partial y^2} \tag{3.35}$$

$$\varepsilon_{xy} = -z\frac{\partial^2 w_0}{\partial x \partial y} \tag{3.36}$$

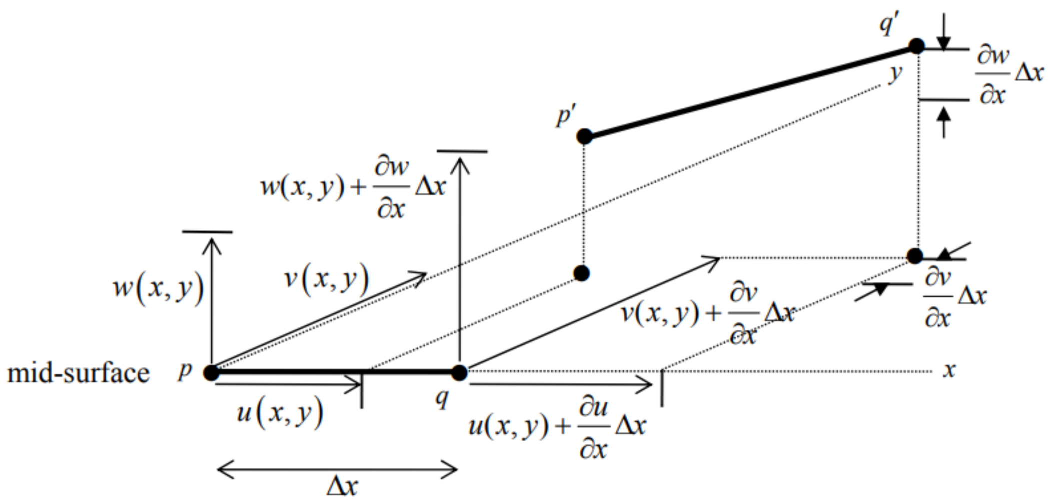

Figure 3.11 Schematic of membrane strains and bending strains

When the plate bends "up," the curvature is positive; points "above" the mid-surface experience negative normal strains, and points "below" the mid-surface experience positive normal strains; there is no shearing strain resulting from the plate's bending. In contrast, when the plate is subjected to a positive pure twist, the twisting moment is negative. This means that points "above" the mid-surface experience negative shear strain, while points "below" experience positive shear strain. Additionally, there is no normal strain resulting from this situation.

3.2.3 The Moment-Curvature equations

After then, Hooke's law was developed in order to transform the link between strain and deformation into the relationship between stress and deformation as well as the relationship between moment and deformation. A demonstration of Hooke's law can be found in equations (3.37 to 3.39). The equations (3.40) to (3.42) illustrate the link that exists between stress and strain with one another.

$$\varepsilon_{xx} = \frac{1}{E}(\sigma_{xx} - v(\sigma_{yy} + \sigma_{zz}) \tag{3.37}$$

$$\varepsilon_{yy} = \frac{1}{E}(\sigma_{yy} - v(\sigma_{xx} + \sigma_{zz}) \tag{3.38}$$

$$\varepsilon_{zz} = \frac{1}{E}(\sigma_{zz} - v(\sigma_{xx} + \sigma_{yy}) \tag{3.39}$$

$$\varepsilon_{xx} = \frac{1}{E}\sigma_{xx} - \frac{v}{E}\sigma_{yy} \tag{3.40}$$

$$\varepsilon_{yy} = \frac{1}{E}\sigma_{yy} - \frac{v}{E}\sigma_{xx} \tag{3.41}$$

$$\varepsilon_{xy} = \frac{1+v}{E}\sigma_{xy} \tag{3.42}$$

3.2.4 Principal Moments

Then the normal stress will be converted with Young's modulus and Passion ratio. The updated equation expressed in (3.43) to (3.45). Based on relationship between stress and elastic deformation, the moment relationship with elastic deformation will be conducted as follows (3.46) to (3.48), which called moment-curvature equations for a plate. The moment-curvature equations are analogous to the beam moment-deflection equation $\frac{\partial^2 v}{\partial x^2} = \frac{M}{EI}$. Afterwards, a new factor as D is provided, which is called plate stiffness or flexural rigidity and expressed in equation (3.49). The D plays the same role in the plate theory as does the flexural rigidity term EI in the beam theory.

$$\sigma_{xx} = -\frac{E}{1-v^2}z(\frac{\partial^2 w}{\partial x^2} + v\frac{\partial^2 w}{\partial y^2}) \tag{3.43}$$

$$\sigma_{yy} = -\frac{E}{1-v^2}z(\frac{\partial^2 w}{\partial y^2} + v\frac{\partial^2 w}{\partial x^2}) \tag{3.44}$$

$$\sigma_{yx} = -\frac{E}{1+v}z\frac{\partial^2 w}{\partial x \partial y} \tag{3.45}$$

$$M_x = D(\frac{\partial^2 w}{\partial x^2} + v\frac{\partial^2 w}{\partial y^2}) \tag{3.46}$$

$$M_y = D(\frac{\partial^2 w}{\partial y^2} + v\frac{\partial^2 w}{\partial x^2}) \tag{3.47}$$

$$M_{xy} = -\mathrm{D}(1-\mathrm{v})\frac{\partial^2 w}{\partial x \partial y} \tag{3.48}$$

$$D = \frac{Eh^3}{12(1-v^2)} \tag{3.49}$$

3.3 Equilibrium and Lateral Loading

In this section, lateral loads are considered and these lead to shearing forces V_x , V_y , in the plate.

In general, a plate will at any location be subjected to a lateral *pressure q,* bending moments M_x, M_y, M_{xy} and out-of-plane shear forces V_x and V_y ; *q* is the normal pressure on the upper surface of the plate, which is expressed as in equation (3.50). These quantities are related to each other through force equilibrium.

$$\sigma_{zz}(x,y) = \begin{cases} 0 & z = -\frac{h}{2} \\ -q(x,y) & z = \frac{h}{2} \end{cases} \tag{3.50}$$

The equilibrium theory of force and moment is then utilized to determine the relationship between force and deformation. This information serves as a theoretical foundation for the further analysis that will take place. Take into consideration a differential plate element with one corner located at (x, y) = (0,0), as shown in Figure 3.12. This element is subject to shear force, pressure, and moments. Taking into account the principle of force equilibrium in the vertical direction (but disregarding the possibility of a slight change in “q”, as this will merely result in the introduction of higher order terms), the equation can be stated as follows: Figure 3.12 is the schematic which is the representation of the equilibrium theory of forces and moments showing a schematic representation. In the beginning, the balance theory of forces will be discussed.

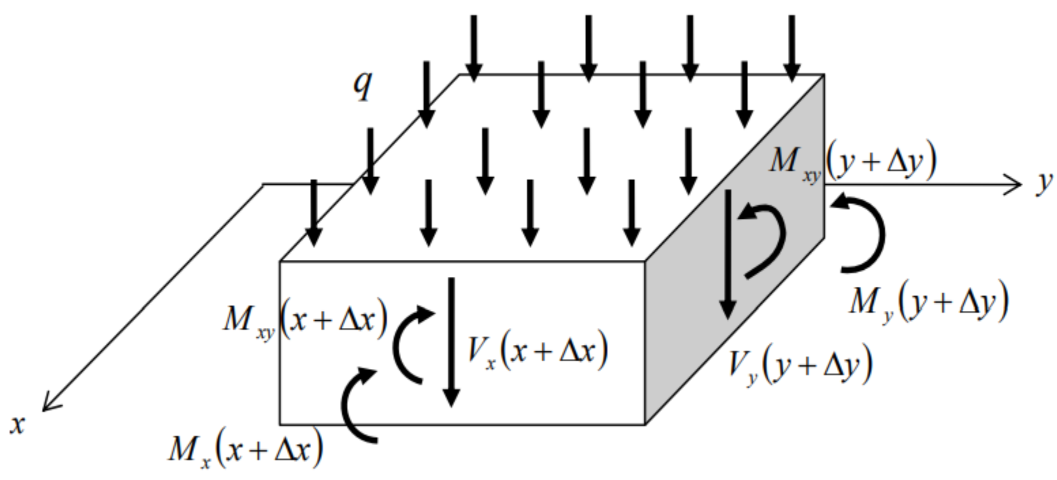

Figure 3.12 A plate element subjected to moments, pressure and shear forces

$$\sum \mathrm{F}|_z = V_y\Delta x - \left(V_y + \frac{\partial V_y}{\partial y}\Delta y\right)\Delta x + V_x\Delta y - \left(V_x + \frac{\partial V_x}{\partial x}\Delta x\right)\Delta y - q\Delta x\Delta y = 0 \tag{3.50}$$

The equation of vertical equilibrium by using the equation 3.50 to obtain, which can be represented as equation 3.51.

$$\frac{\partial \mathrm{V_x}}{\partial \mathrm{x}} + \frac{\partial \mathrm{V_y}}{\partial \mathrm{y}} = -\mathrm{q} \tag{3.51}$$

After that, the equilibrium theory of moments will be discussed and analyzed. The equation p = dV/ dx, which is used in beam theory, is comparable to this. The next step is to construct a relationship by taking moments of the x axis, which is stated in equation 3.51 and can be reduced by the vertical force in different directions, as shown in equations 3.52 and 3.53.

$$\begin{aligned}\sum \mathrm{M}|_x = {} & M_{xy}\Delta y - \left(M_{xy} + \frac{\partial M_{xy}}{\partial x}\Delta x\right)\Delta y - M_x\Delta x \\ & - \left(M_y + \frac{\partial M_y}{\partial y}\Delta y\right)\Delta x - yV_y\Delta x \\ & - (y + \Delta y)\left(V_y + \frac{\partial V_y}{\partial y}\Delta y\right)\Delta x + \left(y + \frac{1}{2}\Delta y\right)V_x\Delta y \\ & - \left(y + \frac{1}{2}\Delta y\right)\left(V_x + \frac{\partial V_x}{\partial x}\Delta x\right)\Delta y - \left(y + \frac{1}{2}\Delta y\right)q\Delta x\Delta y = 0\end{aligned} \tag{3.52}$$

$$V_x = \frac{\partial M_x}{\partial x} - \frac{\partial M_{xy}}{\partial y} \tag{3.53}$$

$$V_y = \frac{\partial M_y}{\partial y} - \frac{\partial M_{xy}}{\partial x} \tag{3.54}$$

From the equations of equilibrium, which include the force balances, it is also possible to directly derive the equilibrium relations equations 3.49 and 3.52. A solution can be obtained by taking the first of these, which ensures that the forces in the X direction are in equilibrium, multiplying it by z, and integrating it over the thickness of the plate which will result in the solution. Furthermore, due to the fact that the shearing stress σ_{zx} must be equal to zero across both the top and bottom surfaces, the equation that has to be solved in equation 3.50. It is necessary to follow a procedure that is comparable to the one that was utilized for the second equilibrium equation in order to acquire equations 3.53 and 3.54. It is possible to get at equations 3.49 and 3.52 by directly integrating the third equilibrium equation without multiplying it by z. This is the conclusion that may be drawn from the previous parts. After removing the shear forces from equations 3.49 and 3.52, the differential equation is produced, which is then expressed as equations 3.55 and 3.56. These equations are then used to describe the situation by enrolled the equation $\frac{\partial^2 M}{\partial x^2} = p$. There are instances when these equations are referred to as the Sophie Germain equation, after the french investigator who was the first to establish it in the year 1815. The boundary conditions of the issue, also known as the fixing conditions of the plate, are taken into consideration when solving this partial differential equation (for more information, see below). Also, when an expression for w(x, y) has been obtained, the strains, stresses, forces, and moments will be obtained follow in their equations. It is important to take note that the differential equation 3.58 with q=0 is easily met in the straightforward pure bending and torsion situations that were discussed earlier. The Laplacian, often known as the "del" operator, is represented by the variable ∇^2, $\nabla^2 = \frac{\partial^2}{\partial x^2} + \frac{\partial^2}{\partial y^2}$. Note that the Laplacian operator (on w) gives the sum of the curvatures in two perpendicular directions and so it is independent of the directions chosen.

$$\frac{\partial^2 M_x}{\partial x^2} - 2\frac{\partial^2 M_{xy}}{\partial x \partial y} + \frac{\partial^2 M_y}{\partial y^2} = -q \tag{3.55}$$

$$\frac{\partial^4 w}{\partial x^4} - 2\frac{\partial^2 w}{\partial x^2 \partial y^2} + \frac{\partial^2 w}{\partial y^4} = -\frac{q}{D} \tag{3.56}$$

$$\nabla^4 w = -\frac{q}{D} \tag{3.57}$$

3.4 Plate Elastic Deformation under Different Shapes

By using Cartesian coordinates, a variety of significant plate problems in this section of the article will be investigated. Within the framework of the bending theory of elastic thin plates, the effects of boundary conditions on the deformation of the thin plates are recognized. Fixed bounds, simply supported borders, and free boundaries are the three categories that can be used to classify them. The amount of deformation that occurs at the fixed boundary is the least significant of all of them. To establish the detection capability of non-destructive testing (NDT), it is necessary to determine whether or not the NDT method can be used to calculate the minimal deformation. It demonstrates that the NDT technology is also capable of detecting defects when there are only supported boundaries and free boundaries. An illustration of the clamped boundary's boundaries can be seen in equations 3.58 and 3.59 and Figure 3.13. In the subsequent chapters, the fixed boundary will serve as the point of departure for the discussion of the impact that various shapes have on the deformation of the thin plate.

$$w|_a = 0 \tag{3.58}$$

$$\left.\frac{\partial w}{\partial x}\right|_a = \left.\frac{\partial w}{\partial y}\right|_a = 0 \tag{3.59}$$

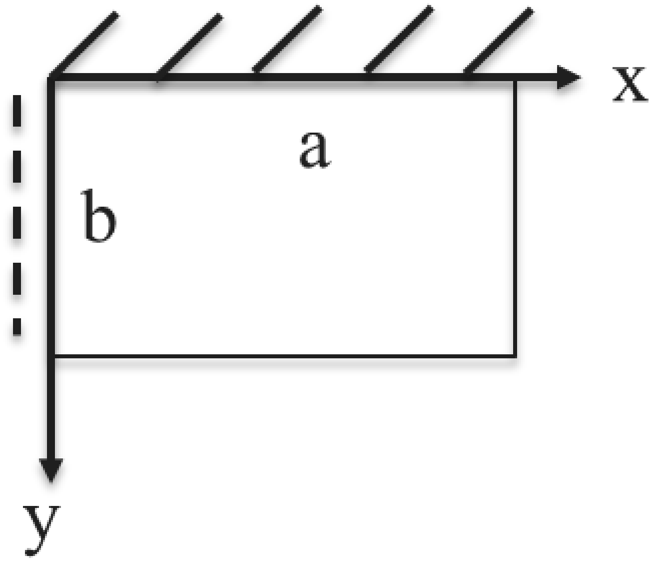

Figure 3.13 Fastened all around

3.4.1 Circular Shape

In the beginning, the circular shape defect will be implemented. At first, a solution to the problem of a circular plate deformation will be offered which will be investigated once more in the section that comes after this one, namely with the polar coordinates that are more natural. In this part, a circular plate is considered whose boundaries are clamped at the edges and is subjected to a uniform lateral load across the entire plate. The schematic is depicted in Figure 3.14, and the trajectory equation is depicted in the equation 3.60.

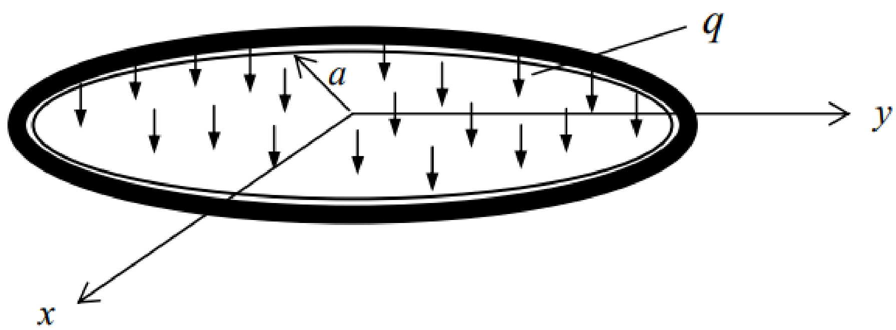

Figure 3.14 A clamped circular plate subjected to a uniform lateral load

$$x^2 + y^2 = a^2 \tag{3.60}$$

The boundary conditions are that the slope and deflection are zero at the boundary of equation 3.58 and 3.59, The trajectory equation updated to 3.61. Then convert to a solution to the problem, which shows in equation 3.62. After that, by enrolled the Sophie Germain equation which in equation 3.5), the deflection is updated to 3.63. and a parameter c was given to help understand the equation 3.64, which related to lateral loading and plate stiffness. The maximum deflection occurs at the plate center, which is expressed in equation 3.65 and Figure 3.15.

$$\mathrm{w} = \mathrm{c}(\mathrm{x}^2 + \mathrm{y}^2 - \mathrm{a}^2)^2 \tag{3.61}$$

$$\mathrm{f}(\mathrm{x}, \mathrm{y}) = \mathrm{x}^2 + \mathrm{y}^2 - \mathrm{a}^2 \tag{3.62}$$

$$\mathrm{w} = \frac{\Delta \mathrm{p}}{64\mathrm{D}}[\mathrm{a}^2 - (\mathrm{x}^2 + \mathrm{y}^2)]^2 \tag{3.63}$$

$$\mathrm{c} = \frac{\Delta \mathrm{p}}{64\mathrm{D}} \tag{3.64}$$

$$W_{max.cricluar} = \frac{\Delta p}{64D} a^4 \tag{3.65}$$

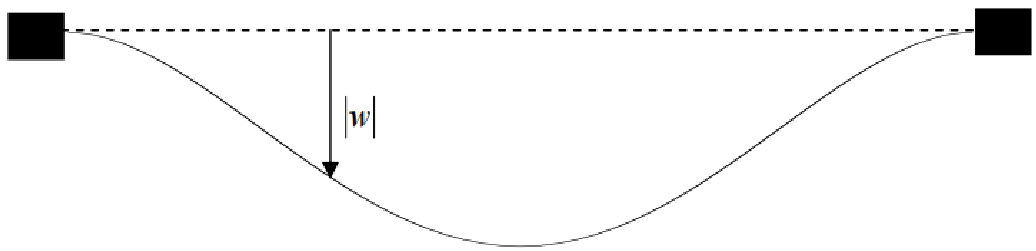

Figure 3.15 Mid-plane deflection of the clamped circular plate

3.4.2 Rectangular Shape

After that, a defect approach that was rectangular in shape will be discussed in this subsection. Along with this consideration, a square plate that has its borders clamped at its edges is being subjected to a lateral force that is maintained across the entire plate. The schematic diagram can be seen in Figure 3.16, and the equation for the boundary condition can be found in equations 3.66 & 3.67.

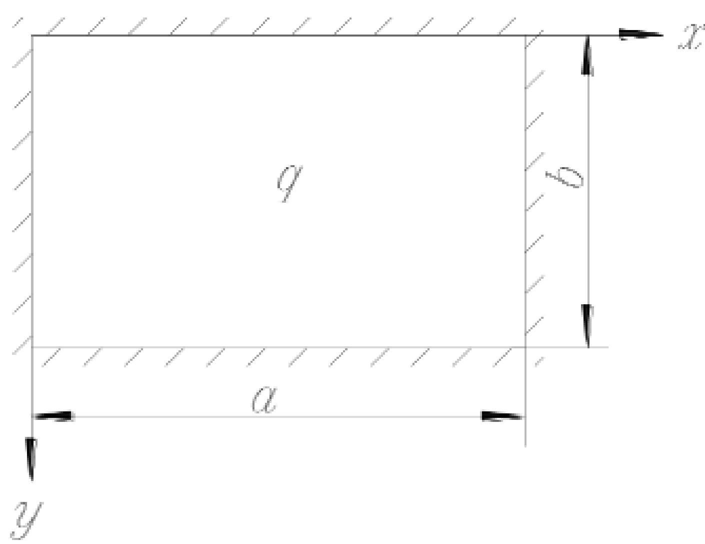

Figure 3.16 Fixed all around for rectangular shape

$$w|_0 = 0\ ; \frac{\partial w}{\partial x}\bigg|_0 = \frac{\partial w}{\partial y}\bigg|_0 = 0 \tag{3.66}$$

$$w|_a = 0\ ; \frac{\partial w}{\partial x}\bigg|_a = \frac{\partial w}{\partial y}\bigg|_a = 0 \tag{3.67}$$

The deformation-deflection function is represented by the equation 3.68, which assumes that the boundary conditions for displacement are satisfied. In the following step, the same strategy is utilized to provide the Sophie Germain equation as well as the sides a and b of the 3.70 equation. There is the possibility of converting this function into equations 3.69 and 3.70.

$$w = w_0(1 - cos\frac{\pi x}{a})(1 - cos\frac{\pi y}{b}) \tag{3.68}$$

$$w_{max.rectangular} = \frac{16\ a^4\ b^4}{\pi^4\ [3(a^4 +\ b^4) + 2a^2\ b^2]}\ \frac{\Delta p}{D} \tag{3.69}$$

$$w_{max.rectangular} = \frac{16a^4 b^4 \Delta p \cdot 12(1 - \nu^2)}{\pi^4[3(a^4 + b^4) + 2a^2 b^2] \cdot Et^3} \tag{3.70}$$

3.4.3 Oval Shape

Take into consideration, an oval plate that has its boundaries clamped at its edges and is subjected to lateral forces that are being held throughout the plate. Figure 3.17 depicts the schematic diagram, and equations 3.71 and 3.72 illustrate the boundary condition equations and Figure 3.17 provides a visual representation of the diagram. An exact solution to the elastic deformation of an elliptical thin plate can be found in equations 3.73 and 3.74, which are provided in the introduction of the Sophie Germain equation. These equations show the link between deformation, lateral load, and plate stiffness.

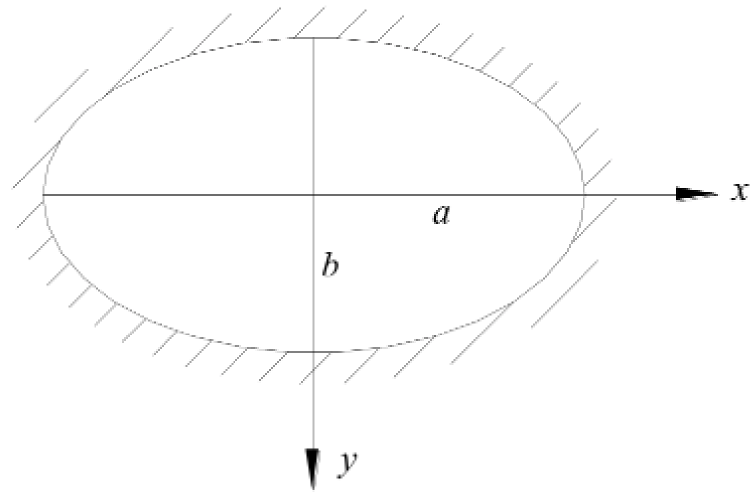

Figure 3.17 Fixed all around for oval shape

$$\frac{x^2}{a^2} + \frac{y^2}{b^2} = 1 \tag{3.71}$$

$$w = m(\frac{x^2}{a^2} + \frac{y^2}{b^2} - 1)^2 \tag{3.72}$$

$$D(\frac{24m}{a^4} + \frac{16m}{a^2b^2} + \frac{24m}{b^4}) = q \tag{3.73}$$

$$w = \frac{\Delta p(\frac{x^2}{a^2} + \frac{y^2}{b^2} - 1)^2}{8D(\frac{3}{a^4} + \frac{3}{a^2b^2} + \frac{3}{b^4})} \tag{3.74}$$

CHAPTER FOUR

DETERMINATION AND DEMONSTRATION OF THE SIZE AND DEPTH OF THE SMALLEST DETECTABLE DEFECT

In this study, a digital shearography approach is presented for the goal of identifying the size of the lowest detectable defect and the depth under various loading magnitudes for the purpose of conducting nondestructive testing. The interferometric nondestructive testing (NDT) approach known as digital shearography has been demonstrated to be an effective instrument for the inspection and evaluation of materials, particularly for the detection of delaminations and disbonds in honeycomb structures and composite materials. In the realm of non-destructive testing (NDT), one of the most frequently asked questions is about measuring sensitivity. More specifically, what is the lowest observable delamination or disbond, and how deep can these features be detected? Despite the fact that numerous attempts have been made to locate the smallest detectable defect through the use of shearography, a numerical model that can determine the size of the lowest detectable defect as well as its depth has not yet been established. Specifically for non-destructive testing (NDT) of delamination and disbond in honeycomb structures and polymers, this work conducted a study on this particular area. First, a mechanical model that was based on the thin plate theory was suggested in order to compute the expected bending of close-to-surface defects. The model constructed a relationship between the deformation that was induced by a defect, the size and depth of the defect, as well as the magnitude of load and the properties of the material. Second, the relationship between the relative deformation measured by shearography and the deformation generated by a defect was created based on the optimized shearing amount and the sensitivity of digital shearography to determine the relationship between the two types of deformation. After doing these analyses, connections were formed between the size of the lowest observable defect and the depth under various load levels for various defect forms, which associations were shown to be significant. Finally, in order to verify these correlations, experimental validation was carried out using prefabricated defects of varying sizes. The findings of the experiments indicate that the model that was built is capable of providing effective estimation for non-destructive testing (NDT) by means of digital shearography. This is particularly helpful for test engineers in estimating the size of the lowest detectable defect as well as the depth with associated loading magnitudes.

4.1 Introduction

With their exceptional strength-to-weight ratios, great resilience to corrosion and fatigue, and widespread application in the aerospace and automotive industries, honeycomb core sandwich composites and composites such as glass/carbon fiber reinforced plastic (GFRP and CFRP) are among the most popular materials in the industry. Unfortunately, these sorts of materials are prone to producing disbonds between the inner core and outer skin for honeycomb structures and delaminations between the laminated layers for GFRP and CFRP as a result of impact loading, aging, defect manufacturing, and other factors. Several non-destructive testing (NDT) techniques have already been utilized in order to check for defects of this nature [4-6]. On the other hand, the optical approaches, such as thermography, holography, electronic speckle pattern interferometry (ESPI), and shearography, are becoming increasingly popular as potential candidates for new industrial non-destructive testing (NDT) tools due to the fact that they are non-contact, non-contaminating, and have a wide field of view [5-12]. When it comes to non-destructive testing (NDT), the shearographic method appears to be the most effective and practical of these optical methods [91-95]. Shearography is a coherent-optical approach that is comparable to Holography and ESPSI. However, due to the fact that it directly measures strain information, shearography offers a number of benefits for industrial applications. (1) A rigid body movement generates a displacement, but no strain, thus, shearography is relatively insensitive to environment interruptions and it is more practical for industrial application; (2) defects in objects usually induce strain concentrations, thus, it is easier to reveal defects with strain anomalies than with displacement anomalies; (3) shearography uses a self-reference interferometric system which has low requirement for laser coherent length and enables the use of economical and practical diode laser or multi diode lasers if a larger area is inspected. Shearography has become one of the most effective non-destructive testing (NDT) tools for composite materials, particularly honeycomb structures [19,20,96]. This is due to the enormous advantages that it offers.

A digital camera is used as the recording equipment in digital shearography, which is also known as electronic shearography or TV shearography. This technique combines a variety of measurement and evaluation methods with the goal of enabling real-time measurement and quantitative evaluation of shearograms [23,97]. In the field of non-destructive testing (NDT) of composite materials, digital shearography has seen widespread application over the course of the past two decades [98-102]. Detecting disbonds in honeycomb structures and delaminations in GFRP and CFRP composite materials is the primary application of this technology [24-26]. A successful shearographic inspection is dependent on highlighting the contribution of defect-induced surface deformation and the smallest observable deformation of the shearographic system. This is true despite the fact that digital shearography offers a great deal of benefits. The defect-induced deformation is a complicated parameter that is connected to the loading magnitude, the loading method, the shearing amount, the size of the defect, the depth of the defect, the shape of the defect, and so on [27]. A significant number of researchers have carried out investigations on shearographic non-destructive testing (NDT) for a variety of diameters and/or depths under a variety of loading methods throughout the course of the previous two decades.

In order to investigate the capability of the shearoghraphy, the literature is investigated and analyzed. Identifying the shearography sensitivity limitation can be accomplished in a few different methods. The finite element method (FEM) is one of the most investigated methods for simulating the deformation, and shearography is used to verify the simulation in order to determine the shearography sensitivity. The modeling of an opto-mechanical measurement system was reported by Dr. Krutul and colleagues [28]. They developed a finite element method (FEM) model to obtain the dynamic mechanical response of the sample when it was subjected to thermal loading. Additionally, they generated a shearography fringe pattern. After that, they verified and compared the model with the shearography measurement system in order to evaluate the quality of the model. In this section, the author presents a variety of boundary conditions and compares the results obtained after unwrapping the data. The generated phase maps and the phase maps that were found through experimentation exhibited a fair resemblance in form. On the other hand, the real data exhibits the asymmetry properties that were seen in the experimental phase maps. It is also important to note that simulated data is not identical to actual data. The only thing that was stated was thermal loading, and it was not detailed enough. Do not take into account the possibility of defects, which could lead to the information being missing at the end.

A new numerical-experimental model was described by Dr. G. De Angelis and colleagues for the purpose of detecting different sizes and depths of flat bottom holes in metallic and laminated composite structures through the use of digital shearography [29]. The model is based on the dynamic response of a defect to applied stress, and according to the theory, the digital shearography results will produce different responses depending on the layer depth. This is due to the fact that the vibration dynamic loading varies from one layer to the next in CFRP layers. By using a simple model to calculate the natural frequency of the vibration defect, the depth of the defect can be determined. In spite of this, it is necessary to conduct tests on a comparable good plate in order to determine its actual frequency, which is not only time consuming but also not accurate enough.

To ensure that this inspection approach yields the best possible results, it is essential to make sure that the loading parameters are adjusted in a manner that is both accurate and precise. An additional numerical-experimental model was described by D. Akbari et al. for the purpose of testing defective materials by digital shearography based on thermal loading [30]. The FEM method was utilized in the paper in order to simulate shearographic fringe patterns. The approach constructed a finite element method (FEM) model in order to acquire the dynamic mechanical response of the sample when it was subjected to thermal loading. Then, the method generated a shearography fringe pattern by FEM, which was then checked and compared with the shearography measurement equipment in order to evaluate the accuracy of the model. The program denoises the fringe pattern and avoids changes in environmental variables, such as unnecessary displacement or vibration when these photos were acquired, which would render the results worthless. However, the results that the denoising technique is not as good as it should be, and the asymmetry problem for simulation is also not solved. When errors occur, the technology records some additional information or deletes some useful information.

X. Chen et al. (2015), Y. Fu et al. (2017), and J.F. Vandenrijt et al. (2019) have reported hybrid approaches that are based on experimental and computational investigations, employing shearographic test findings and finite element analysis software and/or MATLAB to anticipate internal defects [31-33]. These methods also use shearographic test data. A systematic study to show the relationships between the size of the smallest detectable defects and the depths of the defects under different magnitudes of loading for NDT by the shearographic testing method has not yet been conducted, despite the fact that these studies have provided useful information in the field of shearographic non-destructive testing (NDT). In this research, a comprehensive mechanical numerical model to quantitatively illustrate the correlations between the size of the smallest observable defects and the depths under different loading magnitudes for non-destructive testing (NDT) using the shearographic testing method. Initially, a mechanical model was constructed that was founded on the principles of elastic mechanics and thin plate deformation theory. After that, the differential equation of the deformation as well as the solutions of the deformation were presented for a variety of defect shapes under specified boundary conditions. Although thermal loading is the most straightforward technique of loading, vacuuming or applying some internal pressure is a more efficient loading method. This is due to the fact that this type of loading will tear apart disbonds and delaminations, which will result in a bigger surface deformation and enable non-destructive testing (NDT) of defects easier to do. In order to determine the size of the smallest detectable defect and the depth based on the smallest measurable deformation or the relative deformation of digital shearography, numerical equations were constructed using this loading approach. These equations were used to determine the diameter of the defect. The numerical equations were validated using experimental validation, and the results were consistent with the equations.

4.2 Digital Shearography for Non-Destructive Testing (NDT)

4.2.1 Principle of shearography for NDT

Identifying interior defects or delaminations is the primary objective of shearography for non-destructive testing (NDT). This is accomplished by detecting surface anomalies resulting from the distribution of w, which is induced by a modest force. The operation of the shearography for NDT is depicted in Figure 4.1. When an object that has an internal defect (shown in Figure 4.1 a) is loaded, for example by a vacuum loading (shown in Figure 4.1 b), the surface in the defect region will produce a significantly bigger deformation (shown in Figure 4.1 c) than the surface in other places, and the maximum deformation will occur in the middle of the defect area. A relative deformation denoted as "Δw" is measured by shearography between two sites that have a shearing amount (as shown in Figure 4.1 d). In the event that the shearing amount chosen is equal to or greater than the size of the defect, the maximum relative deformation Δw_{max}

that is recorded by shearography is equivalent to the maximal deformation that occurs in the defect area, which is represented by the symbol w_{max}, as depicted in Figure 4.1 d. Generally, the lowest sized defect that ought to be recognized is either already known or is predetermined by the properties of the materials. As a result, an optimal shearing amount can be chosen, and the maximum measurable relative deformation is the maximum deformation Δw_{max} in the defect area.

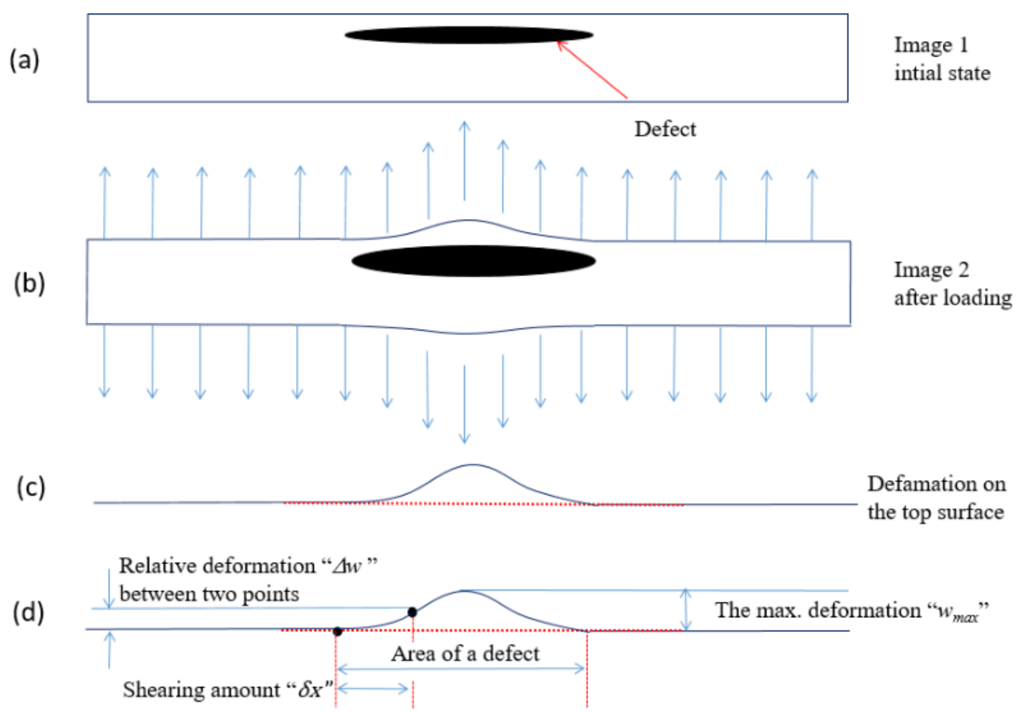

Fig. 4.1. Fundamentals of shearography for NDT: (a) an object with a defect, (b) deformation after a loading, (c) the shape of the deformation, and (d) relationship between the relative deformation and the shearing amount

Now, the question that needs to be answered is, what kinds of defects can be discovered? In the event that the deformation that is brought about by a loading in the defect area is greater than the smallest quantifiable deformation w_{max} that can be determined by digital shearography, then it is expected that defects of this nature will be recognized. Depending on the test environment, the hardware setup, and the software method, the smallest quantifiable deformation w_{max} can range anywhere from $\lambda/10$ and $\lambda/20$. There is a connection between the deformation that is brought about by the loading and the defect size S, the depth t from the surface, the characteristics of the material, and other factors (Fig. 4.5). In order to determine the smallest defect that can be detected, it is necessary to do an analysis of the relationship that exists between these characteristics.

4.2.2 Relationship among the deformation caused by loading, the size and depth of the smallest detectable defect

4.2.2.1 Mechanical model

Before beginning to analyze the relationship between the deformation that is generated by loading in the defect area and the size and depth of the smallest observable defect, it is necessary to first investigate a numerical method that can calculate the deformation. Figure 4.2 illustrates the deformations that occur when a disbond occurs between a surface sheet and a honeycomb core in a honeycomb structure. Additionally, delamination occurs in a CFRP or GFRP panel when it is subjected to a pulling force, such as a vacuum loading of the panel. In this context, it is important to stress that the study is predicated on the fact that the defect is located relatively close to the surface of the object. It is imperative that the depth of the defect, denoted as t, is less than one fifth to one eighth of the defect size, and that the loading is orthogonal to the surface. The top parts of the defects can be counted as plates if these assumptions are taken into consideration. These deformations are identical, from a mechanical point of view to the deformation of the plate when it is subjected to a loading of internal pressure, as depicted in Figure 4.3. Assuming that the size of the hole underneath the plate is S and that S = 2a (where a represents the radius of a circular shape or the half side of a rectangular shape) and that the thickness of the top plate is t, the deformation depicted in Figure 6 can be considered to be an approximation of the model of deformation in the region of the disbond or the delamination depicted in Figure 4.2.

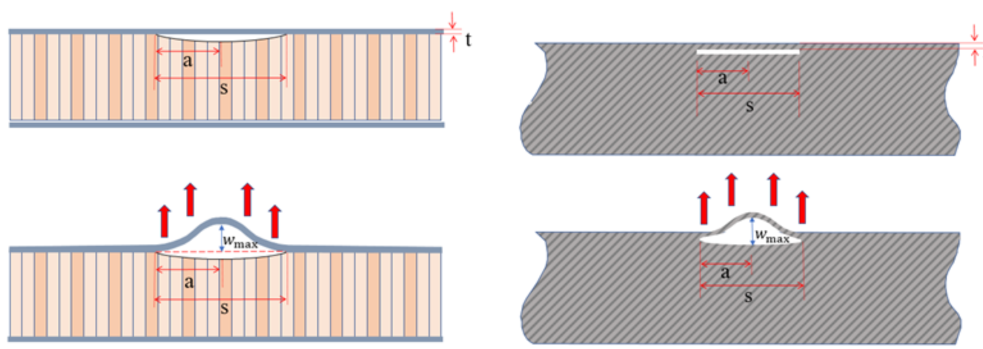

Fig. 4.2. Defects and the deformation under a pulling force: a disbond in a honeycomb structure (left), and a delamination in a CFRP/GFRP panel (right)

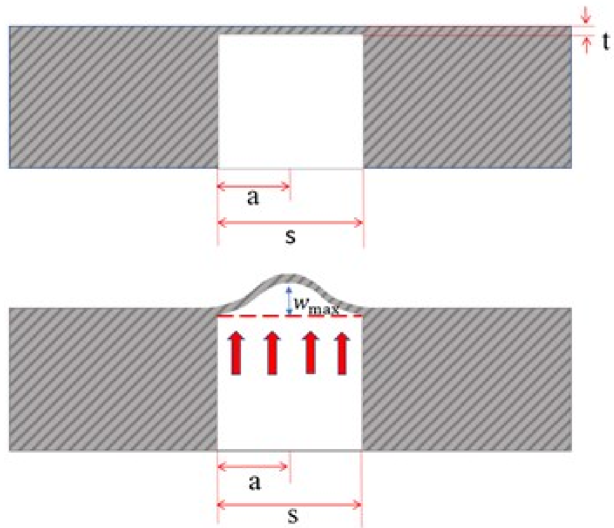

Fig. 4.3. An equivalent deformation for a plate with a hole underneath under an internal pressure.

If the loading is perpendicular to the surface and the thickness t is much smaller than the size of S [t < (1/5~1/8) xS], the upper part of the hole can approximately be regarded as a plate fastened all around under pure bending and twist. According to the elastic deformation mechanics of the thin plate theory, the differential equations of the deformation for the plate shown in Fig. 4.6 is given by [103]:

$$\nabla^2\nabla^2 \mathrm{w} = \frac{\Delta \mathrm{p}}{\mathrm{D}} \tag{4.1}$$

where w is the out-of-plane deformation, Δp is the magnitude of internal pressure, D is the flexural rigidity, ∇^2 and D are shown as follows:

$$\nabla^2 = \frac{\partial^2 w}{\partial x^2} + \frac{\partial^2 w}{\partial y^2} \tag{4.2}$$

$$D = \frac{E\, t^3}{12\,(1 - \nu^2)} \tag{4.3}$$

E represents the elastic modulus of the material, ε represents the Poisson ratio, and t represents the thickness of the plate, which is comparable to the depth of defects. This equation can be found in equation 4.3. In order to get the solution to equation 4.1, it is necessary to consider the shape of the defect, the loading mechanism, and the boundary conditions. Within the scope of this research investigation, the defects in two different shapes will be discussed: one is circular, and the other is either rectangular or square.

4.2.2.2 Deformations of defects with different shapes

Oval defect

Let's talk about oval shape defects first. Assuming that the circular defect has a radius of "*a*", its depth is *t*, and the origin of coordinates is in the middle of the defect, the magnitude and methods of loading and the boundary conditions are listed below:

- Loading method: internal pressure (a uniform load),
- Boundary conditions: Fastened all around, i.e. $w|_{x=a} = 0$, $\partial w/\partial x|_{x=a} = 0$,

Under these conditions, the solution of differential equation 4.3 for deformation *w* is given by [104]:

$$\frac{x^2}{a^2} + \frac{y^2}{b^2} = 1 \tag{4.4}$$

and the maximum deformation w_{max} occurs in the middle of the plate, i.e. at x = 0 and y = 0:

$$w = \frac{\Delta p(\frac{x^2}{a^2} + \frac{y^2}{b^2} - 1)^2}{8D(\frac{3}{a^4} + \frac{3}{a^2b^2} + \frac{3}{b^4})} \tag{4.5}$$

where Δp is the magnitude of the internal pressure, a is the radius of the defect which is half of the size of the defect *S*, i.e. $S = 2a$. Substituting equation 4.3 for the flexural rigidity D in equation 4.5, the maximum deformation w_{max} can be rewritten as follows:

$$w = 0.09375 \frac{\Delta p \cdot (1-\nu^2)}{(3+3r^2+3r^4)Et^3} s^4 \tag{4.6}$$

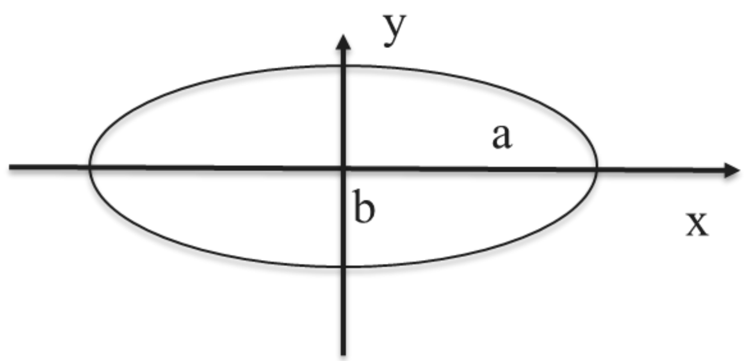

Figure 4.4 Fastened all around for oval shape

Then, the deformation of a defect with a circular shape will be discussed. Assuming that the circular defect has a radius of "*a*", its depth is *t*, and the origin of coordinates is in the middle of the defect, the loading and the boundary conditions are listed below:

- Loading method: internal pressure (a uniform load),
- Boundary conditions: Fastened all around, i.e. $w|_{x=a} = 0$, $\partial w/\partial x|_{x=a} = 0$,

Under these conditions, the solution of differential equation 4.3 for deformation *w* is given by:

$$w = \frac{\Delta p}{64\, D} \left[a^2 - (x^2 + y^2) \right]^2 \tag{4.7}$$

and the maximum deformation w_{max} occurs in the middle of the plate, i.e. at x = 0 and y = 0:

$$w_{max}\Big|_{circular} = \frac{\Delta p}{64\,D}\; a^4 \qquad (4.8)$$

where Δp is the magnitude of the internal pressure, a is the radius of the defect which is half of the size of the defect S, i.e. $S = 2a$. Substituting equation 4.3 for the flexural rigidity D in equation 4.8, the maximum deformation w_{max} can be rewritten as follows:

$$w_{max}\Big|_{circular} = 0.01172\; \frac{(1-\nu^2)}{E}\; \frac{S^4\,\Delta p}{t^3} \qquad (4.19)$$

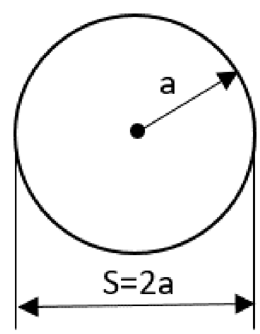

Figure 4.5 Fastened all around for circular shape.

Rectangular and square defect

If the defect is a rectangular shape with a size of 2a x 2b (2a is the long side and 2b the short side) under the same loading method (i.e. an internal pressure) and boundary conditions (i.e. fastened all around) as the circular defect, the maximum deformation in the middle of the plate is given by:

$$w_{max}\Big|_{rectangular} = \frac{16\,a^4\,b^4}{\pi^4\,[\,3(a^4 + b^4) + 2a^2\,b^2]}\;\frac{\Delta p}{D} \qquad (4.10)$$

If the ratio of the short side 2b to the long side 2a is denoted r (r = 2b/2a) and the defect size S is expressed as 2a, equation 4.11 can be simplified by substituting equation 4.3 for D:

$$w_{max}\big|_{rectangular} = 0.01543\ \frac{8\,r^4}{[3r^4 + 2r^2 + 3]}\ \frac{(1-v^2)}{E}\ \frac{S^4 \Delta p}{t^3} \tag{4.11}$$

For a square defect $a = b$, i.e. $r = 1$, equation 4.11 can further be simplified as:

$$w_{max}\big|_{square} = 0.01543\ \frac{(1-v^2)}{E}\ \frac{S^4\ \Delta p}{t^3} \tag{4.12}$$

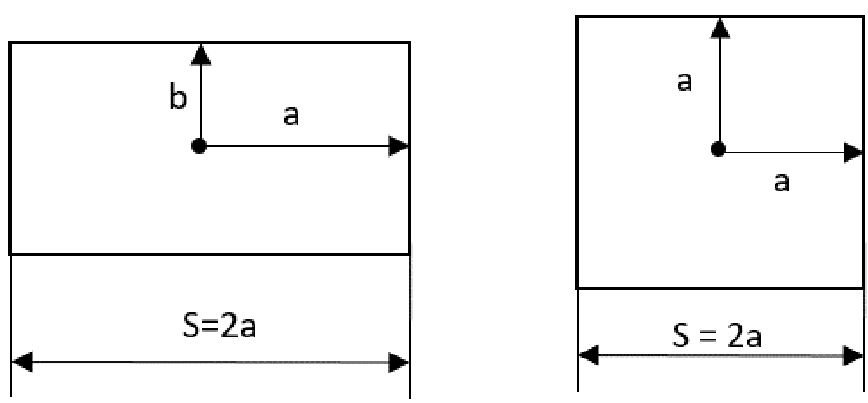

Figure 4.6 Fastened all around rectangular shape

4.2.2.3 Equilibrium and Lateral Loading

The equations 4.9–4.12 illustrate the link between the maximum deformations in the middle of the defects and the properties of the material, the size and depth of the defects, and the amount of the loading for defects that have circular, rectangular, and square geometries, respectively. Additionally, it is possible to rewrite them as an expression of the depth of the defect, denoted as t, in terms of the defect size, denoted as

S (S = 2a), the loading, denoted as p, and the greatest deformation in the middle of the defects, denoted as w_{max}.

$$t^3 = \frac{\Delta p \cdot S^4}{64 \cdot \frac{u_{max} - 12(1-\nu^2)}{E}} \tag{4.13}$$

$$t\,(S, \Delta p, w_{max})\,\Big|_{circular} = 0.22714\,[\frac{(1-\nu^2)}{E}]^{\frac{1}{3}}\,[\frac{S^4\,\Delta\,p}{w_{max}}]^{\frac{1}{3}} \tag{4.14}$$

$$w_{max.rectangular} = \frac{16\,a^4\,b^4}{\pi^4\,[3(a^4 + b^4) + 2a^2\,b^2]}\,\frac{\Delta p}{D} \tag{4.15}$$

$$t\,(S, \Delta p, w_{max})\,\Big|_{rectangular} = 0.24896\,[\frac{8\,r^4}{[3r^4 + 2r^2 + 3]}]^{\frac{1}{3}}[\frac{(1-\nu^2)}{E}]^{\frac{1}{3}}\,[\frac{S^4\,\Delta\,p}{w_{max}}]^{\frac{1}{3}} \tag{4.16}$$

$$w_{max.rectangular} = \frac{16a^4b^4\Delta p \cdot 12(1-\nu^2)}{\pi^4[3(a^4 + b^4) + 2a^2b^2] \cdot Et^3} \tag{4.17}$$

$$t\,(S, \Delta p, w_{max})\,\Big|_{square} = 0.24896\,[\frac{(1-\nu^2)}{E}]^{\frac{1}{3}}\,[\frac{S^4\,\Delta\,p}{w_{max}}]^{\frac{1}{3}} \tag{4.18}$$

If a defect is subjected to a certain loading that results in a deformation, and the maximum deformation w_{max} at the center of the defect, as given in the equations above, achieves the smallest measurable deformation by shearography, then such a defect can be identified by the use of shearography. When the smallest measurable deformation value, also known as the measuring sensitivity of deformation, is substituted into the equations for w_{max}, the associated values of S and t are the size of the smallest detectable defect and the depth of the defect, respectively. As a result, the equations 4.13–4.18 can be used to calculate the relationships between the size of the smallest observable defect S and the depth of the defect t under a vacuum or a pressure loading which used for test different shapes of defects that include circular, rectangular, and square shapes, respectively.

What is the measuring sensitivity of deformation by digital shearography? Shearography measures a relation deformation Δw. In the intensity subtraction method, the measuring sensitivity of Δw is $\lambda/2$, whereas it can reach 5 to 10 times higher if a phase shift technique is introduced, depending on different conditions such as the test environment, the optical setup, and the software algorithm. Although 10 times higher measuring sensitivity needs an optimized condition, it is relatively easy to reach 5 to 6 times higher measuring sensitivity, i.e. the measuring sensitivity of Δw reaches to $\lambda/10$ to $\lambda/12$. According to the discussion in section 4.2.1, if the shearing amount is selected as a half size or bigger than half the size of a defect, the maximum relative deformation Δw measured by shearography is equal to the maximal deformation in the defect area as explained in Figure 4.1 d, i.e. the measuring sensitivity of digital shearography for a relative deformation is actually equal to the measuring sensitivity of w_{max}. In order to find the defect, the w_{max} caused by a loading should bigger than the measuring sensitivity of shearography, e.g. from $\lambda/10$ to $\lambda/12$.

Substituting the w_{max} with $\lambda/12$, the relationships between the size of the smallest detectable defect *S* and the depth *t* can be determined by equations 4.13–4.18 for defects with circular, rectangular and square shapes, respectively. If an He-Ne laser is used in the setup, the value of $\lambda/12 \approx 53$ nm. Figures 4.7 -4.9 show these relationships under different loading magnitudes if the material is aluminum, i.e. E = 70 GPa, $\nu = 0.33$. The data in the x- and y-axes in the figures represent the size of the smallest detectable defect and the depth, respectively. The right part below the curves stands for the sizes of defects which are bigger than the smallest detectable defect, and thus the defects are detectable and considered visible. The left part above the curve stands for the sizes of defects which are smaller than the smallest detectable defect, and thus the defects are not detectable, and considered invisible. Using different material properties (i.e. the Young's Module "E" and the passion ratio "ν"), the curves for different materials, such as for GFRP or CFRP panels, can be created based on equations 4.13 – 4.18.

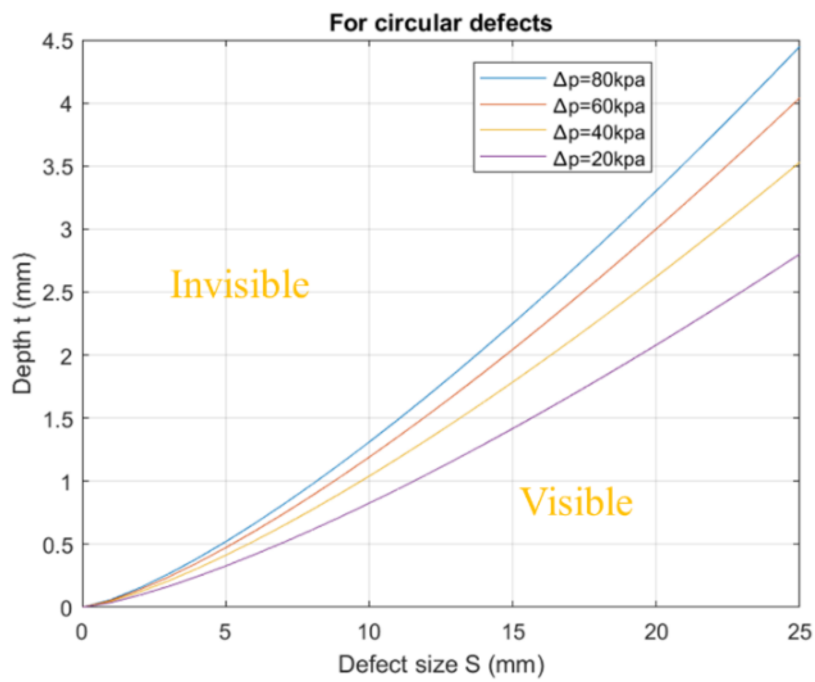

Figure. 4.7 Relationships between the size of the smallest detectable defect S and the depth t with a ***circular*** defect shape under different pressures (E=70 GPa, ν=0.33 and w_{max}=53 nm)

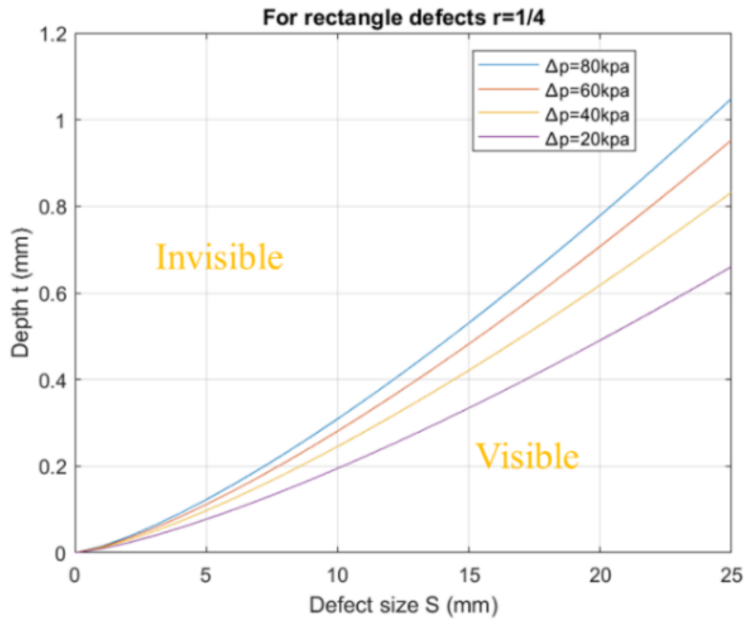
For rectangle defects r=1/4
Δp=80kpa
Δp=60kpa
Δp=40kpa
Δp=20kpa
Invisible
Visible
Depth t (mm)
Defect size S (mm)
1.2
1
0.8
0.6
0.4
0.2
0
0
5
10
15
20
25

(a)

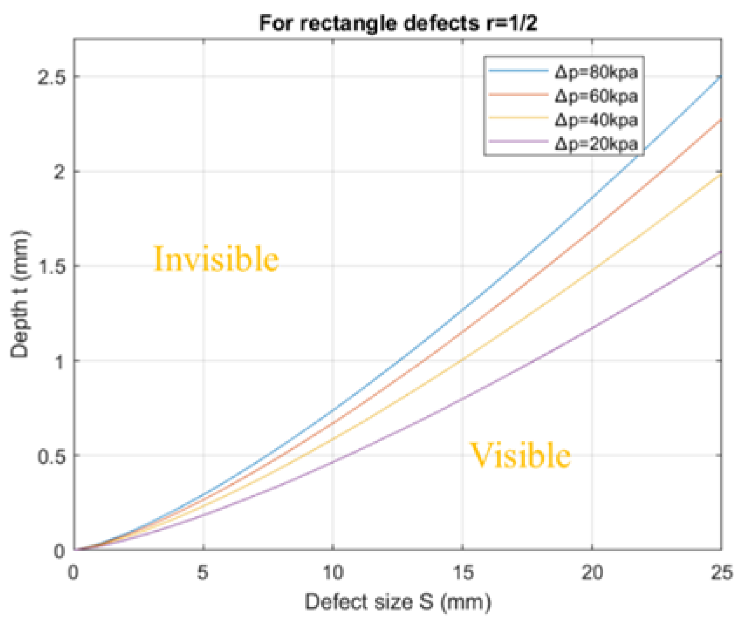
For rectangle defects r=1/2
Δp=80kpa
Δp=60kpa
Δp=40kpa
Δp=20kpa
Invisible
Visible
Depth t (mm)
Defect size S (mm)
2.5
2
1.5
1
0.5
0
0
5
10
15
20
25

(b)

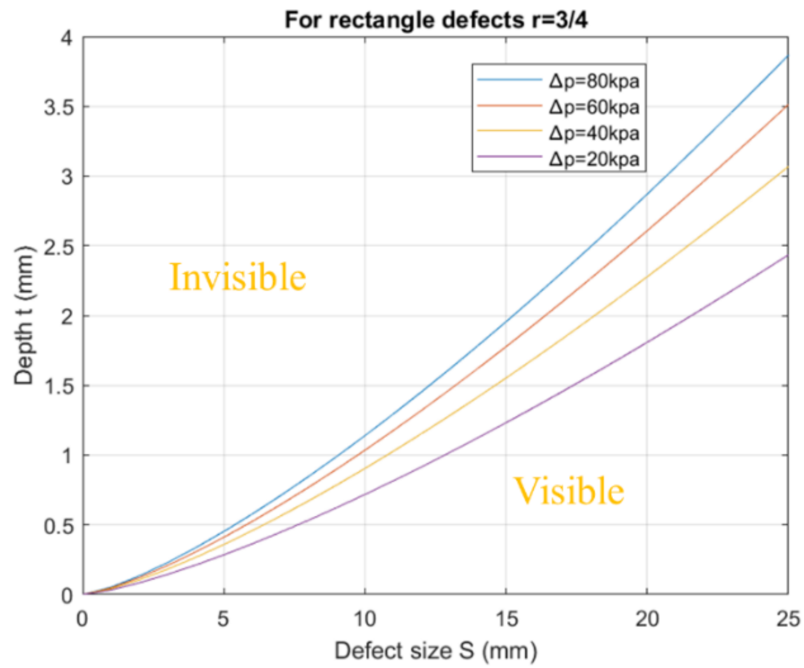

(c)

Figure. 4.8. Relationships between the size of the smallest detectable defect *S* and the depth *t* with a rectangular defect shape at different *r* values ($r = b/a$, E=70 GPa, ν=0.33 and w_{max}=53 nm)

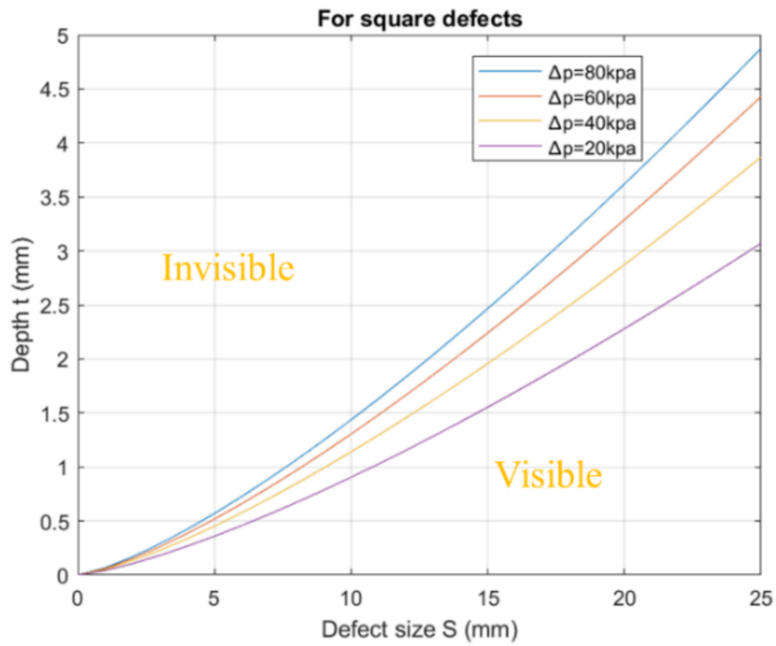

Figure. 4.9. Relationships between the size of the smallest detectable defect S and the depth t with a square defect shape under different pressure (E = 70 GPa, =0.33 and w_{max}= 53 nm)

4.3 Experiments

4.3.1 Specimen preparation

Flat-bottomed holes of varying depths and sizes were used to replicate defects in aluminum plates with a total thickness of 12.7 mm (0.5 in) and a diameter of 166 mm. This was done in accordance with equation 4.14. One specimen had five cylindrical holes drilled into it at a depth of 12.2 millimeters, with diameters ranging from 3, 4, 5, 5.9, and 8.2 millimeters. The other specimen had five holes drilled into it at a depth of 11.7 millimeters, with diameters ranging from 5, 5.9, 8.2, 9.9, and 12 millimeters, respectively. For the first specimen, the depth of the five simulated defects is t = 0.5 mm, and for the second specimen, the depth is t = 1 mm which boundary conditions for both specimens are fixed all around.

Flat-bottomed holes of varying depths and diameters were used to replicate defects in aluminum plates with a total thickness of 12.7 mm (0.5 in) and a diameter of 166 mm. This was done in accordance with equation 4.14. One specimen had five cylindrical holes drilled into it at a depth of 12.2 millimeters, with diameters ranging from 3, 4, 5, 5.9, and 8.2 millimeters. The other specimen had five holes drilled into it at a depth of 11.7 millimeters, with diameters ranging from 5, 5.9, 8.2, 9.9, and 12 millimeters, respectively. For the first specimen, the depth of the five simulated defects is t = 0.5 mm, and for the second specimen, the depth is t = 1 mm. The boundary conditions for both specimens are fixed all around. A sample with a thickness of one millimeter is seen in Figure 4.10. Fixing is accomplished through the utilization of the six penetrating holes that are evenly spaced over the outer ring. In order to imitate five defects of varying sizes, the remaining five blind holes inside are employed this way.

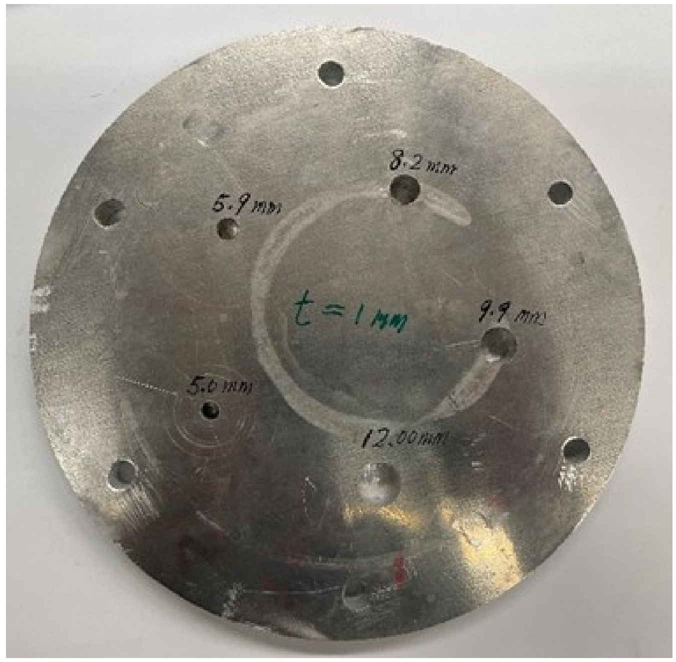

(a)

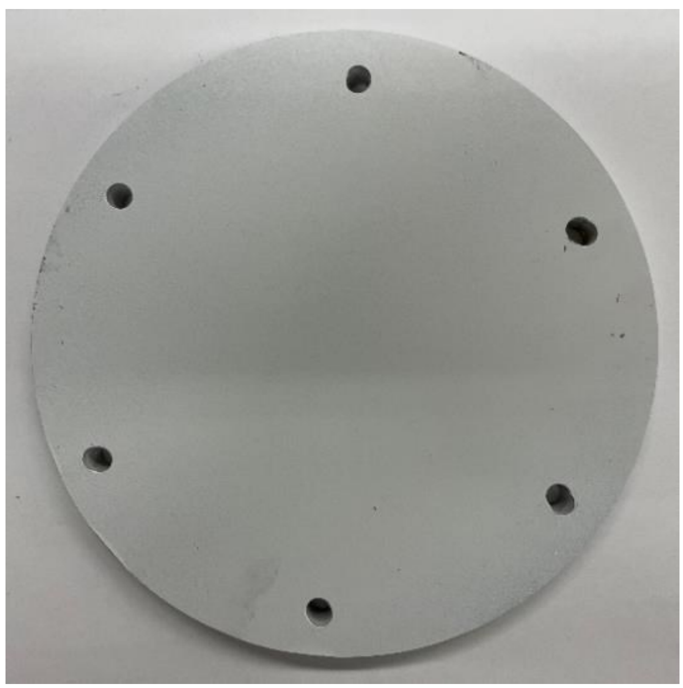

(b)

Figure. 4.10. The specimen of t = 1 mm with 5 simulated defects made by 5 flat bottomed blind holes of different diameters, left: back side, right: front side to be tested

4.3.2 Experimental setup and results

The setup for the experiment is depicted in Figure 4.14. In order to establish a pressure load, the aluminum plate was secured inside of a cylindrical chamber that was connected to a pressure pipe. After being irradiated by an extended He-Ne laser with a wavelength of 632.8 nm and a power output of 50 mW, the front surface of the aluminum plate was subjected to digital shearography using the phase shift technique. There are one mega pixel numbers in the camera, and the shearing device is a modified Michelson Interferometer. For the phase shift approach, a piezoelectric transducer (PZT) driven mirror is utilized in the shearing device. The shearing direction is occurring in the x-direction; nevertheless, according to the findings of this research, the shearing direction does not have an impact on the outcomes of the test if the defect is of a circular, square, or rectangular shape. In situations where the defect is a narrow and lengthy slot that is significantly larger than the shearing amount, the shearing direction will have an effect on the test result. It is recommended that to consult the literature [105] for information regarding shearographic tests of narrow and lengthy defects. The shearing amount is six millimeters, which is greater than fifty percent of the diameter of each hole in both of the specimens respectively. As a result of restricted manufacturing capabilities inside the facilities, cylindrical holes with flat bottoms were only able to be produced by the research team; in other words, this test only conducted experiments on defects that had a circular shape.

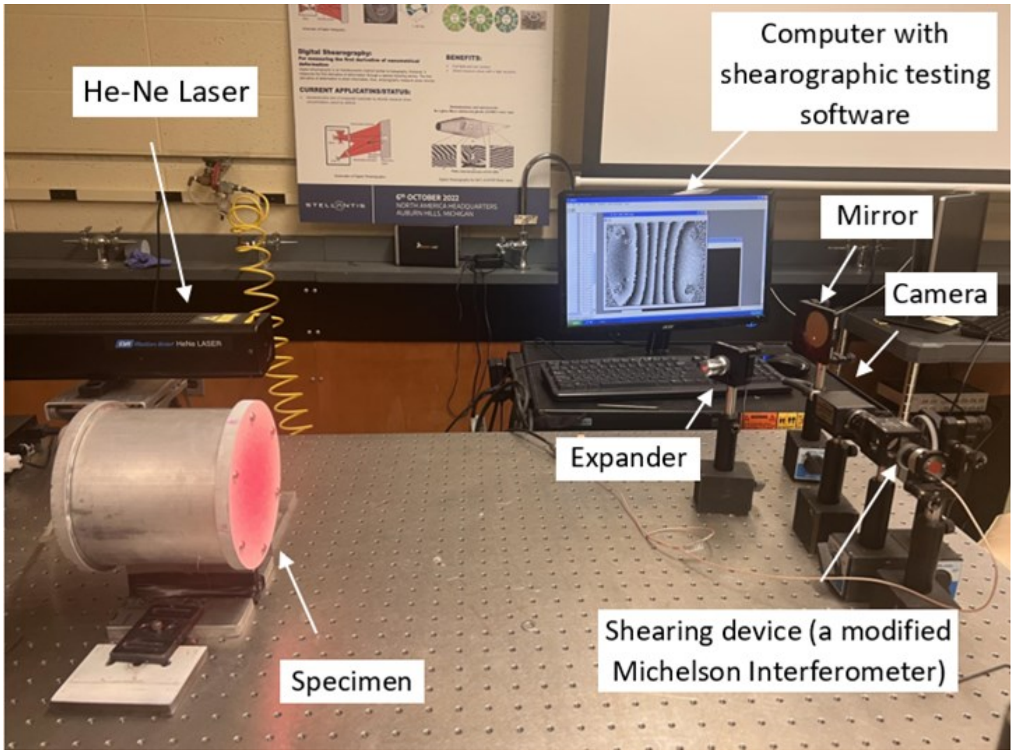

Figure. 4.11. The setup of digital shearography for the experimental validation

The shearographic test results for the aluminum plate with five prefabricated defects are displayed in Figure 4.12. The depth of the defects is 1 millimeter, and their size (diameter) ranges from 5 millimeters. 5.9 millimeters, 8.2 millimeters, 9.9 millimeters, and 12 millimeters, respectively. As soon as the internal pressure $\triangle p$ reaches a value of 80 kPa, it is possible to identify three out of the five defects. These defects are denoted by the red circles and have a size of 8.2, 9.9, and 12 millimeters, respectively. It is important to take note that the noisy spots in the outer ring are not defects; rather, they are the locations of the fastening studs illustrated in Figure 4.10 respectively. The measurements were zoomed in to each defect area, which was approximately 65 millimeters by 50 millimeters, in order to enhance the amount of pixels that lay between two neighboring fringes which was done in order to clearly display the results with a better spatial resolution. The display in the small region is able to improve its spatial resolution from around 7 pixels per millimeter to approximately 15 pixels per millimeter by utilizing a camera with a resolution of one megapixel. A high spatial resolution results in a greater number of pixel numbers between two adjacent fringes, and a greater number of pixels results in a greater number of grayscale points or values between that pair of fringes. The shearography pattern known as the butterfly fringe pattern becomes more distinct as a result of this. The shearograms that were measured in each defect area of the aluminum plate at $\Delta p = 80$ kPa are shown in Figure 4.13, which is a comparison between the simulated curve of the least detectable defect size at $t = 1$ mm and the shearograms that were obtained at that pressure. There are five simulated defects on the aluminum plate, and their sizes (diameters) range from $S = 5$ to $S = 5.9$ to 8.2 to 9.9 to 12 mm. These sizes correlate to the five shearograms that are located in each defect area, which are arranged from left to right. At a time of 1.0 millimeters, the numerical curve and the experimental findings are in agreement. At the thickness and loading that have been specified, the numerical curve indicates that the only defects that can be discovered are those that are larger than 8 millimeters, and the actual results have also demonstrated this. However, the shearograms in the areas with defect sizes of 5.0 mm and 5.9 mm do not show a butterfly pattern, which means that these two defects cannot be detected (see the two shearograms on the left). On the other hand, the three shearograms on the right show a clear butterfly pattern, which indicates that defects of size 8.2, 9.9, and 12 mm can be detected.

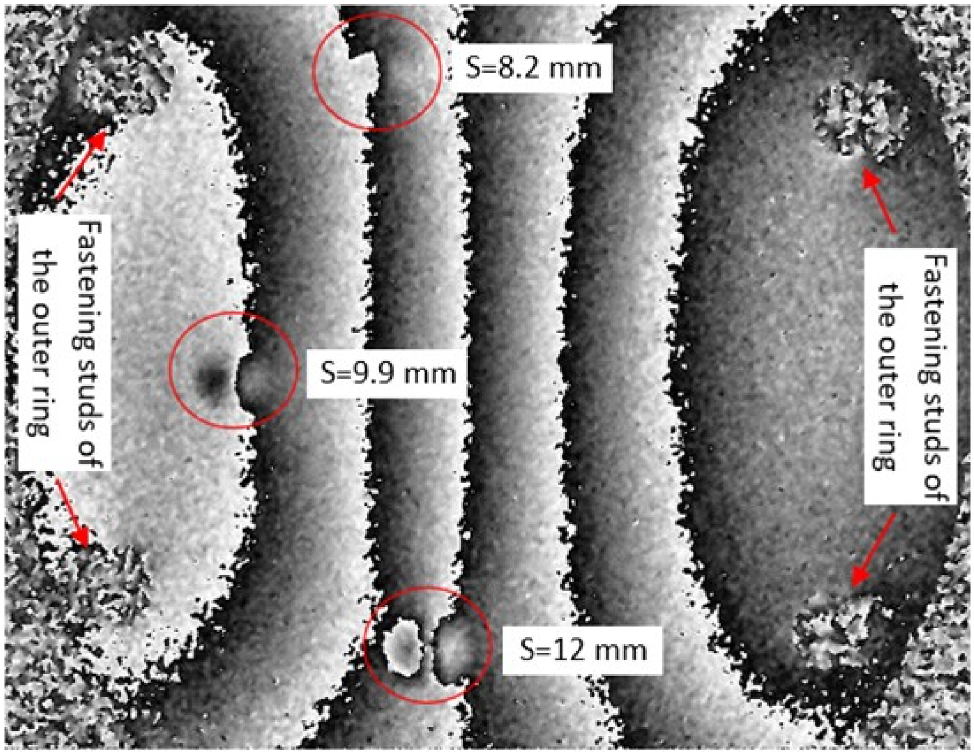

Figure. 4.12. Shearographic test results for the aluminum plate with five prefabricated defects whose thickness is t =1 mm, and three of which were founded at Δp = 80 kPa

Figure. 4.13. A comparison between the simulated curve and the shearograms measured in the area of each defect of the aluminum plate with five prefabricated defects at t = 1 mm and Δp = 80 kPa.

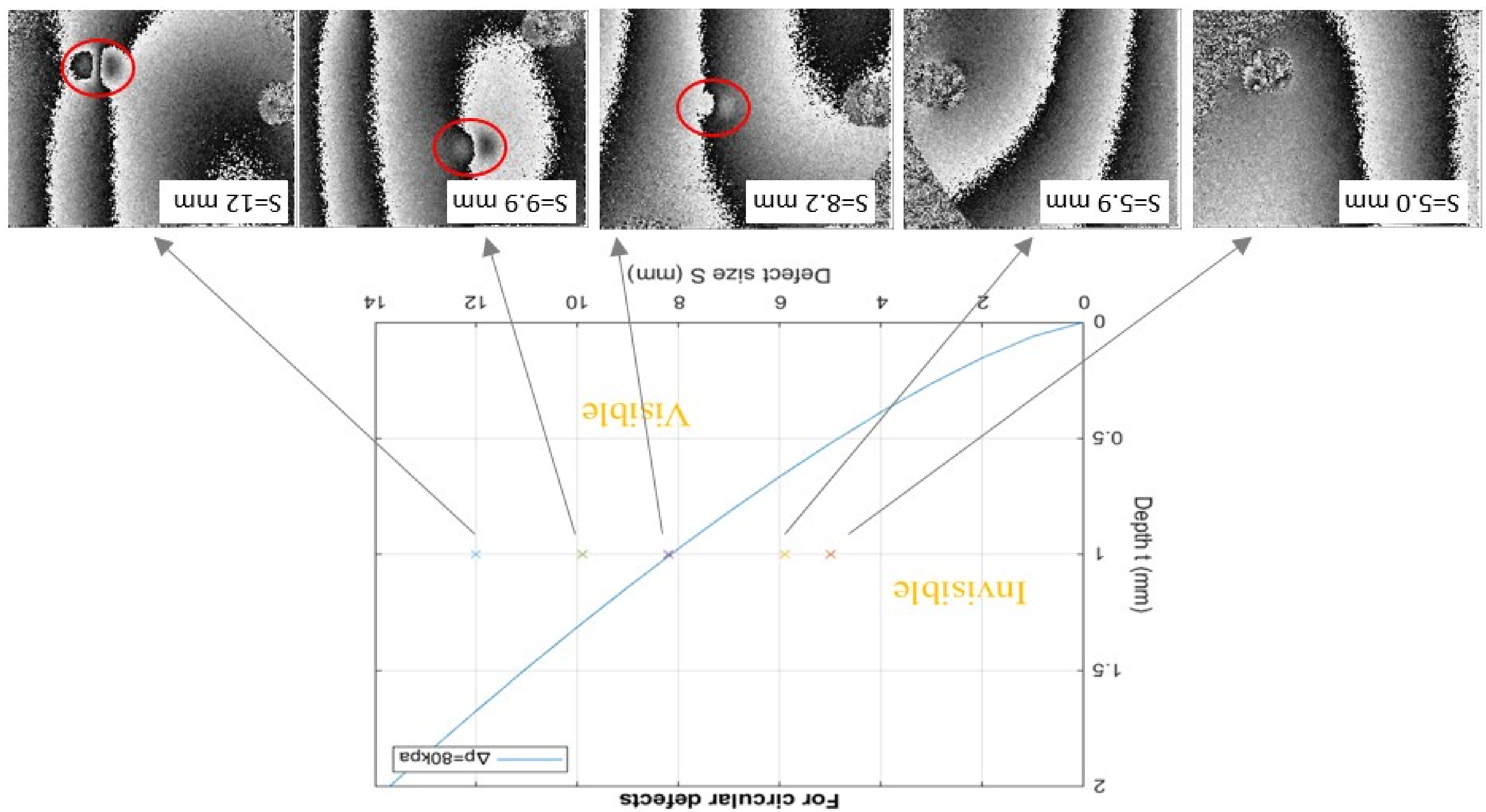

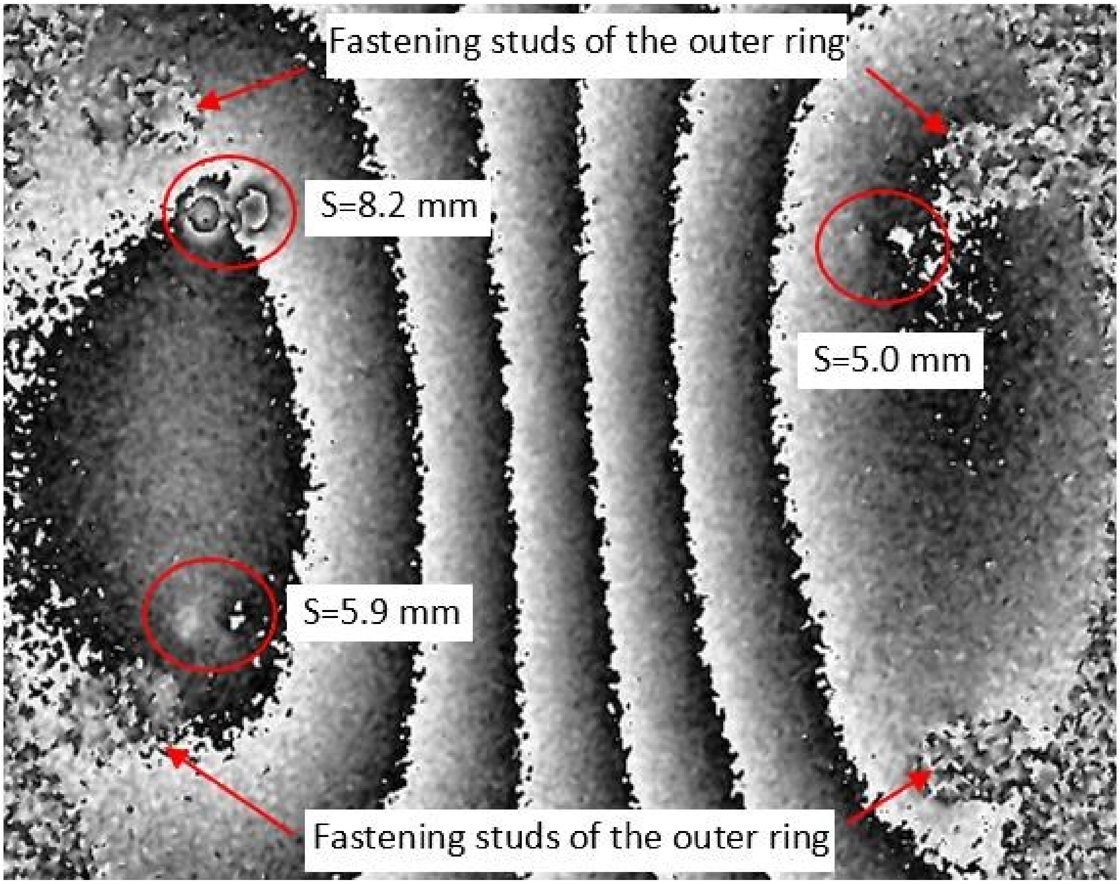

Figure. 4.14. Shearographic test results for the aluminum plate with five prefabricated defects whose thickness t = 0.5 mm, and three of which were founded at Δp = 80 kPa

Figure. 4.15. A comparison between the simulated curve of the smallest detectable defect size and the shearograms measured in the area of each defect of the aluminum plate with five prefabricated defects with their depth t = 0.5 mm

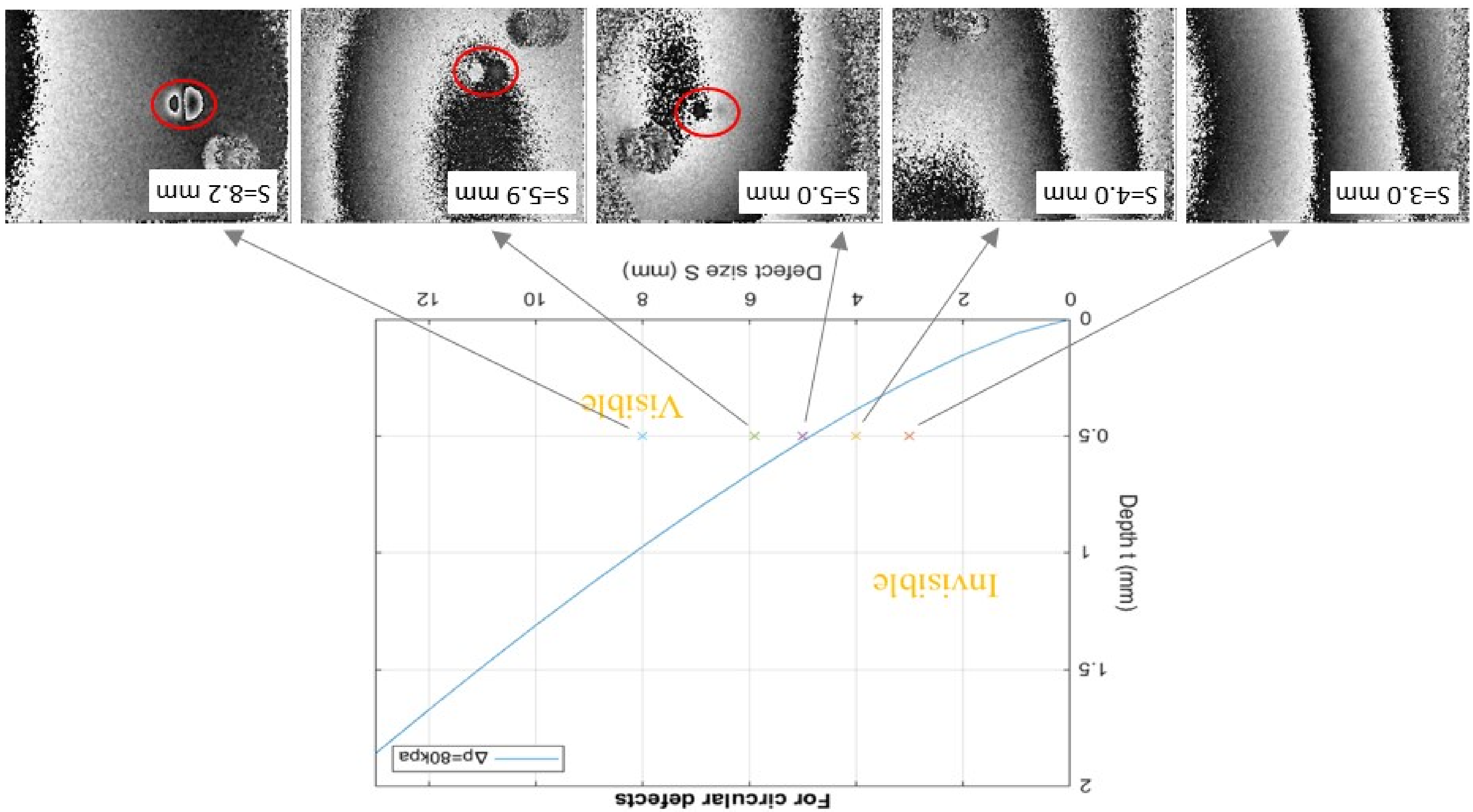

The digital shearography setup was used to test the other plate, which contained five prefabricated defects with a depth of 0.5 mm and sizes ranging from S = 3, 4, 5, 5.9, and 8.2 mm, respectively. This was done in order to further validate the numerical curve. The results of the test on the entire plate are depicted in Figure 4.15. At a pressure of 80 kPa, three of the five defects, with diameters of 5.0, 5.9, and 8.2, were discoverable. In Figure 4.15, a comparison is provided between the numerical curve and the shearograms that were obtained in the area of each defect with a depth of 0.5 millimeters. In accordance with the numerical curve, the only defects that may be identified at the specified thickness and load are those that are more than 4.9 millimeters. It is not possible to detect defects with sizes of 3 mm and 4 mm (see the two shearograms on the left), but it is possible to detect defects with sizes of 5 mm, 5.9 mm, and 8.2 mm (see the three shearograms on the right). Once again, these experimental findings demonstrate a high degree of concordance with the numerical curve at a time of 0.5 millimeters and a pressure of Δp = 80 kPa.

4.4 Analysis and Discussion

For the purpose of confirming the numerical equations and curves that were derived in section 4.3, experimental tests have been carried out. In light of the experimental results, it has been demonstrated that the simulated equations and curves are reliable. In this section, the application scopes and circumstances of these numerical equations and curves will be reviewed, as well as assess the impact that a variety of parameters have on the outcomes of the tests. The size of the smallest detectable defect, denoted by S, the corresponding depth, denoted by t, the loading magnitude, denoted by $\triangle$p, the measuring sensitivity of the deformation in the middle of the defect, denoted by

w_{max}, and the term of material properties, denoted by E and v, are the five parameters associated with each of the three models that were developed based on equations 4.13-4.18. An examination of the effects that these parameters have on the size of the smallest detectable defect S will take place in this section to be carried out. As an illustration for the analysis, the equation for the circular defects will be continue use, which is denoted by the equation 4.13-4.18. Let's rewrite equation 4.13-4.18 as an expression of the size of the smallest detectable defect S, while taking into account the thickness t, the load △p, the measurement sensitivity of the deformation in the middle of the defect w_{max}, and the term of material properties (E and v):

$$S\,(t,\,\Delta p,\,w_{max})\big|_{oval} = 4.4\frac{(3+3r^2+3r^4)Ew^{\frac{1}{4}}}{\Delta p\cdot(1-\nu^2)}\,t^{\frac{3}{4}} \tag{4.19}$$

$$S\,(t,\,\Delta p,\,w_{max})\big|_{circular} = 4.4\,[\frac{E}{(1-\nu^2)}\,]^{\frac{1}{4}}\,[\,w_{max}]^{\frac{1}{4}}\,[\,\frac{1}{\Delta\,p}\,]^{\frac{1}{4}}\,t^{\frac{3}{4}} \tag{4.20}$$

$$S\,(t,\,\Delta p,\,w_{max})\big|_{square} = 4.02\,[\frac{E}{(1-\nu^2)}\,]^{\frac{1}{4}}\,[\,w_{max}]^{\frac{1}{4}}\,[\,\frac{1}{\Delta p}\,]^{\frac{1}{4}}\,t^{\frac{3}{4}} \tag{4.21}$$

$$S \propto w_{max}{}^{\frac{1}{4}} \propto t^{\frac{3}{4}} \propto \frac{1}{\Delta p}{}^{\frac{1}{4}} \tag{4.22}$$

<u>4.4.1 Impact of the measuring sensitivity of shearography</u>

Figure 4.16 depicts two curves that illustrate the correlations between the size of the smallest detectable defects S and the depth t at various test sensitivity levels of shearography "w_{max}." The term "w_{max}" refers to the smallest quantifiable deformation in the defect center. One has a maximum wavelength of 106 nanometers, whereas the other has a maximum wavelength of 53 nanometers. When looking at the curve with a

thickness of 1 millimeter, the test sensitivity for w_{max} is increased from 106 nanometers to 53 nanometers, which means that the test sensitivity is twice. Additionally, the size of the smallest observable defect S is reduced from 9.7 millimeters to 8.1 millimeters, which is approximately a change of 16%. It is obvious that the defect size can be discovered to be less when the test sensitivity is higher; however, the impact of this is not considerable because S is only proportional to the quarter power of w_{max}.

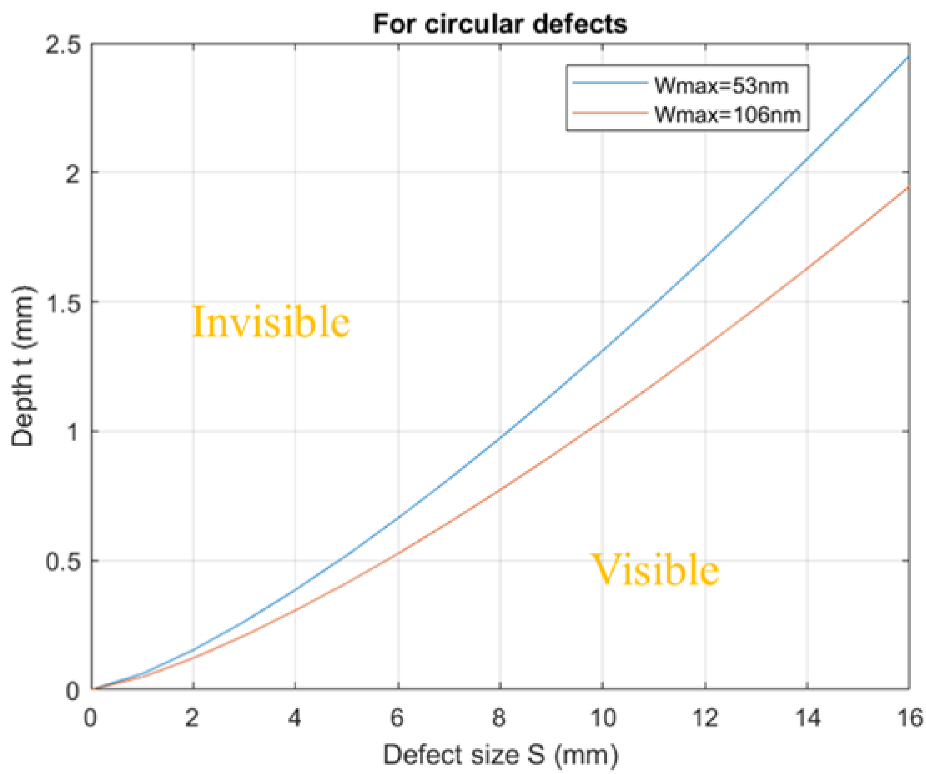

Figure. 4.16. Relationships between the size of the smallest detectable defect S and the depth t at different test sensitivity w_{max} (E = 70 Gpa, ν = 0.33 and Δp = 80 kPa)

4.4.2 Impacts of the material properties and the load magnitude

The impacts of the material property term $[E/(1-\nu^2)]$ and the load magnitude Δp on the size of the smallest detectable defect S is similar to the measuring sensitivity presented in section 5.1, because *S* is only proportional to the 1/4th power of material property's term and inversely proportional to the 1/4th power of the loading magnitude. Therefore, the degree of influence on *S* is similar to the discussion in Section 5.1, i.e. if the Young's modulus E decreases by half or the magnitude of loading Δp is doubled, the smallest detectable defect *S* will only be reduced by about 16%.

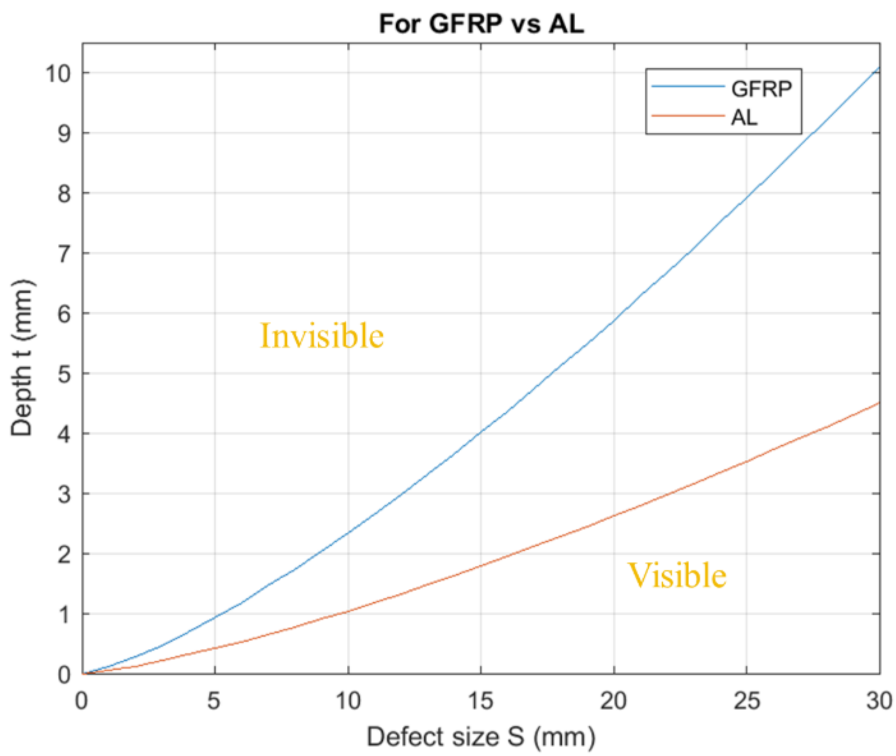

Figure. 4.17. Relationships between the size of the smallest detectable defect *S* and the depth *t* at different material properties (E = 70 Gpa, ν = 0.33 and Δp = 80 kPa)

4.4.3 Impact of the depth of defect

The impact of the defect depth on the size of the smallest detectable defect can be found from Figure 4.18. When the defect depth *t* is doubled, e.g. increases from 1 mm to 2 mm, looking at the curve of Δp = 80 kPa, the size of the smallest detectable defect S changes from 8.1 mm to 13.7 mm which is about a 69% change. This is because S is proportional to 3/4 power of t. Therefore, the depth of a defect t has a more obvious impact than the other three parameters. An increase in the depth of defects will lead to more difficulty in finding small defects.

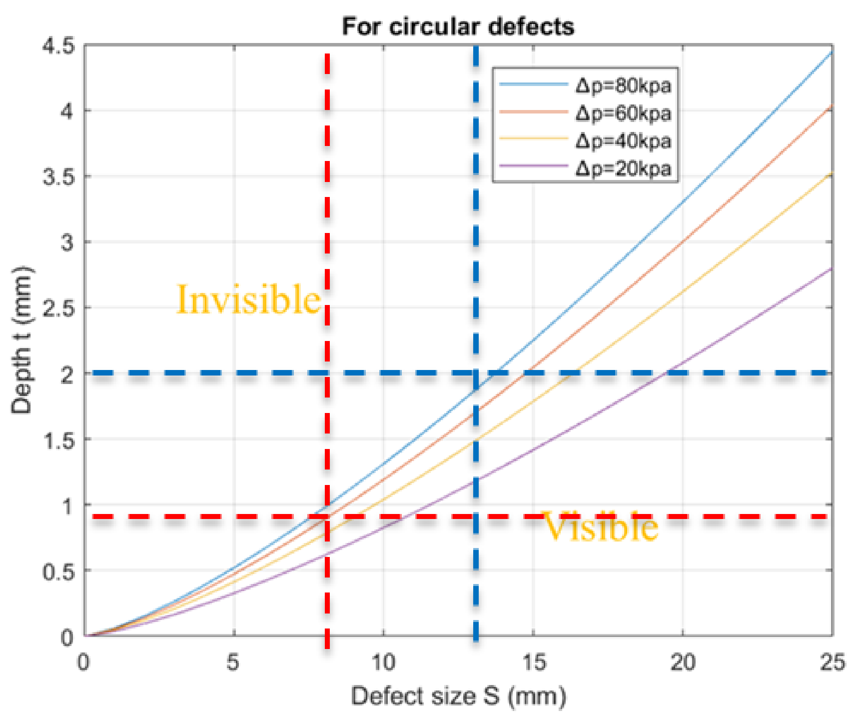

Figure. 4.18. Relationships between the size of the smallest detectable defect *S* and the depth *t* at different depth of defect (*E* = 70 Gpa, *ν* = 0.33 and *Δp* = 80 kPa)

4.4.4 Effect of defect shapes

Regarding the effect of defect shapes, the square shape is the easiest shape to find small defects, the circular shape is similar to the square shape, and the rectangular shape with its small r value, i.e. very narrow defect, is the most difficult to detect. These phenomena can be observed from Figures 4.7 – 4.9. It should be noted that the relationships between the size of the smallest detectable defect S and the depth t for an elliptical defect has not been presented due to its complexity, but because of its similarity to the rectangular equation, equations 4.13 can be approximately used to estimate ellipsoidal defects.

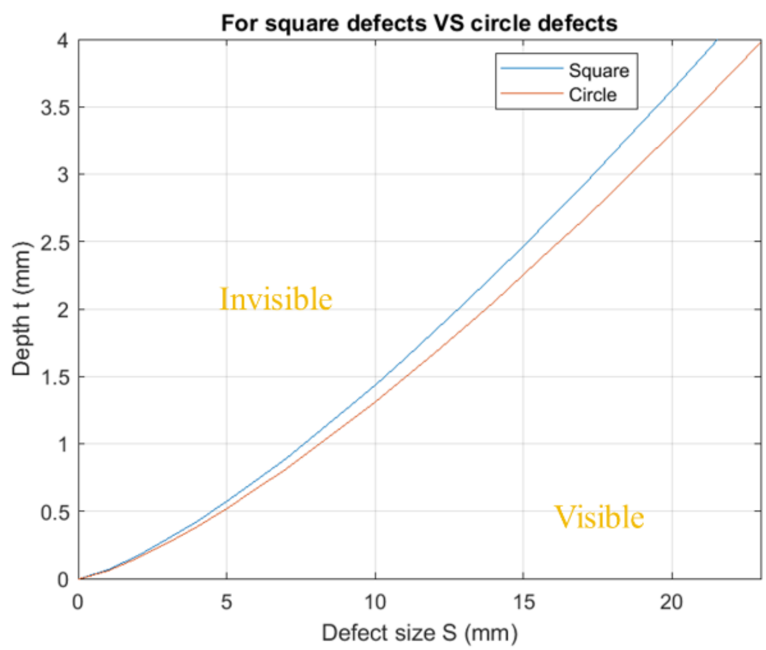

Figure. 4.19. Relationships between the size of the smallest detectable defect S and the depth t at different defect shapes (E = 70 Gpa, ν = 0.33 and Δp = 80 kPa)

4.4.5 Applicability of the simulated models

As a result of the plate theory, the differential equation of the deformation that is described in equation 4.1 and the analytical solutions that are presented in equations 4.13-4.18 are both accurate. There is a possibility that the upper portion of a defect, which is the portion that extends from the top surface to the delamination or disbond, can be considered as a plate if the thickness t is significantly smaller than the defect size S. In most cases, the thickness t is less than the defect size S. As a result, the analytical equations 4.13-4.18 are suitable for identifying defects that are located close to the surface. Consider the following example: if the defect size S is 12 millimeters, the equations and curves that have been produced are suitable for detecting defects with a depth of less than 2 millimeters. On the other hand, if the defect size S is 36 millimeters, the equation and the curve are suitable for detecting defects with a depth of less than 6 millimeters. Through the use of this connection, an estimation can be made regarding the magnitude of the defect and the depth at which it can be identified. In terms of the materials that are suitable for the models that have been constructed, the analytical equations 4.13-4.18 are suitable for any isotropic and quasi-isotropic materials, provided that the Young's modulus and Poisson ratio may be considered independent of the directions. The following are examples of composite materials that are suitable for direct application of analytical solutions:

- Sheet Molding Compound (SMC) Carbon Fiber substrates, which are characterized by short fibers that are located in a random orientation.
- Composites with short fiber reinforcements, which may make use of carbon or glass fiber reinforcements and may also contain a thermoplastic matrix.

• Sandwich structures that have an isotropic front sheet and typically have a core that is honeycomb-like in character.

When working with woven fibers that are arranged in regular patterns, it is possible that some adjustments will be required. The deformation that is estimated using the classical theories is sufficient for quasi-isotropic composite substrates (such as -60°/0°/60° or 0/-45°/45°/90°) for the purpose of shearographically detecting delamination defects through the use of shearography. On the other hand, a correction factor that takes into consideration the shear stress that exists between the plies might be utilized in order to achieve more precise results [106]. The Young's modulus and the Poisson ratio can be assumed to be independent of the x and y coordinates when one considers these particular circumstances.

Due to the absence of considerable structural stiffness in the direction that is perpendicular to the fibers, this model is not easily applicable to unidirectional fiber composites when it is applied to these materials. Additionally, this methodology is not suited for detecting defects that are very deep without increasing the size of the defect themselves. It has been claimed that hybrid approaches, such as shearography paired with the FEM method, have been utilized in this particular instance [47-48]. There are certain circumstances and circumstances in which they are efficient; however, shearography is not the ideal way to test very deep defects unless the size of the defect is considerable. The reason for this is because if the surface deformation generated by a load is unable to reach the measuring sensitivity of shearography, then no surface information can be used for finite element modeling (FEM) or other numerical methods. This phenomenon is highly probable if the defects are placed too deep from the surface. Application of techniques such as ultrasonic and x-ray techniques is recommended for the purpose of detecting both deep and tiny defects.

4.4.6 Boundary conditions and the loading methods

Regarding the determination of "visible" and "invisible" defects in the S-t curve, if a defect point falls directly on the curve, then theoretically, this defect size at the corresponding thickness is traceable under the given load magnitude. This is the case even if the defect point is not visible. It will not be possible to identify any point in the region that is smaller than this size but larger than the thickness; in other words, points that are located above the curve. On the other hand, for practical purposes, the boundary conditions of genuine defects are not exactly the same as those of the models. A more stringent boundary condition is shown by the fact that the boundary condition in the models that were developed has been fastened all around. If it is possible to discover a defect under this condition, then it is highly likely that it will also be discovered under other boundary circumstances. Therefore, the visible defect (i.e. the area above and below the curve) is fairly accurate. However, depending on the actual boundary condition of the defects, there may be points in the invisible region that are visible slightly above the curve. This indicates that there is a transition area that exists slightly above the curve, but it is difficult to indicate exactly in the figure due to the fact that the boundary condition of the defects is unknown. It is recommended that numerical models and curves be used to estimate the smallest detectable size and depth rather than using them for exact measurement of the smallest detectable defect size. This is because numerical models and curves are more accurate than exact determinations.

In conclusion, it is important to point out that the models that were constructed relate to either a pressure loading or a vacuum loading. The vacuum loading method is the most effective loading method for a shearographic test because it generates a pulling force, as demonstrated in Figure 4.1b. Delamination or disbonding can be separated by a pulling force, which can also generate a larger deformation and make it easier to do non-destructive testing on the defects. It is true that the vacuum loading method is the most effective loading method; nevertheless, it is also the most difficult loading method. One of the most straightforward approaches to loading is through heating; unfortunately, the models that are described in this study are not suitable for heating loading. The development of this work is something that will hopefully take place in the not-too-distant future.

4.5 Conclusion

A numerical and experimental study of digital shearography for determining the size of the smallest detectable defect and the relationship with different parameters has been conducted. Numerical models to detect defects close to surface (usually, the defect depth t is smaller than 1/5 to 1/8 size of defect) and to determine the size of the smallest detectable defect by shearography under a vacuum and a pressure loading have been developed which provides first hand materials for test engineers before starting their investigations. The numerical models developed show that higher sensitivity for deformation measurement by shearography, less rigid material, larger loading magnitude, and shallower defects can lead to finding smaller defects. Of these four parameters, the most significant impact on defect inspection is the depth of the defect. An increase in the depth of the defect will obviously lead to more difficulty in finding the defect. The other three parameters: sensitivity for measuring deformation, material properties, and load magnitude, have the same weight for defect inspection and less impact than the defect depth t. This is because the size of the smallest detectable defect S is proportional to one-quarter's power of each of the three parameters, but three-quarters the power of the defect depth t. The experimental validation of shearography demonstrated a very good agreement with the numerical models developed, which shows that the numerical models are a promising method to provide useful estimation for NDT by digital shearography. The models established in equations 4.13-4.18 can be used to assist in the shearography inspection by estimating the size and depth of the smallest detectable defect with the corresponding load magnitudes.

CHAPTER FIVE

INCREASE SMALLEST DETECTABLE VISUALIZATION DEFECT: CONVENTIONAL METHODS AND SEGMENTED FITTING METHOD TO ELIMINATE GLOBAL DEFORMATION

The utilization of a wide variety of novel materials necessitates the implementation of increasingly demanding quality evaluation requirements as a result of the progression of science and technology. The digital shearography system is a high-precision interferometric non-destructive testing (NDT) device that has proven to be an effective instrument for the inspection and assessment of materials. In particular, it has been found to be useful for detecting delamination and debonding in honeycomb structures and composites. When it comes to the use of digital shearography, one of the most frequently encountered challenges is figuring out how to differentiate between defect information and general deformation information. Incorporating several restrictions, such as the requirement for enormous data sets and the necessity for fine-tuning, it has been the focus of a great deal of effort to implement intelligent algorithms. In addition, classification tasks for the purpose of defect classification are frequently employed to investigate factors like impact energy, which can result in an incorrect interpretation of the results. Methods for defect detection frequently need the participation of competent practitioners, and it is possible that other engineering specialists are not readily available. Before moving on to the next section, the numerous methods that are utilized to acquire defective information that is more precise will be firstly examined. Additionally, the various loading and deformation states will be discussed and analyzed. The segmented fitting method is the a novel technology that is offered, and it is used in conjunction with the fringe pattern. The first derivative of sample deformation can be calculated using a technique called digital shearography, which involves measuring phase differences during the process. Decomposing phase difference into a collection of global deformation, defect, and noise information is possible under most working circumstances. This hybrid approach takes into account theory that has been established through experimentation and makes use of image processing techniques in order to get rid of information about global deformation. The fringe pattern after loaded is subjected to processing in order to operate according to the concept of this method. First, the value of relative phase change of each fringe is extracted, and then a second-order polynomial fitting is done on each fringe in order to create a fitting plane. Finally, in order to get rid of the global deformation, the plane is subtracted from the fringe pattern that was captured following the deformation. Finally, in order to validate these correlations, experimental verification was carried out using manufactured defects of varying sizes. Furthermore, the results of the experiments demonstrate that this strategy is advantageous in terms of amplifying and improving the capture of information linked to defects. The purpose of this research is to enhance the efficiency and precision of digital shearography in the detection of defects in a variety of materials, including delamination, debonding, and similar issues. The results of the experiments demonstrate that this method contributes to the enhancement of the non-destructive testing capabilities of digital shearography. Additionally, it makes the extraction of defect information more straightforward and more intuitive.

5.1 Introduction

Speckle interferometry techniques, such as digital holography and digital shearography, are currently being utilized extensively for full-field slope and displacement measurements. These techniques are also capable of measuring surface deformations on a micron scale. After nearly four decades of research, it has finally reached the point where it is a non-destructive testing technology that is approved by the industry [107]. Through the use of an interferometry technique known as digital shearography, internal defects can be identified. This is accomplished by measuring the out-of-plane displacement gradient of a specimen surface that is illuminated by a coherent beam. The utilization of the phase shift approach results in a significant enhancement in the accuracy of the displacement gradients that are measured [108,109]. This further encourages the development of measurement equipment and the application of those instruments in the non-destructive testing of a variety of composite materials [107 110–111]. The findings of the tests are associated with several loading methods, including heat radiation, pressure, vacuum, acoustics, and mechanical vibration stimulation, among others. The capacity to detect deeply buried defects is limited in thermography with thermal stimulation due to issues with rapid heat dissipation and uneven heating [112, 113].

However, due to the fact that composites are often anisotropic materials, it is difficult to simulate the behavior of the specimen when damage occurs, such as damage that is caused by impact [30,114]. When testing composites and alloy materials, defects such as debonding and delamination frequently arise during the production process or during usage due to variances in the chemical and physical properties of various materials

[107,110] because of the fact that different materials will have different properties. On the other hand, because of the complex properties of the material, it is possible for a number of defects, such as delamination and fiber breakage, to develop during the production process as well as during use. During the manufacturing process, for instance, residual stresses caused by resin shrinkage and uneven curing can result in delamination, fiber matrix debonding, fiber waviness, and matrix cracking in thick composites. These issues can be caused by the production of thick composites. Accidental cracks that occur during usage can also produce matrix cracking and internal delamination, both of which are scarcely apparent from the impact surface because of their depth. The mechanical properties and structural complexity of composites may be significantly impacted by these imperfections, which may appear on the surface or near the surface, or they may be deeply buried. Based on this reason, non-destructive testing (NDT) of composite materials or alloys is of utmost importance in order to enhance the safety and dependability of structures. Therefore, it is necessary to detect the defects at an early stage in order to preserve structural integrity. By utilizing digital shearography, one may assess the structural integrity of a composite structure following an impact, thereby determining whether or not the structure has to be repaired or replaced [115–119].

However, due to limitations of experimental equipment, experimental environment, and application scenarios, the information that the shearogram recorded by digital shearography can record is limited. How to extract more detailed information from the recorded images is a question to be discussed in the next section. The most common method is to increase the contrast between defect information and background information. First, it is necessary to understand the development of previous research on improving the sensitivity of digital shearography by improving contrast and use it as a basis, and then develop a new system based on previous research. As a result, this part begins by analyzing a variety of approaches and discussing the benefits and drawbacks associated with each of pervious research. Following that, a novel approach that was based on fringe pattern was suggested as a solution to these issues. The fringe pattern is created by multiplying the undeformed speckle pattern with the deformed speckle pattern. This results in the fringe pattern being divided into three parts: the fringe pattern, which contains phase information, the background intensity, and additional high-frequency noise components. By substituting a new plane and subtracting, the final two components can be removed from the equation. Furthermore, this approach is more resistant to oscillations in the speckle field than other methods.

5.2 Polynomial fitting and other method to remove global deformation

In this part, the primary focus is on the examination of conventional technologies. Previous studies have shown that techniques that can improve the sensitivity of digital shearography in specific boundary cases mostly convey defect information by amplifying it by increasing the contrast between the defect information and the background information. There are two basic methods that might be utilized regarding the extraction of information regarding defects. One method involves reducing the amount of noise in order to improve the understanding and efficiency of the information that is being expressed. The elimination of the global deformation is still another strategy that can be taken in order to further improve the visibility of defect information. The study that is now being done on noise reduction makes use of spatial deformation to carry out second, third, and fourth-order differentiation in order to mitigate noise and enhance defect diagnostics.

In the beginning, the topic of lowering the amount of noise and improving the high-frequency signals in areas where defects are prevalent will be discussed. Lopes et al. [37] utilized numerical differentiation inside the phase diagram for the purpose of reducing noise with stroboscopic illumination or intensity modulation.

By employing this technique, the second, third, and fourth order spatial derivatives of the displacement field are computed in a sequential manner. This is accomplished by applying a low-pass filter and a first-order central finite difference algorithm to the phase map of the modal rotation. As a result of the fact that these phase diagrams and their associated derivatives are specified between $-\pi$ and π, the discontinuities can be removed by employing an expansion procedure. After that, a continuous description of the rotating field can be obtained by the procedure of unwrapping method, which results in a better visualization of the perturbations in the derivatives, which in turn leads to a better analysis of the damage localization. The elimination of high-frequency noise is accomplished through the utilization of an averaging filtering technique in this method. However, in order to make use of this method, the fringe pattern must first be transformed into a continuous mapping. This is accomplished by shifting them to complex domains, and the filtering technique that is employed makes use of diagram convolution. After all is said and done, the derivatives of the modal fields can be generated by employing Goldstein's unpacking procedure [122]. From the result, the low-frequency information will gradually decrease, while the high-frequency information will become more obvious and clearer. This demonstrates that the utilization of stroboscopic laser illumination and temporal phase modulation in shearogram results in significant improvements in the quality of measurements. According to this conclusion, the information regarding defects will be more understandable because it is much simpler for operators to locate information about defects.

Based on that, a frequent method involves the construction of a fitting plane, followed by the elimination of the global deformation through the subtraction of this fitting plane. According to the fundamental idea behind this technique, the fringe pattern is composed of two distinct pieces of information. These include information about global deformation and abnormal defect deformation, which is brought about by defects in the global deformation information. The phase value of the global deformation information is the most significant one in all information of the shearogram. When compared to the information regarding the global deformation, the width of the defect is limited. This makes it easy for the global deformation information to mask the small defect information, making it more difficult to identify. The second way, which is also the most popular method, is to construct a fitting plane by using a variety of methods, and then to utilize this fitting plane to represent the global deformation. After that, the fitting plane is removed from the initial image in order to get rid of the global deformation. This helps to enhance the defect information, which in turn makes it simpler for the operator to locate it. Because of this, it is possible to readily collect information regarding defects by removing the global deformation which shown in Figure 5.1. [38-45].

First, the method of polynomial regression fitting methods will be discussed. In order to demonstrate the importance of researching new approaches, the first thing that needs to be done is to provide a concise summary of how this method eliminates global deformation information. By employing a polynomial regression function, Templeton [48] was able to design a suitable plane. In order to reduce the effect of global deformation information, this technique involves subtracting the plane that fits the polynomial regression curve from the plane that represents the deformation. This is accomplished by conducting a polynomial fit on the diagram that has been distorted using a regression curve. Getting rid of general deformation is accomplished with this procedure the majority of the time. Within the initial step of this procedure, shearography is used to record the fringe pattern while the loads are large. After that, an unwrapping algorithm is used to unfold the fringe pattern in order to achieve the construction of a continuous deformation phase map. Following this, the polynomial regression fitting approach is utilized in order to produce a simulation phase diagram that is based on the deformation diagram. After that, the simulation map is subtracted from the deformation map in order to eventually get rid of the general deformation and only keep the defect information. A step-by-step analysis of the flow diagram is presented in Figures 5.2 to 5.4. For example, the perfricated defects aluminum disc was employed to show the schematic of polynomial regression fitting method. Figure 5.2 (a) records the fringe pattern, and 5.2 (b) records the image after unwrapping. The results of recording the fringe pattern under large load by shearography are displayed in Figure 5.2. The image is recorded after the shearography process has been completed. Due to the fact that the global deformation is significantly larger than the defect information and noise, the defect information and noise will be disregarded when polynomial fitting is being performed. Figure 5.3 describes the entire plane is processed using the fitting results and Figure 5.4

illustrates the workings of the principle of this method. After that, a polynomial regression function is utilized in order to come up with a suitable plane that is representative of the total deformation. Following the unwrapping of the fringe pattern that was captured by shearography under large loads, the fitting plane is then subtracted from the deformation data in order to effectively minimize the global deformation. Figure 5.4 illustrates the outcomes that were obtained by selecting regression equations with varying fitting orders. These equations were selected using polynomial regression function orders that varied.

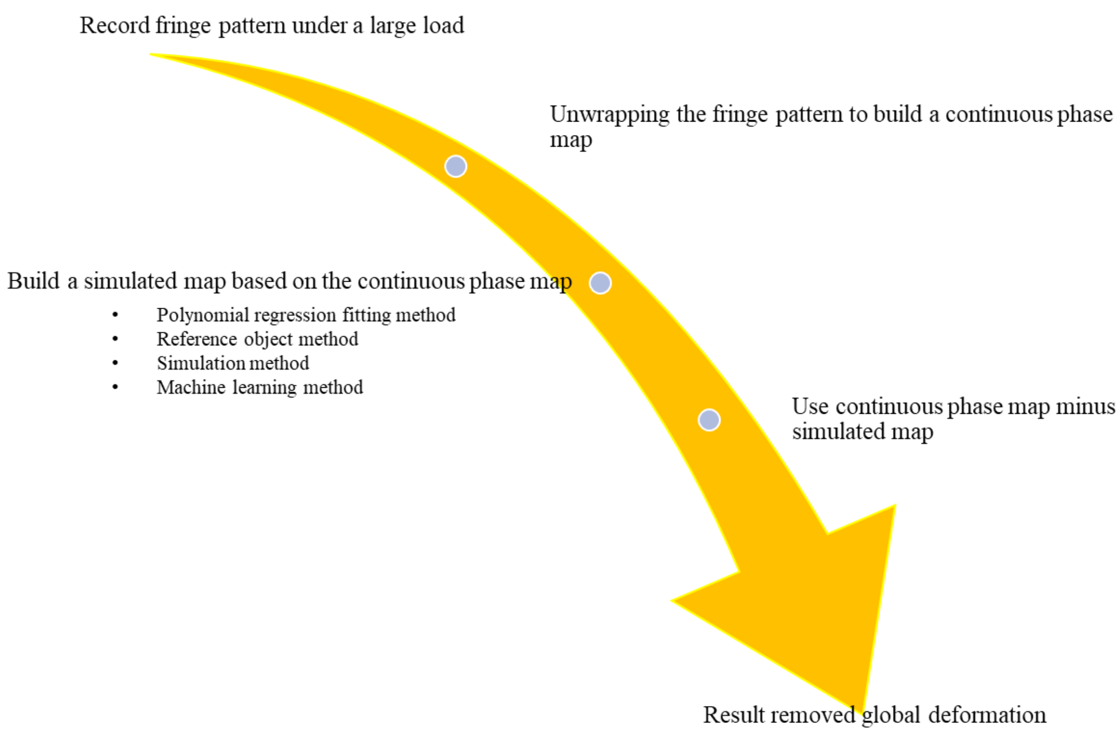

Figure 5.1 Schematic of polynomial regression fitting method.

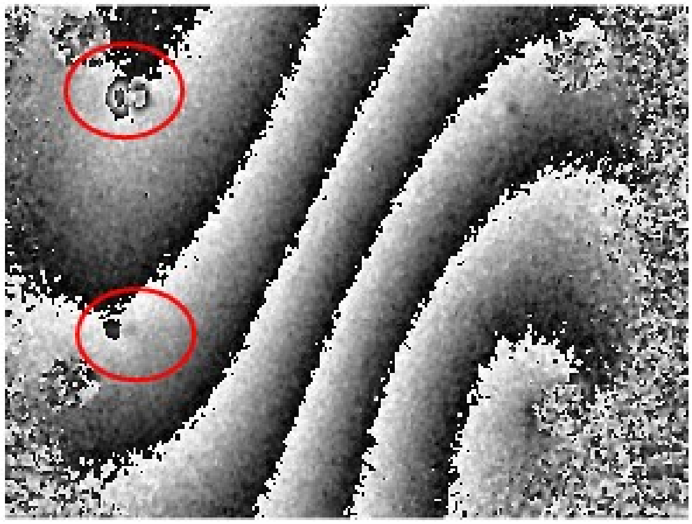

(a)

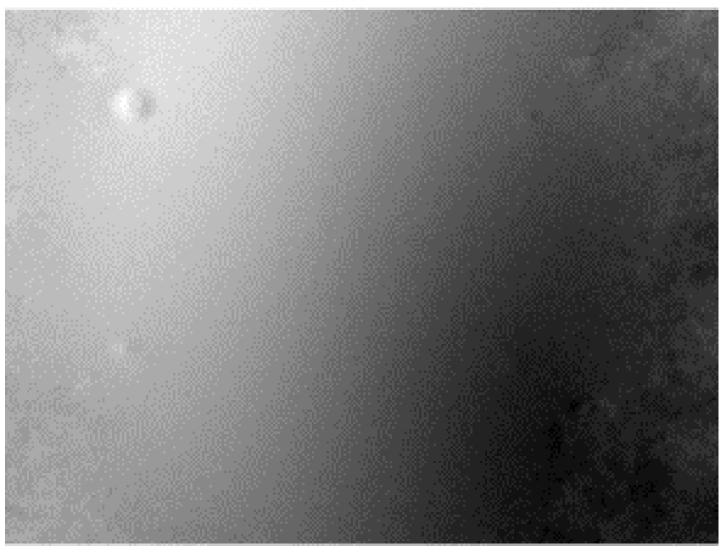

(b)

Figure 5.2 AL05 deformed image (a) Deformed image (b) unwarping image

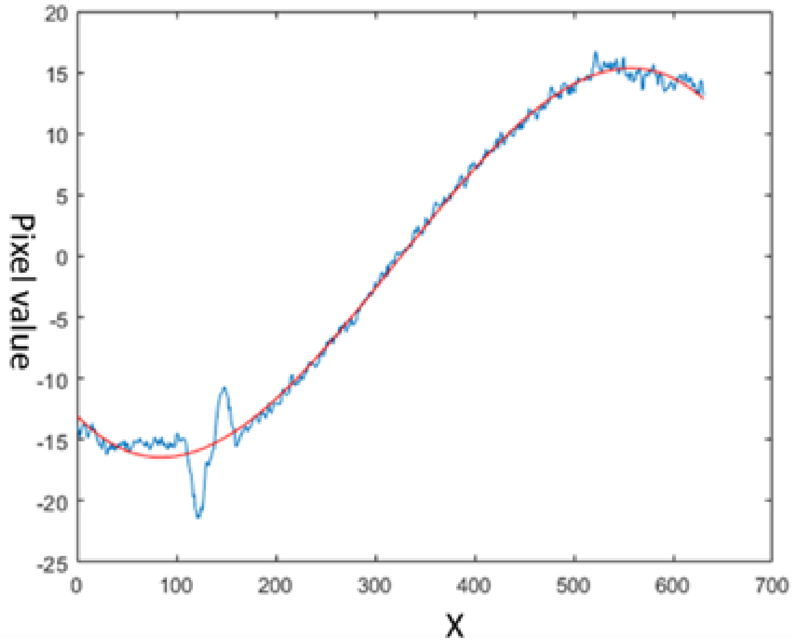

Figure 5.3 Theory of Polynomial fitting method

(a) (b)

Figure. 5.4. Polynomial fitting plane(a) Fitting plane (b) Deformed image minus fitting plane

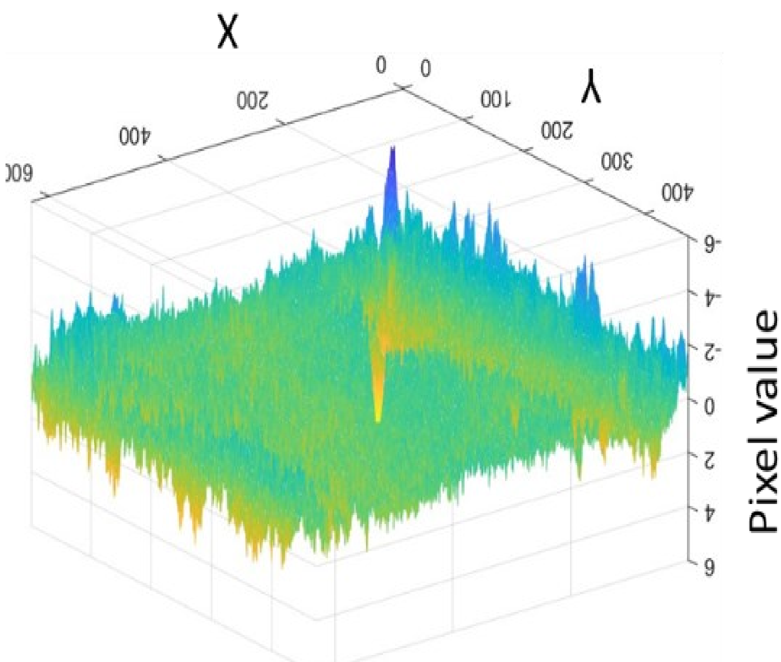

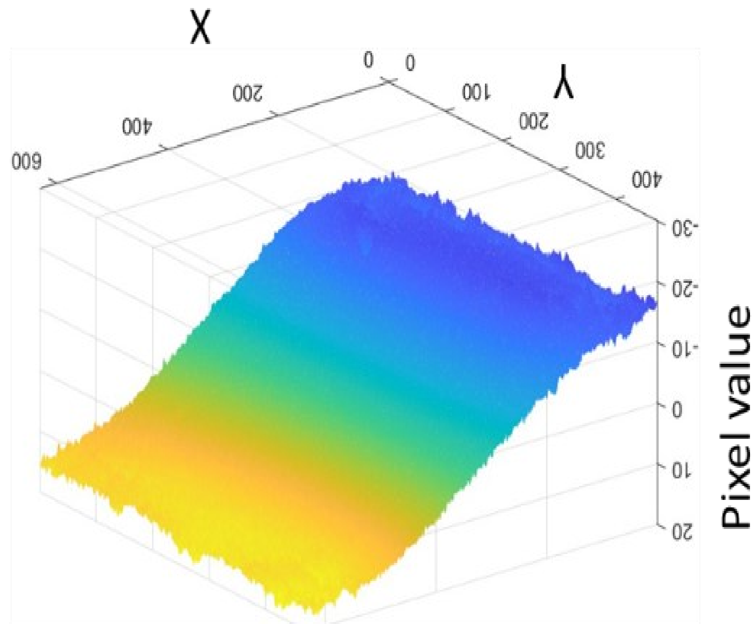

(a) (b)

Figure. 5.5. Final result of fitting method(a) 3rd order (b) 8th order

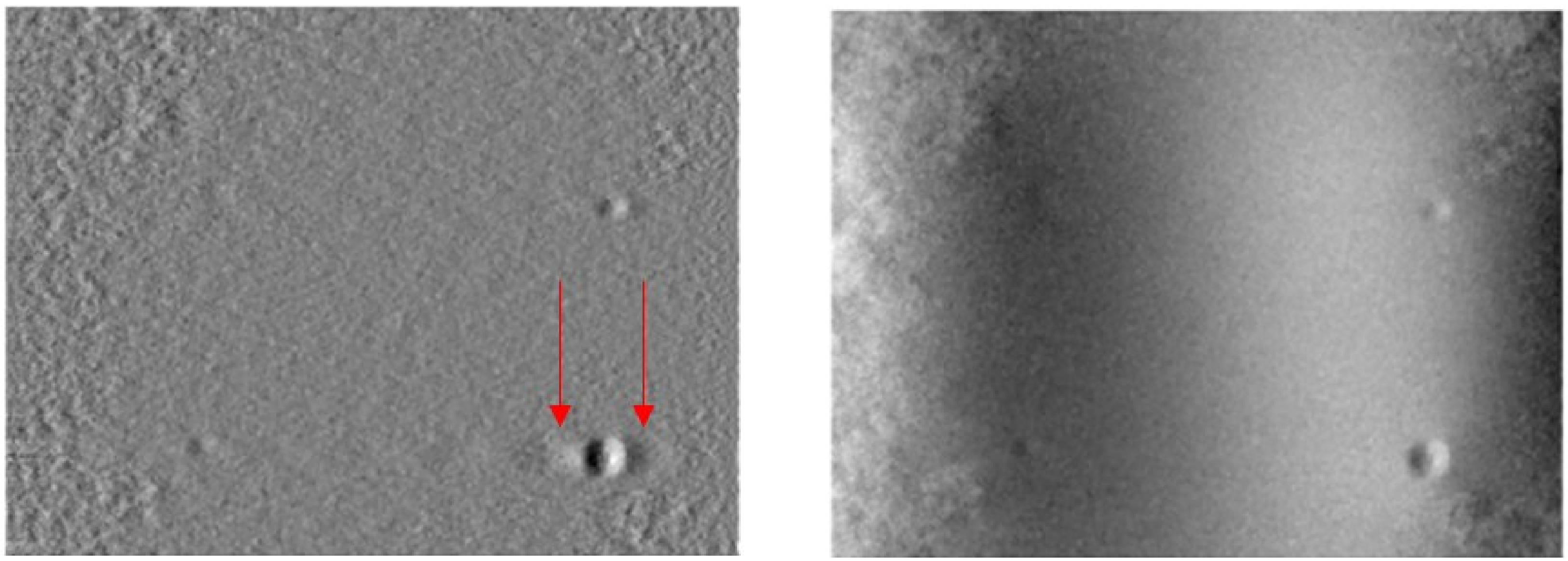

In the following section, several ways for removing global deformation will be briefly examined. At first, the B-spline interpolation technique is the subject of discussion. For the purpose of constructing the fitting plane, Deepan makes use of the B-spline interpolation approach [123]. For the purpose of determining the slope, curvature, and deformation of individual fringe patterns in digital shearography, the technology creates an algorithm for fringe analysis. Estimating the bias curvature and deformation map from the fringe direction and fringe density maps is accomplished through the utilization of a particular method. The curvature and deformation maps that were obtained are then subjected to additional processing by means of B-spline interpolation in order to accomplish the building of the fitted plane with a high-quality curvature and deformation map. However, there are several limitations associated with this technology. After B-spline interpolation, the map is not clear, and there is noise in the central part of the map. This noise leads to the introduction of information that is not necessary, and it is also time-consuming.

The following technique is known as the reference plate method, and it involves establishing a reference plane in order to model the aggregate deformation. [45] Fomitchov carried out an experiment in which the research simulated global deformation by inserting a replacement plate into the apparatus. This plate was intended to replace the plate that had been first identified as defective. A comparison is made between the intensity value at a pixel position in the interferogram and the intensity value at the same pixel in a reference interferogram using this method. If the relative deviation in intensity of a pixel is greater than a threshold that falls between 0.1 and 0.5, then the pixel is considered to be within the borders of an edge cluster. If this is not the case, it will be located in the background portion of the sample that it is necessary to reference. In spite of the fact that this technique does not call for any new apparatus, it does make use of new specimens as the reference specimen. This method is not practical because the experimental loading process cannot be repeated at the same time, and different materials also have their own unique characteristics.

Tao used polynomial fitting as a method to perform similar phase correction. The objective of this process was to optimize the image of the specimen by eliminating errors and mitigating defects for the purpose of improvement [46]. Use a good sample with the same magnitude of thermal loading, then use the fitting method for the good sample, and finally use the deformed fringe pattern to subtract the good pattern in order to obtain the defect information. Initially, the polynomial fitting method is applied; however, due to the limitations of the polynomial fitting method, it does not perform as well as it should. In order to extract the defect deformation of the structural health monitoring system, this approach requires the use of a reference damage panel, which is one of the disadvantages of this approach. In the course of this process, there is a possibility that more errors will occur, which may result in the error of information regarding defects. Additionally, the act of concurrently capturing two images leads in a reduction in the resolution of the camera.

Optimization of the contrast-to-noise ratio method was carried out by Hofmann and his colleagues [47] in order to quantitatively evaluate the contrast between defects and the backdrop of the image. However, this method requires a significant amount of empirical data, requires extended periods of mechanical training, and is only effective for a single category of material. In addition, it is an inefficient method. An additional method entails contrasting the knowledge about defects with the information about planes, which is then followed by the application of machine learning techniques that are founded on this overarching theoretical framework. The collecting of information regarding defects can be accomplished with better precision for those technique who have received considerable training. However, this method requires a significant amount of empirical data, requires extended periods of mechanical training, and is only effective for a single category of material. In addition, it is an inefficient method.

However, there is a possibility that vital information in the fringe pattern will be overlooked because all of the methods rely on unwrapped displacement data. The fitting method is appropriate for removing global deformation in situations when the deformation is under the elastic and can be predicted. However, in order to reduce the global deformation, a technique is required in situations when the loading conditions are complex. The purpose of this research is to present a method that eliminates global deformation and extracts defect information based on the analysis of fringe patterns which is possible to fit on the fringe pattern using this procedure. The theory behind it is comparable to that of fitting the equation for polynomial regression analyses. In order to achieve first-order fitting, it takes into account the phase value change that occurs between each pair of fringes on the fringe pattern. After the fitting process, the fringe pattern that is left over is a representation of the global deformation's fringe pattern. This technique is straightforward and easy to comprehend, and it enhances the quality of the photograph.

5.3 Segmented fitting method

As part of digital shearography, surface positions both before and after deformation can be compared in a number of different combinations. The subtractive speckle-related fringe creation approach is the method that has been used conventionally and is the most prevalent. In addition to having a limited dynamic range, measurement sensitivity, and effective spatial resolution, these fringes have a signal-to-noise ratio that is relatively low and noticeable contrast. The advancement of unwrapping techniques has become increasingly popular among users of DSPSI technology as a result of their pursuit of the measuring qualities stated above. As discussed in previous parts, the unwrapping computations were the foundation of all of the earlier techniques that were successful in removing global deformation. There is a good reason for the widespread adoption of the unwrap method: it compensates for or removes the majority of the drawbacks associated with fringed patterns. However, the technology brings with it an additional choice that is not typically properly evaluated once it has been implemented. Rather than producing a fringe pattern, phase shiftting results in the production of a "wrapped" phase profile. In many cases, it is possible to unwrap a wrapped phase profile in order to provide a continuous collection of data. This requires a certain level of expertise, attention, and time. The unfolded phase that is produced as a result is a direct representation of the surface deformation that occurs at each pixel. On the other hand, this method is not particularly helpful in finding defects, and it results in phase discontinuities when attempting to reconstruct a smooth phase map. Struggling to overcome the challenges that are associated with locating discontinuities and calculating different values of 2π is a challenging endeavor. It is crucial to retain as much information as possible throughout the fringe pattern processing because even though this process may result in some loss of information, it is crucial to retain as much information as possible. Secondly, the sequence in which the various fitting equations are selected has repercussions for materials that have defects of varying magnitudes of load. In order to select the sequence of fitting equations and to decide the type of fitting equations that are utilized in the fitting process, several criteria are required. This is due to the fact that the shape, position, and depth of defects that occur in real life are distinctively different from one another. It is on the basis of this that the idea of segmented fitting is first introduced.

The segmented fitting principal diagram may be found in Figure 5.6. The use of the segmented fitting principle can be broken down into the four stages that are listed below. Digital shearography technology is utilized in the initial stage of the process in order to record the fringe pattern that occurs after the specimen has been deformed under a specific load. In the next step, the border is chosen to be either white or black, depending on the phase value. This means that the pixel value is either 0 or 255, which is used to establish the range of each segment. It is recommended that it begin at the edge and choose pixel values that are continuous and unchanging in order to prevent the presence of defects. When it comes to fitting the pixel value changes that occur within each segment, the third part makes use of a first-order fitting equation. On the other hand, the fitting approach creates a simulation map that was derived from the deformation map in order to accurately depict the global deformation. After that, the simulated image is subtracted from the original global in order to get rid of the global deformation, the Figure 5.7 shows another way in which the principle can be stated.

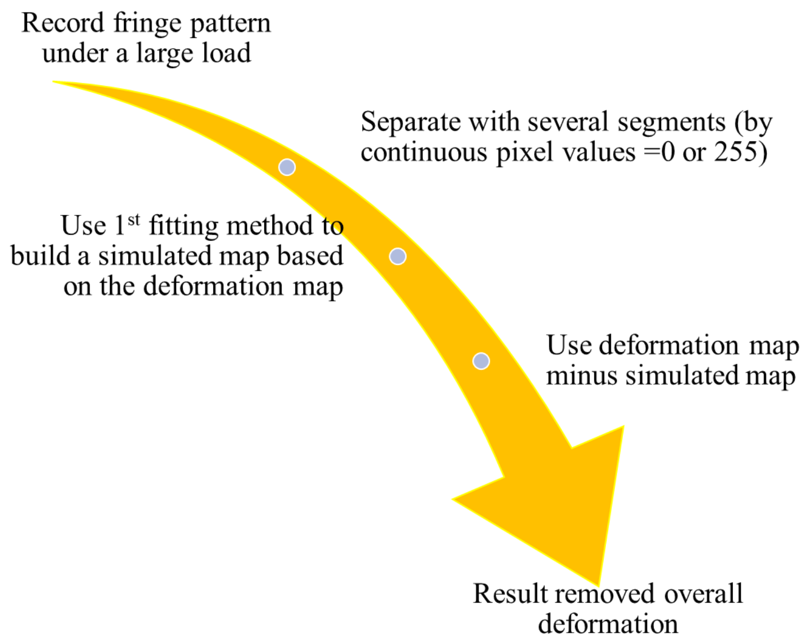

Figure 5.6 Schematic of Segmented method.

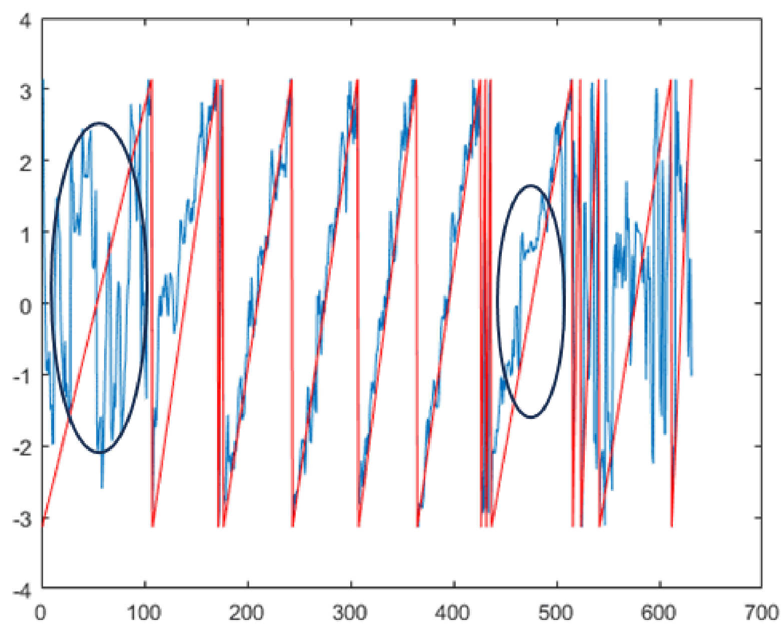

Figure 5.7 Theory of Segmented method

5.4 Experiments & results

5.4.1 Experimental setup and sample preparation

The apparatus that was utilized in this investigation is illustrated in Figure 5.8. The two most common types of loading procedures that are utilized in shearography are thermal loading and vacuum loading. When it comes to the identification and characterization of defects that have open boundaries, the employment of vacuum loading techniques can be prohibitively expensive and may not be the most effective method. The application of thermal loading has the potential to extend the duration of the test, bring about extensive changes to the specimen, and bring about temperature differences throughout the surface of the object. For the purpose of determining whether or not the procedure described in this article is effective, a number of different loading techniques and materials with a comprehensive range of attributes were utilized. The specimen is subjected to continuous irradiation from a 1000W halogen lamp for a duration of three minutes as part of the thermal loading procedure, which is one of the methods that is utilized. When measuring the surface temperature of the test specimen, the infrared thermometer is utilized, and it has the capability of attaining a maximum temperature of 44 degrees Celsius. On the other hand, the vacuum loading method, makes use of a vacuum pump to produce a maximum pressure differential of ninety kilopascals (kPa) within the vacuum chamber. With a power output of fifty milliwatts and a wavelength of six hundred thirty-two nanometers, an extended helium-neon laser was used to illuminate the front surface of the specimen while the experiment was being carried out. Additionally, phase-shift technology was utilized in conjunction with digital shearography in order to conduct the examination of the specimen. The shearing device is a modified Michelson interferometer that adds a piezoelectric transducer (PZT) powered mirror to aid the phase-shifting approach. The camera has a certain amount of megapixels, and the shearing device is one of the mirrors of Michelson interferometer. For the purpose of demonstrating the comprehensive applicability and precision of the coefficient approach, a wide range of materials were selected as test subjects in order to suit a variety of different circumstances. A prefabricated aluminum panel (AL05) with a diameter of 166 millimeters and five round defects is the first material that will be discussed now. It is 166 millimeters in diameter and has a thickness of 12.7 millimeters. 0.5 millimeters is the distance between the surface and the circular defect, which is shown in Figure 5.9.

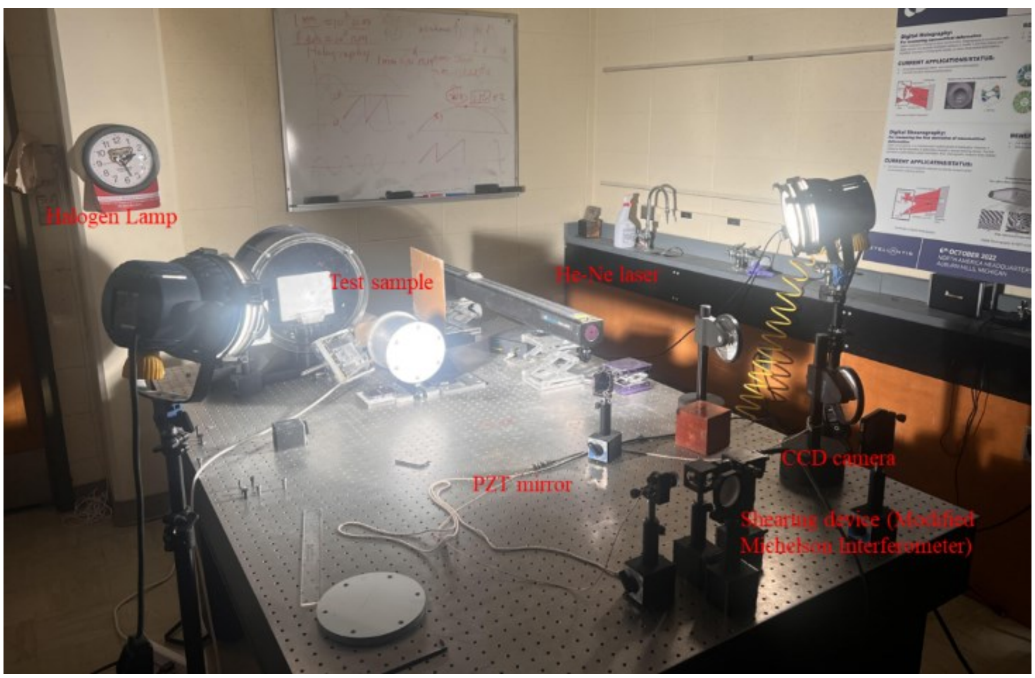

Figure 5.8. The setup of digital shearography for the experimental validation

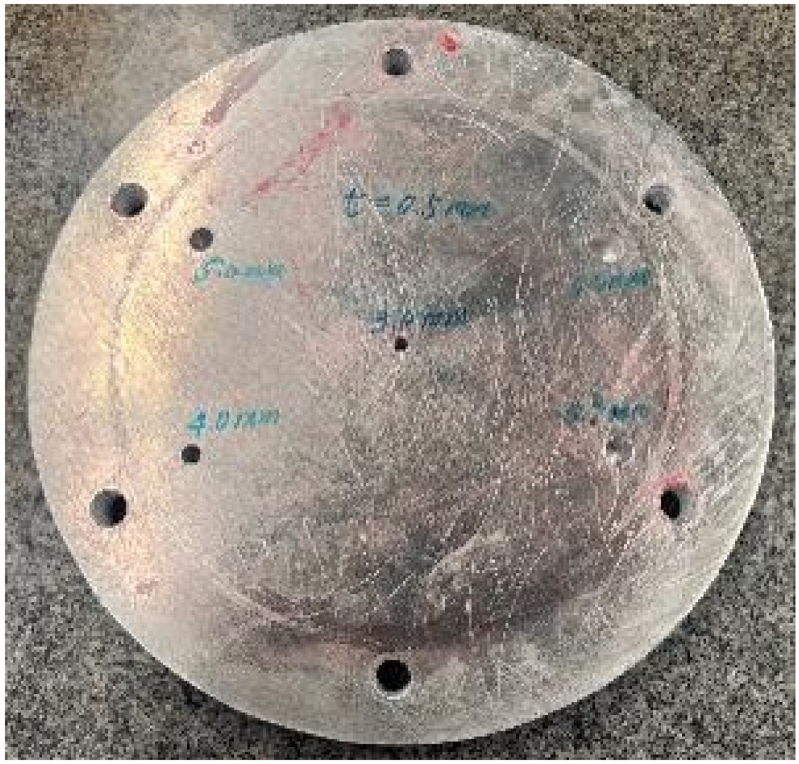

Figure 5.9 Sample of AL 05

Also, for confirming the theory, a composite material (C3) with prefabricated three defects which set in horizontal are selected to verify the result. C3 is a composite material that is constructed of two aluminum slabs that are bonded together with three different-sized internal defects. Figure 5.10 shows the sample of C3.

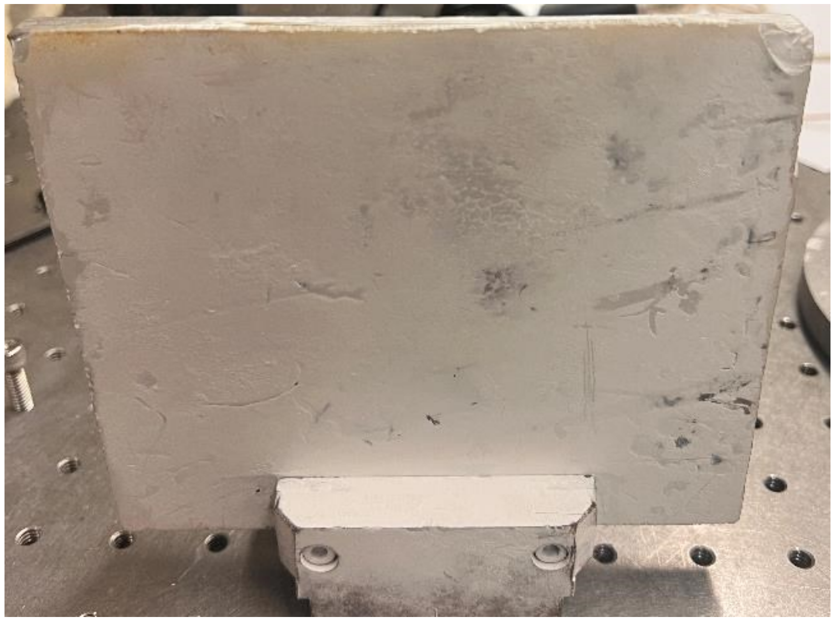

Figure 5.10 The sample of C3

In addition, the fitting method is not appropriate for situations involving complicated deformation, as will be shown in further depth in the subsequent sections. It is impossible to measure the actual global deformation of the surface when using the fitting strategy since it is difficult to select a suitable fitting equation for surfaces that are intricate. Composite laminate (CP) was chosen as the representative material with the factors, which shows in Figure 5.11. The total thickness of the material is 5. 65mm. To imitate imperfections, drill holes on the specimen with the different sizes. The specimen dimension is 150 mm x 145 mm. The nine cylindrical holes with the following dimensions: 6 mm, 10 mm, and 20 mm in diameter, and a depth of 5.15 mm. Additionally, create a 3 mm-deep stage to mimic delimitation. The thinner steps are 2.65 mm from the surface, and nine of the simulated defects have a depth of t=0.5 mm from the surface. Three sides of the material will be left free and one side will be fastened as the experimental boundary conditions.

(a) Front side of CP

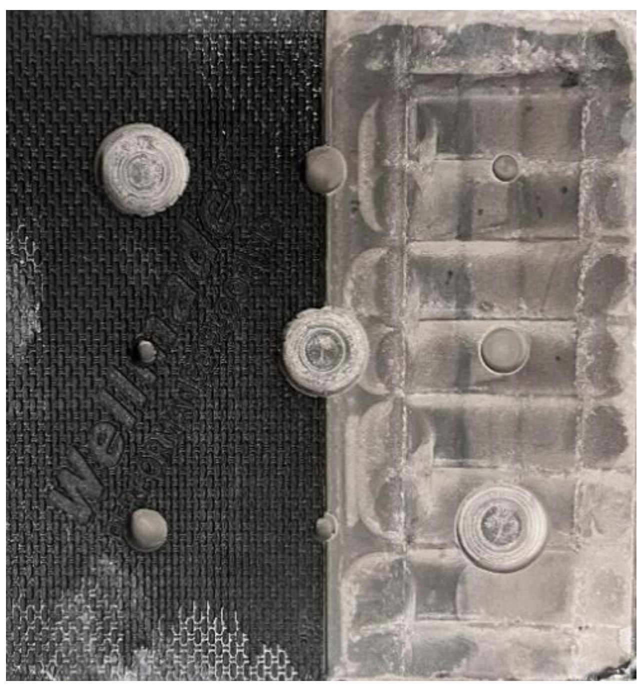

(b) Backside of CP

Figure 5.11. The specimen of t=0.5 mm with 9 simulated defects made by 9 flat bottomed blind holes of different diameters, with a 3 mm stage.

5.4.2 Experimental Results

In the following step, the outcomes of the experiment will be discussed and analyzed. For the purpose of this verification test, vacuum loading was utilized, and the fringe pattern of AL05 was chosen for testing at Δ88 kPa loading. While Figure 5.12 depicts the fringe pattern of AL05 when subjected to 88 kPa, Figure 5.13 depicts the three-dimensional surface when subjected to this stress. Next, the image is processed using a technique called segmented fitting. The structure is depicted in Figure 5.14 after it has been processed. It is possible to identify only three defects. A representation of the outcomes of the polynomial regression equation fitting approach may be found in Figure 5.15.

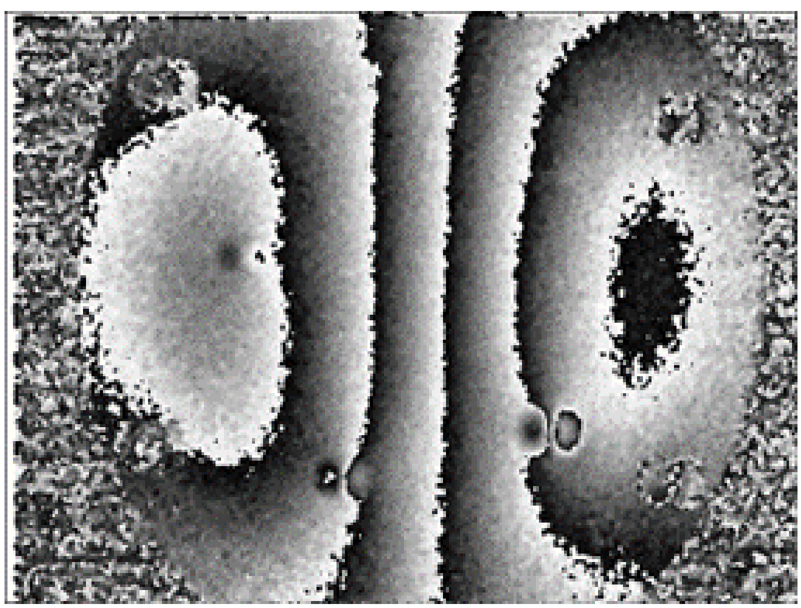

Figure 5.12 88 kPa 0.5mm depth defects

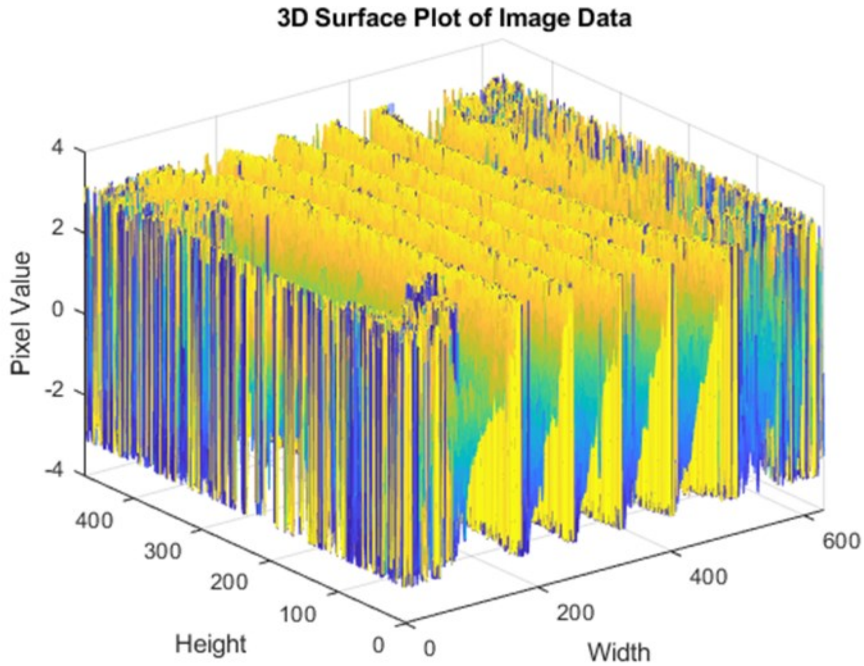

Figure 5.13 3D surface plot

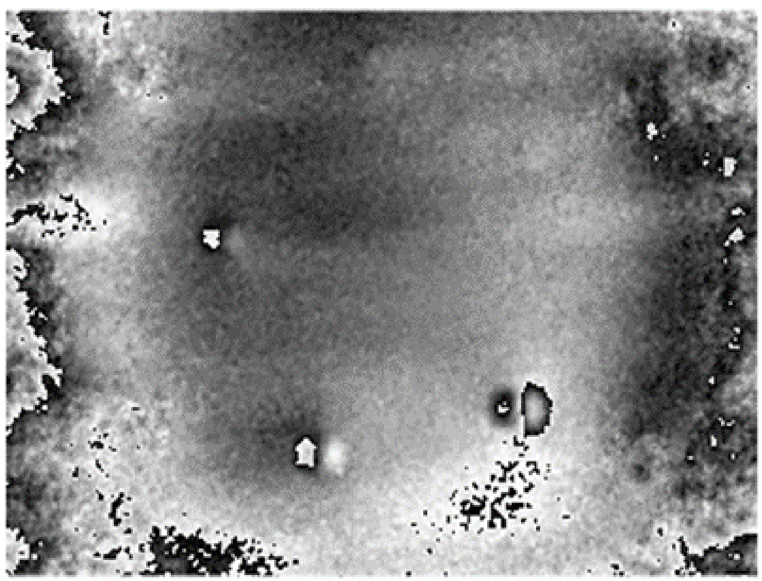

Figure 5.14 Result from segmented method

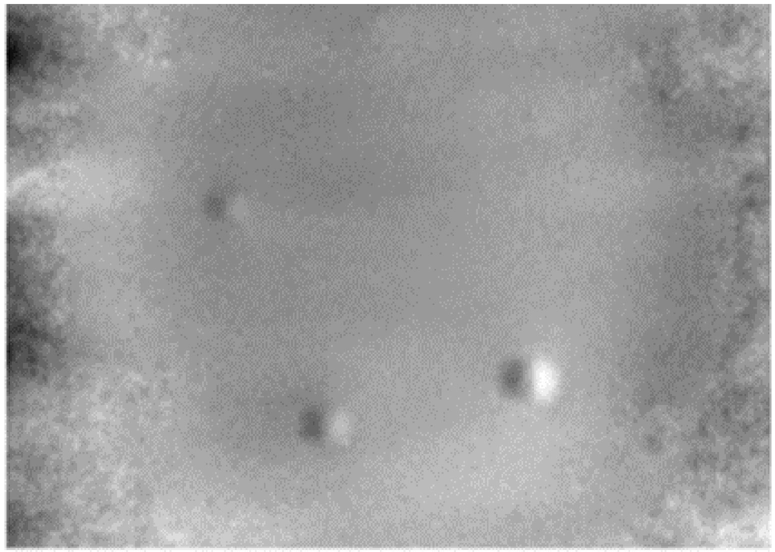

Figure 5.15 Result from polynomial regression fitting method

In order to verify the effectiveness and applicability of the segmented fitting method, the fringe patterns of temperature difference of 24 ºC are shown in Figure 5.16. The results of C3 under segmented fitting method are displayed in Figure 5.17. The different orders of polynomial regression fitting method are listed in Figure 5.18.

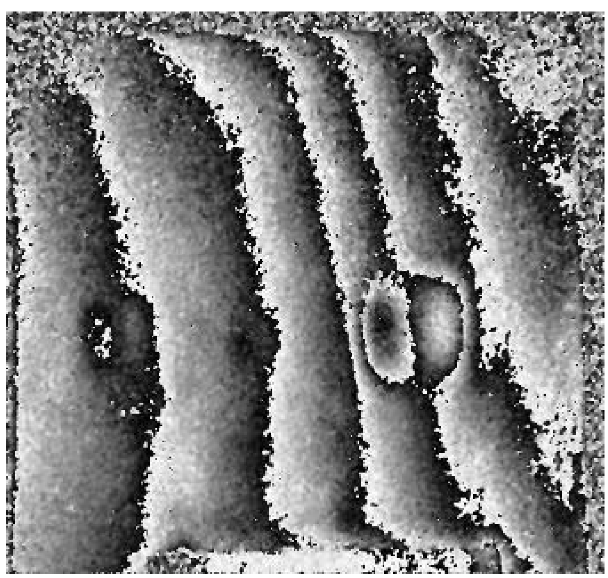

Figure 5.16 24 ºC temperature difference for C3

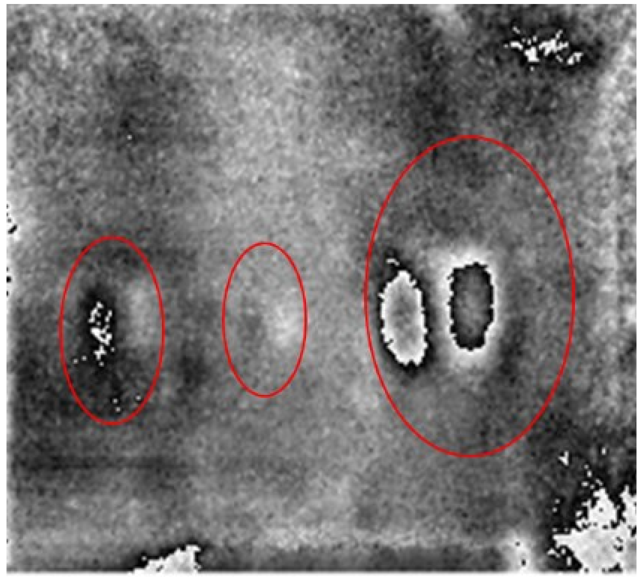

5.17. C3 results from the segmented fitting method.

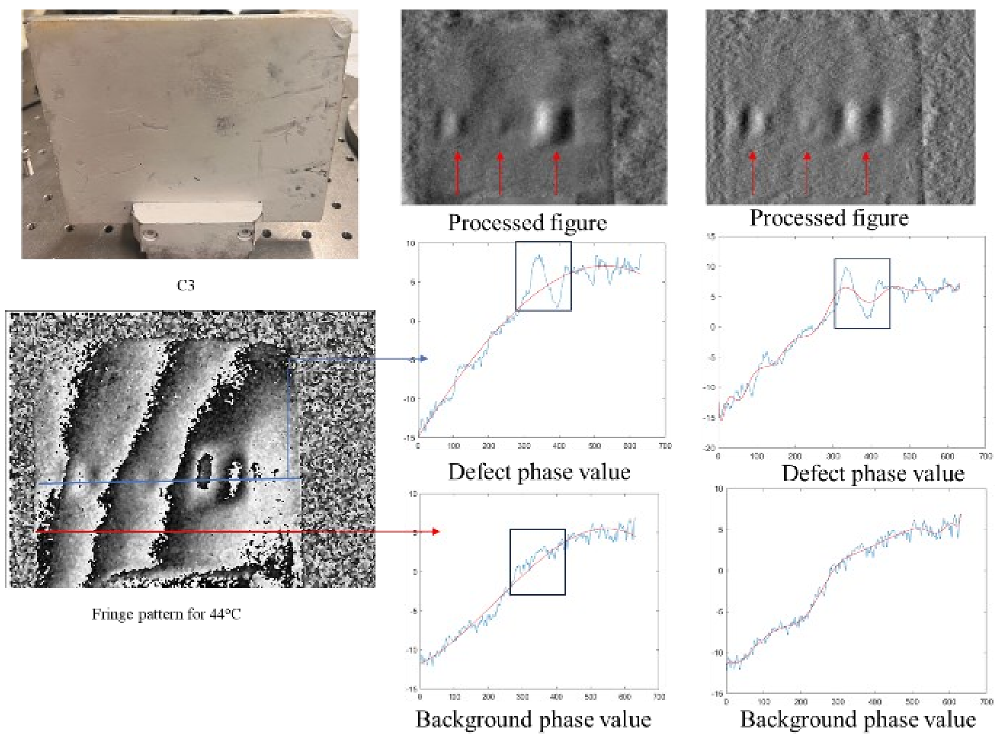

Figure 5.18 C3 results with large defect from polynomial regression fitting method.

For the complex condition, for the prefabricate defect composite (CP) with different thickness in the specimen ais chosen. Figure 5.19 shows the CP under thermal loading (Δt = 25 ºC) resulting. Figure 5.20 shows the result after removed the global deformation from the segmented fitting method. Also, result from polynomial regression fitting method show in 5.21。

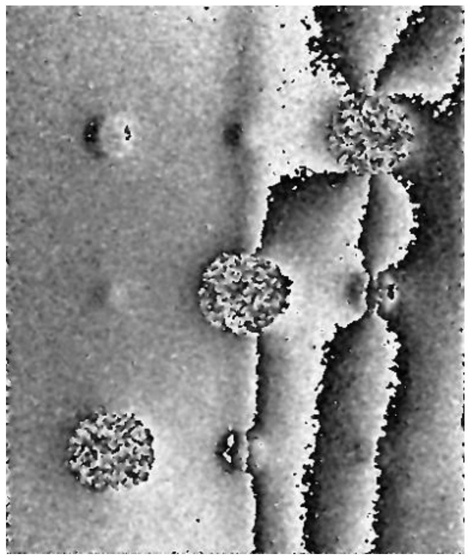

Figure 5.19 Δt = 25 ºC result of CP

Figure 5.20 CP results from the segmented fitting method.

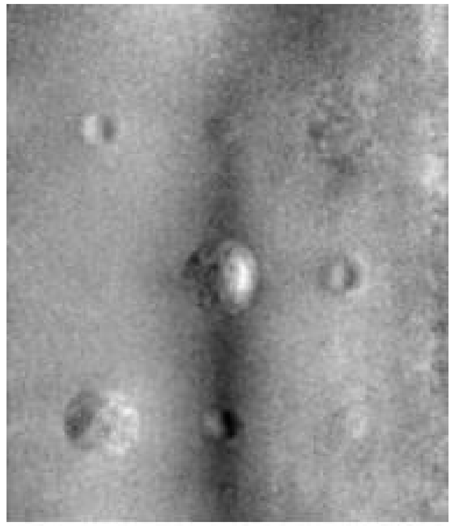

Figure 5.21. Result for CP from polynomial regression fitting method

5.5 Analysis and Discussion

5.5.1 Result analysis under the homogenous thickness material

According to Figure 5.14 and 5.15, it is possible to discover that the information regarding the position of the defect may be observed in a clear manner. The effectiveness of this fitting method in removing integer deformation under general conditions has been demonstrated through numerous experiments. This demonstrates that this method is an efficient way to get rid of global deformation. Following the use of the segmented fitting method, it is possible to observe that the outcomes are more transparent when compared to Figures 5.15 and 5.176. Because the fitting approach is based on the unwrapping method; hence, in order to reconstruct a smooth phase map in the unwrapped state, it is important to detect phase discontinuities that are generated solely by rotation. Adjusting the phase value by adding or subtracting multiples of 2π is the key to the unrolling method. In the event that the phase jumps at two consecutive places below or above π, respectively, this adjustment takes place. It is required to combine additive or subtractive approaches in order to reconstruct continuous phase patterns that incorporate noise and minor defect information. This is because the obstacles associated with finding discontinuities and calculating various values of 2π are difficult to overcome. Nevertheless, it is probable that this process will result in the loss of some information; hence, it is essential to keep as much information as possible throughout the processing of fringes patterns.

5.5.2 Result analysis for different fitting order of polynomial regression fitting method

According to Figure 5.18, results for higher-order fitting equations and lower-order fitting equations are shown and compared. Also, the phase values of the overall deformation of the background and the global deformation of the defect location are extracted and analyzed respectively. In Figure 5.18, it can be found that in the high-order fitting results, the entire specimen is eliminated, which is basically consistent with the phase value of the background information. As the fitting order increases, this result has a better effect on eliminating global deformation. However, the defect information also becomes unclear in the results of higher-order fitting. This is because the fitting order is too high, which causes the large defects information to be gradually taken into account in the overall deformation information, thus making the size and depth of the defect shallower, bringing errors to the observation. Appropriately increasing the fitting order of the fitting equation is more beneficial to eliminating global deformation, but too high a fitting order can also cause trouble in defect identification. In summary, fitting equations of different orders will affect the fitting technique in specific ways, making it difficult for novice operators to choose an appropriate fitting method.

5.5.3 Result analysis under the complex loading conditions

In this section, the processing results of the two methods for global deformation of complex deformations are discussed based on the results of CP shown in Figure 5.20 and Figure 5.21. First, from the results of the polynomial regression equation fitting method, the 20 mm diameter defect on the thinner platform is unclear, while the 6 mm diameter defect is almost invisible. This is because the conventional polynomial regression fitting method is based on the gray value of the continuous phase map to simulate global deformation. Complex deformation conditions make the selection of fitting equations more troublesome, thus bringing certain errors to the results. The presence of this error sometimes identifies large defective phase values as global deformations to the fitting algorithm, which is ultimately eliminated. The information of small defects can be considered as noise and becomes invisible after smoothing during the unwarping process. This result proves that this method is not suitable for extracting complex deformation situations and small defect information. Secondly, in the segmented fitting method, there is a lot of noise, which makes the 20 mm diameter defect on the thicker platform unclear, and there are many fringes representing global deformation. This is because segmented fitting is performed based on the changes in the terms in each fringe. When in complex deformation, the fringe near the defect is distorted, causing the fitting results to be affected at the location of larger defects. On the other hand, the stage on the thicker side basically has no fringes in the original image, and the first fringe encountered later is at the delamination position. When the first fringe encountered is used as the boundary, the phase value that determines the fitting equation will be affected by the fringe quality and noise, causing the stage on the thicker side to produce outer fringes. This shows that this method is not suitable for global deformation removal in complex deformation situations with large defects.

5.6 Conclusion

This section's primary objective is to conduct an analysis of the many approaches that have been used in the past to eliminate global deformation and to suggest a novel fitting method that is based on fringe pattern in order to display defect information in a manner that is simple to comprehend. Through the successful elimination of global deformation, this approach works toward the goal of accurately conveying defect information. A number of experiments have demonstrated that this method is capable of successfully preserving accurate data without introducing additional fringes that could lead to confusion. Additionally, it results in a significant enhancement of the capability of digital shearography to effectively locate and capture defects. On the other hand, the noise information of the segmentation method would increase, this method can be solved by employing multiple filtering times. In general, for simple deformations, the segmented fitting method can provide more detailed information than the polynomial regression fitting method, but it is not suitable for complex deformations. For complex deformation situations, the polynomial regression fitting method can extract small defect information, while the segmented fitting method is not suitable for extracting large defects.

CHAPTER SIX

INCREASE SMALLEST DETECTABLE VISUALIZATION DEFECT: THE NOVEL EXPERIMENT BASED METHOD FOR REMOVING GLOBAL DEFORMATION

6.1 Introduction

In the aerospace sector, it is imperative to subject all manufactured components to thorough inspection, to ensure their suitability for operational deployment. Conventional Non-Destructive Evaluation (NDE) techniques, including x-ray, eddy current, ultrasonic, and acoustic emission techniques, are often unsuitable for defect detection or necessitate calibration. Digital shearography is an optical interference technique, which is applicable for NDE inspection of a wide variety of composite materials, such as glass fiber and carbon fiber reinforced plastics, honeycomb structures etc. Shearography is ideally suited for such applications due to its full-field inspection capabilities, non-contact nature, and high measurement sensitivity, as well as to its direct measurement of the first derivative of the deformation in the shearing direction, i.e., strain information [124-129]. The first derivative of the deformation measured by shearography is always related to the shearing direction: the words "in the shearing direction" will be omitted in the following text.

In Shearographic Non-Destructive Testing (NDT), defects are found by identifying anomalies in the surface deformation caused by internal defects under a small load. Because shearography measures the first derivative of the deformation, these defects generate butterfly fringe patterns on the surface [15,16,130]. For very small defects, the butterfly fringe pattern is often masked by the global deformation, therefore making the defect detection and visualization difficult [131-132].

It is important to note that the key to successful digital shearography inspection is to highlight the contrast between information from defect-induced deformation and global deformation. As long as the defect signal is large enough to be detected (for example, the ratio of defect signal to background signal is greater than 2), defect visualization is straightforward.

This study addresses the issues presented in conventional approaches. Firstly, all previous methods rely on a continuous phase map obtained after unwrapping: a continuous phase map often reduces the contrast between defect and background information, making smaller defects harder to detect. Secondly, the continuous phase map can be irregular under complex deformations, rendering surface fitting or interpolation processes difficult to execute. Lastly, the use of machine learning techniques can help remove the information from global deformation, but this approach requires the collection of large amounts of data, and its application is often limited to the substrate material used for model training. In contrast, this proposed novel approach for the removal of the information from global deformation is quick, practical, and broadly applicable: it relies on the direct analysis of a shearogram. If the resolution of the hardware is 8-bit, which is composed of multiple fringes with gray levels varying from 0 to 255, each fringe can display more detailed information. Two phase maps are recorded during a single elastic loading process, one at a relatively small load, and the second one at a larger load (i.e. one more phase map than conventional digital shearography is recorded), therefore avoiding the issues typical of conventional methods. The information from the phase map obtained at the relatively small load is used to generate a shearogram containing the information from global deformation at the higher load, via a linear elastic coefficient that is calculated from the two original (unwrapped) shearograms. The information caused by global deformation is then removed, revealing the defect information.

6.2 Highest point coefficient method

An experimental procedure, referred as the "point coefficient method", is developed to help remove the information from global deformation information while retaining defect information. A linear relationship exists between the 1st derivative of the global deformation and the applied load, provided that the specimen is loaded within its elastic range. Two loads of different magnitude (identified as a relatively small load and a relatively large load) are applied to the test sample, and two corresponding shearograms are obtained. The literature shows that defects and defects cannot be detected in a shearogram when the applied load is relatively small [36]. The small-load shearogram, therefore, only contains information on the phase difference generated by the sample's global deformation, and is free of any defect information. The large-load shearogram, however, includes the defect information, as well as the sample's global deformation. In order to minimize the effect of noise information, selecting the smallest available phase distribution after the first fringe is generated is recommended. The phase difference Δ_{global} at the relatively large load can be determined by multiplying the small-load shearogram by the established linear correlation coefficient *C*. Then, using equation 6.1, the defect information can be extracted. The experimental point coefficient method is explained in detail in the flow chart in Figure 6.1.

$$\mathit{\Delta} = \Delta_{global} + \Delta_{defect} \rightarrow \Delta_{defect} = \mathit{\Delta} - \Delta_{global} \tag{6.1}$$

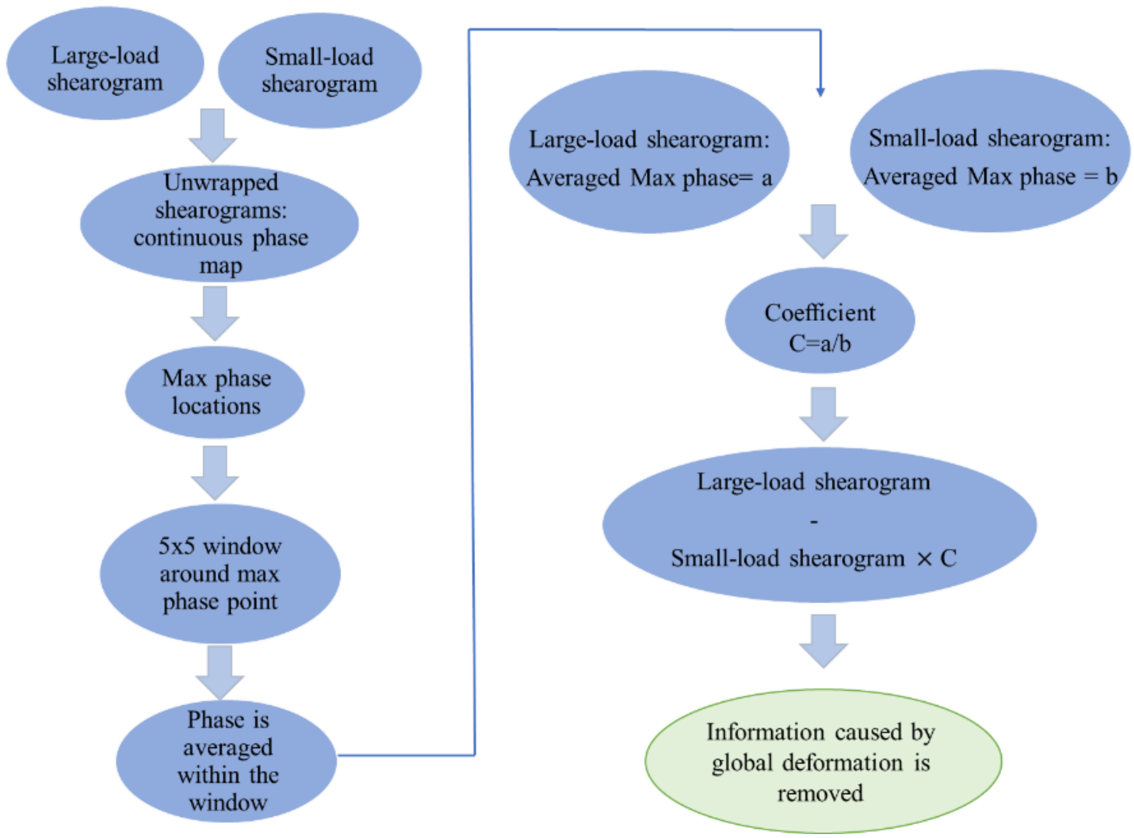

Figure 6.1. Schematic of experimental point coefficient method

As illustrated in Figure 6.1, a novel developed technique for removing the information caused by global deformation is the experimental point coefficient method. This method uses digital shearography to record an additional phase (Δ_{P1}') during the loading process and obtains a relatively small loading shearogram (Δ_{P1}'-Δ_{P1}) by subtracting the phase distribution before deformation. Figure 6.2 shows the phase distributions that were recorded during the loading process at internal pressures difference of 88 kPa (Figure 6.2 a), 28 kPa (Figure 6.2 b), and 0 kPa (Figure 6.2 c, unloaded). The resulting shearograms are shown in Figure 6.3.

The linear correlation coefficient *C* is determined from the two shearograms. First, the locations of maximum and minimum phase are identified on the large-load shearogram. Then, the phase value is averaged within a sampling window centered on these two points, as shown in Figure 6.4, to limit the impact of noise on the coefficient *C*. In equation 6.2, the averaged maximum phase value. The same operation is performed on the small-load shearogram, and the variable *b* in equation 6.2 refers to the respective averaged maximum phase value. The linear correlation coefficient *C* is the ratio between *a* and *b*. The surface representing Δ_{global} is obtained by multiplying the small-load shearogram by C, and is subtracted from the large-load shearogram, leaving only the defect information.

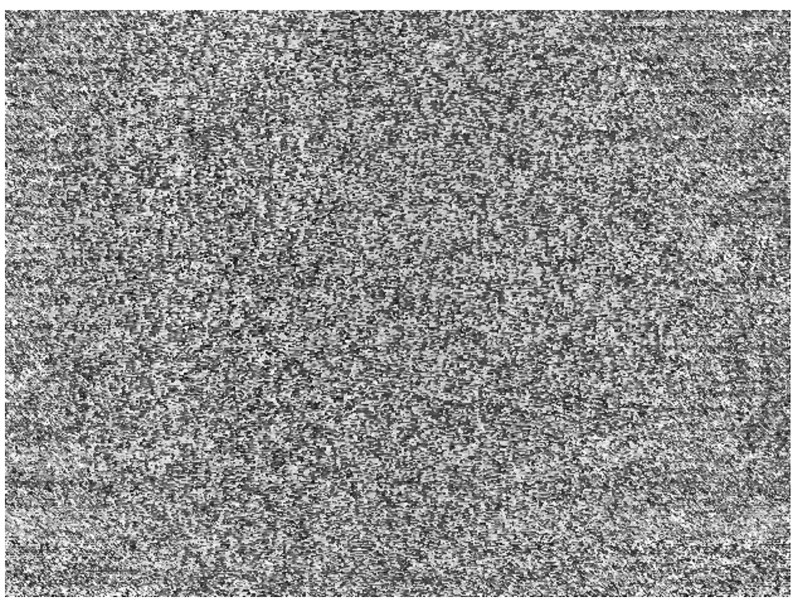

(a) Phase at 88 kPa

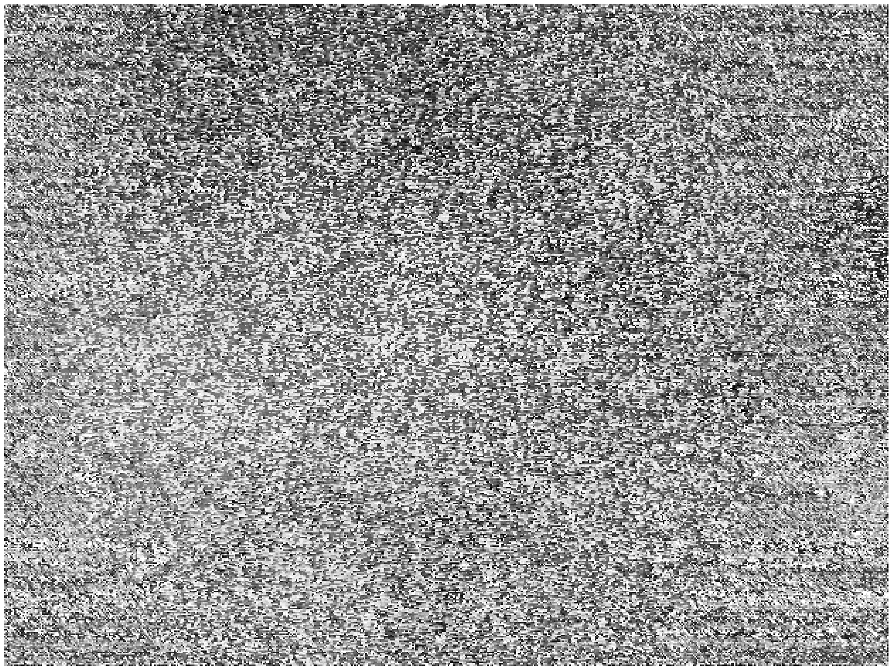

(b) Phase at 28 kPa

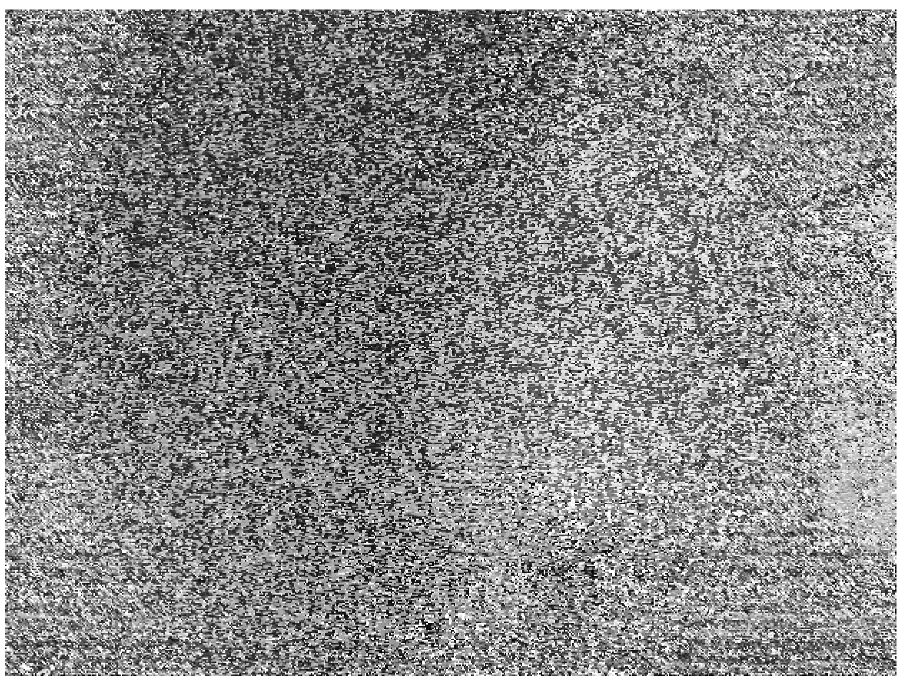

(c) Phase at 0 kPa

Figure 6.2. Phase maps during the loading process

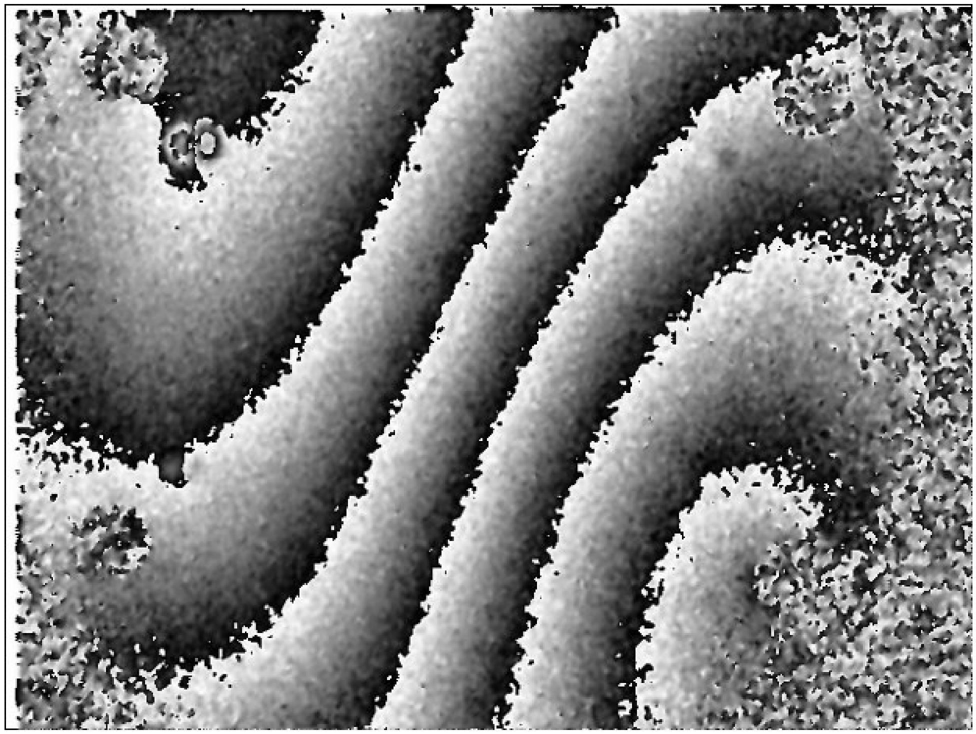

(a) Large-load (88kPa) shearogram

(b) Small-load (10kPa) shearogram

Figure 6.3. Fringe patterns for the 2024 Aluminum disc

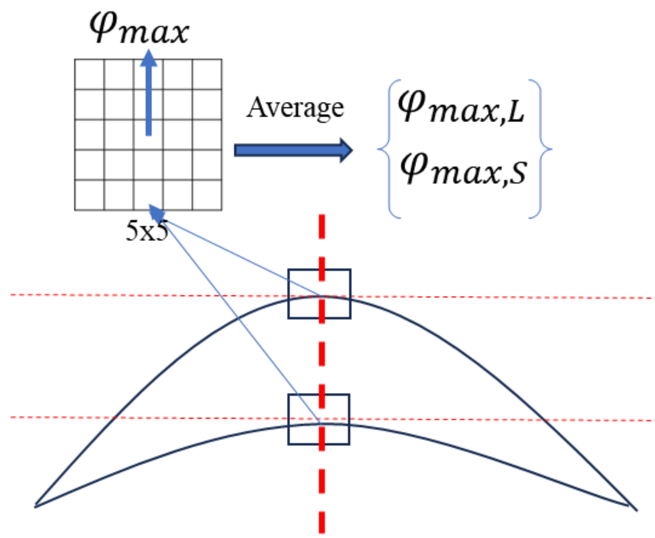

Figure 6.4. Determination of the coefficient *C*

$$a = \varphi_{\max\,(L)}$$
$$b = \varphi_{\max\,(s)} \qquad (6.2)$$
$$C = \frac{a}{b}$$

Sampling window sizes of 3x3, 5x5, and 7x7 pixels are used to calculate the value of the coefficient *C*, and the results are compared in Figure 6.5. In the range of 3x3, 5x5, and 7x7 window size does not significantly affect the value of the linear coefficient *C*, based on that, the 5x5 window size was selected.

The point coefficient method can be used to improve digital shearography's defect detection capability for samples made of various materials and with uniform thickness. Moreover, the experimental nature of this method allows to obtain fast and highly reproducible results.

It should be emphasized that the point coefficient method is suited for materials which has a uniform structure with same thickness and under elastic loading. Under these conditions, the coefficient C should be the same at every point. Therefore, the determination of the C value could be conducted at any point on the surface of the object. It is however recommended to calculate the C value at the location with the maximum phase value, to maximize the method's sensitivity.

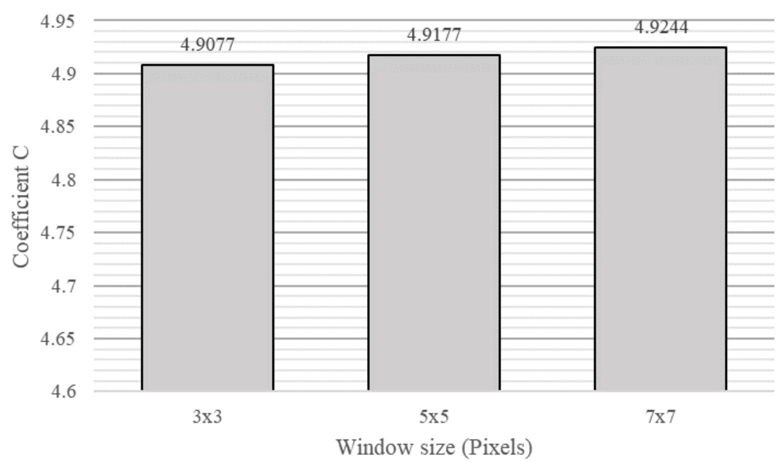

Figure 6.5. Coefficient comparison for different window sizes.

6.3 Surface coefficient method

The experimental point coefficient method can be applied to parts with relatively simple deformation fields. Another approach, denoted "experimental surface coefficient method", is developed for more complex deformation fields, common for samples with nonuniform thickness and/or material properties. The two approaches share the same fundamental principles: during a single loading process, an additional shearogram is recorded at a relatively small load. The information from global deformation is then eliminated by using the linear relationship between the small-load and large-load shearograms. The working principle of the experimental surface coefficient approach is illustrated in Figure 6.6. a_{ij} and b_{ij} represent the relative phase maps for the large-load and small-load shearograms, respectively, and are divided to obtain the correlation coefficient C_{ij}, as shown in equation 6.3. Differently from the previous approach, the coefficient varies with the i and j coordinates. In equation 6.3, $\varphi_{(i,j)}$ and $\varphi'_{(i,j)}$ represent the large-load and small-load phase maps.

$$C_{(i,j)} = \frac{a_{(i,j)}}{b_{(i,j)}} = \frac{\varphi_{(i,j)}}{\varphi'_{(i,j)}} \tag{6.3}$$

The large-load phase map $\varphi_{(i,j)}$, however, includes information relative to the defects, which can affect the calculation of the correlation coefficient C_{ij}. A combination of fitting and experimental methods is therefore used to eliminate the contribution of the defects to the calculation of C_{ij}, as shown in Figure 6.7. Once the defect information is filtered out of the correlation coefficient, the information global deformation is obtained as the Hadamard product of C_{ij} and the small-load shearogram.

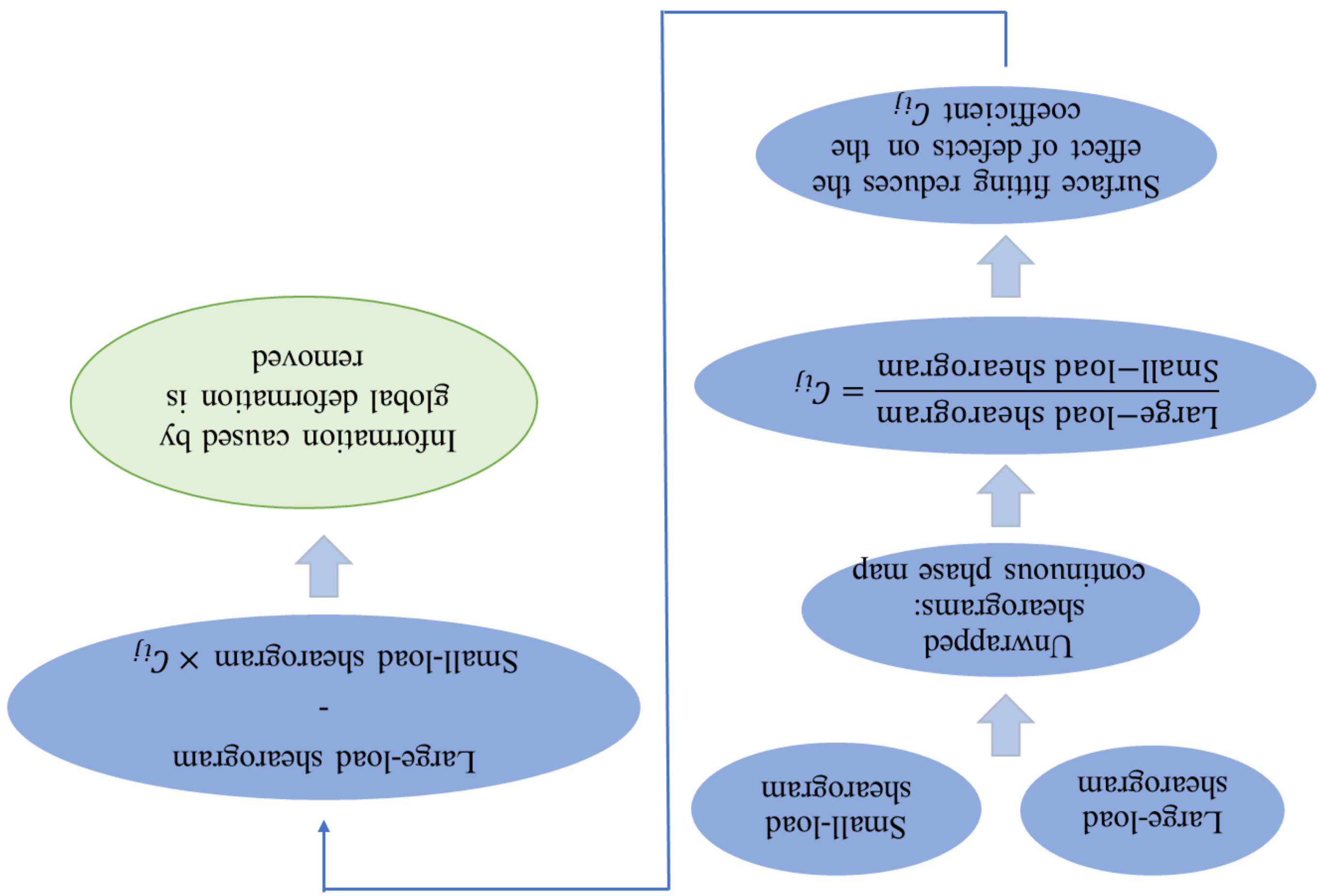

Figure 6.6. schematic of experimental surface coefficient method

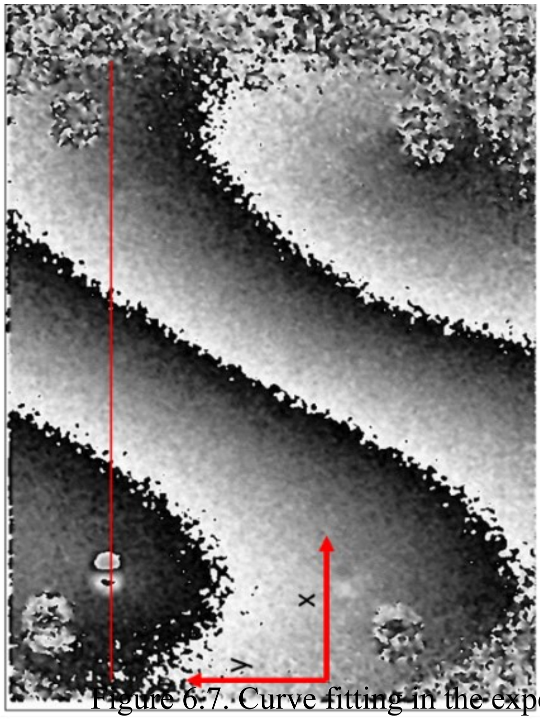

Figure 6.7. Curve fitting in the experimental surface coefficient method (defect informat

180 pixels

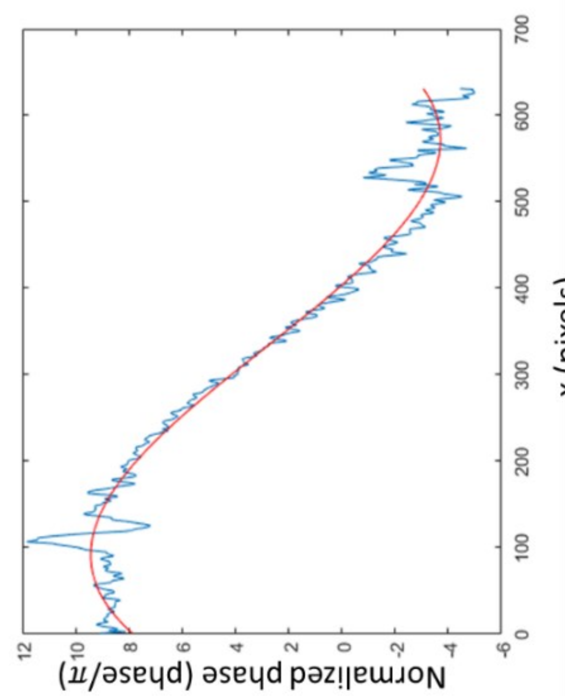

6.4 Experiment and results

6.4.1 Specimen preparation

The defect detection performance of the two novel approaches is assessed using test samples made of two different materials, manufactured with known defects. The sensitivity of digital shearography after the removal of the information global deformation is tested.

The first test specimen (AL05) has homogeneous thickness and is made of Aluminum. Five flat-bottomed holes are drilled on a circular plate having a diameter of 166 mm and a thickness of 12.7 mm (0.5 in.). The holes are drilled to a depth such that the flat bottom is 0.5 mm below the “front side” surface shown in Figure 6.8 (i.e. the depth of the holes is 12.2 mm). The holes have varying diameters: 3, 4, 5, 5.9, and 8.2 mm, simulating defects of different sizes. Six evenly spaced through holes are utilized for fastening the plate to the shearography setup.

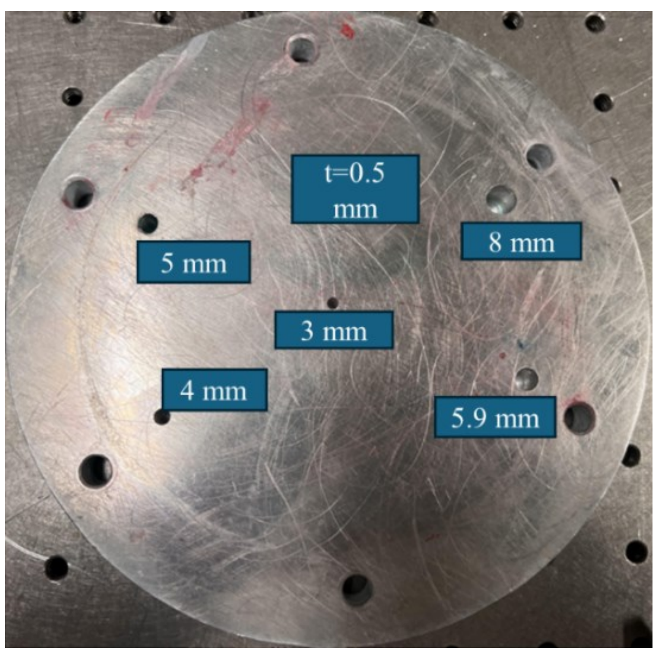

(a) Backside of AL05

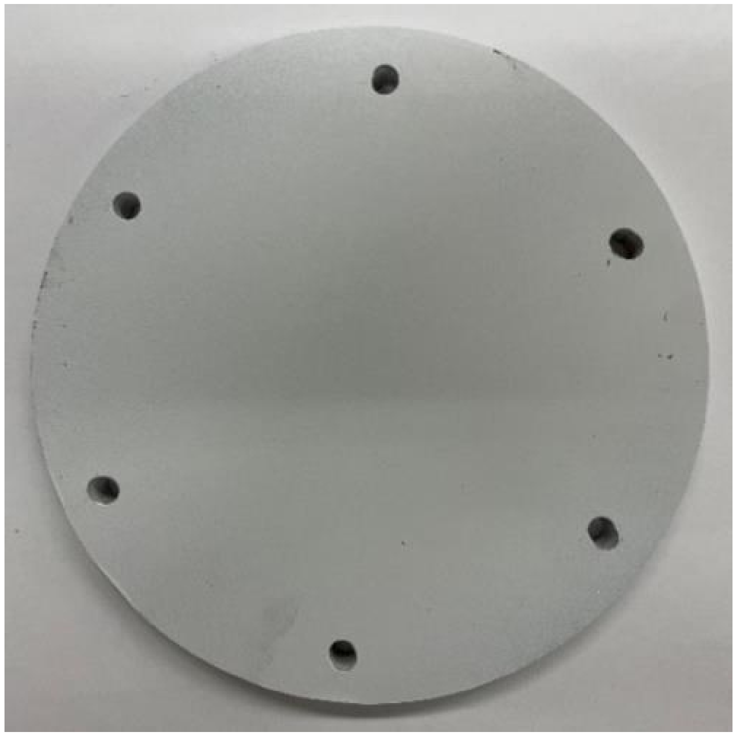

(b) Front side of AL05

Figure 6.8. The specimen of t=0.5 mm with 5 simulated defects made by 5 flat bottomed blind holes of different diameters, left: back side, right: front side to be tested

The second specimen is made of the 150 mm x 145 mm composite laminate (CP) shown in Figure 6.9. The varying (stepped) thickness and the non-isotropic properties of the test sample are chosen to verify the defect detection capabilities of the surface coefficient method in the case of more complex deformations. The total thickness of the specimen is 5.65mm, and a 3 mm-thick layer of material is removed on one side to simulate delamination's. Nine holes of different diameters (6, 10, and 20 mm) are drilled on the specimen, to a depth of 0.5 mm from the front side. Only one side of the sample is constrained (clamped) during testing.

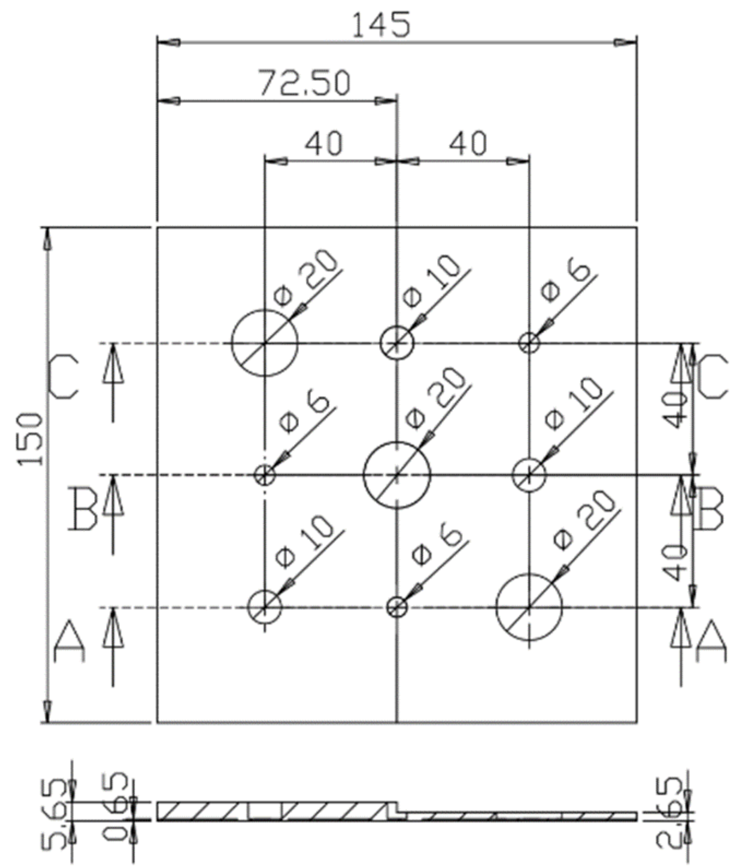

(a) Schematic of CP specimen

(b) Front side of CP

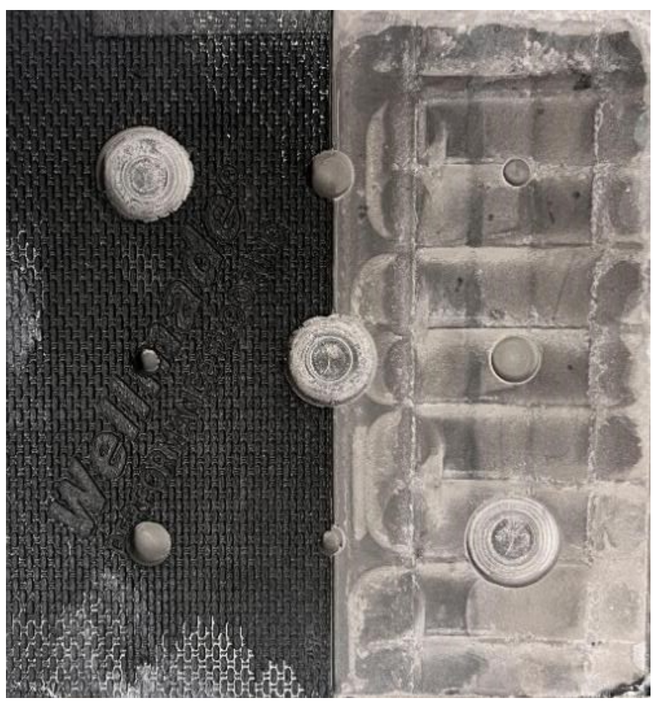

(c) Backside of CP

Figure 6.9. Composite laminate (CP) specimen, with 9 flat bottomed blind holes of different diameters, and a 3 mm delamination stage.

6.4.2 Experimental setup

The setup utilized in this study is shown in Figure 6.10. Thermal and internal pressure loading are the predominant loading techniques employed in shearography. Internal pressure (vacuum) is used to apply a uniform out-of-plane load on the AL05 specimen, to validate the effectiveness of the novel experimental coefficient method. Figure 6.10 (a) depicts this configuration, with the AL05 specimen closing one end of a cylindrical pressure vessel.

The deformation resulting from the application of a thermal load is more complex, as it is affected by the material's heat capacity and conductivity, as well as by convective flows and other interactions with the environment. Thermal loading is therefore applied to the CP specimen to validate the capabilities of the surface coefficient method. This configuration is shown in Figure 6.10 (b): two 1000W halogen lamps illuminate the sample for three minutes. To ensure that the specimen is heated uniformly, the two halogen lamps are placed at the same angle. The phase map is recorded while the specimen is cooling down, to prevent measurement errors caused by the light reflection. An extended helium-neon laser with a 50 mW power output and a 632.8 nm wavelength is used for the shearographic measurement of both samples. The shearing device is a modified Michelson interferometer that incorporates a piezoelectric transducer (PZT) driven mirror to facilitate the phase-shifting procedure.

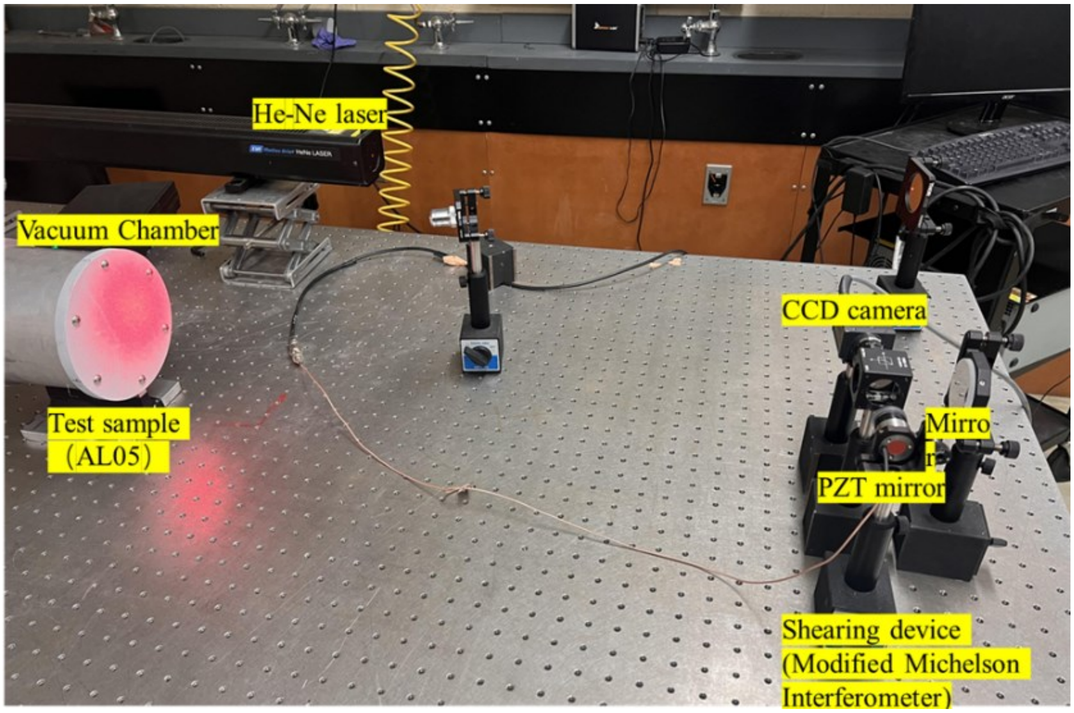

(a) Vacuum loading setup

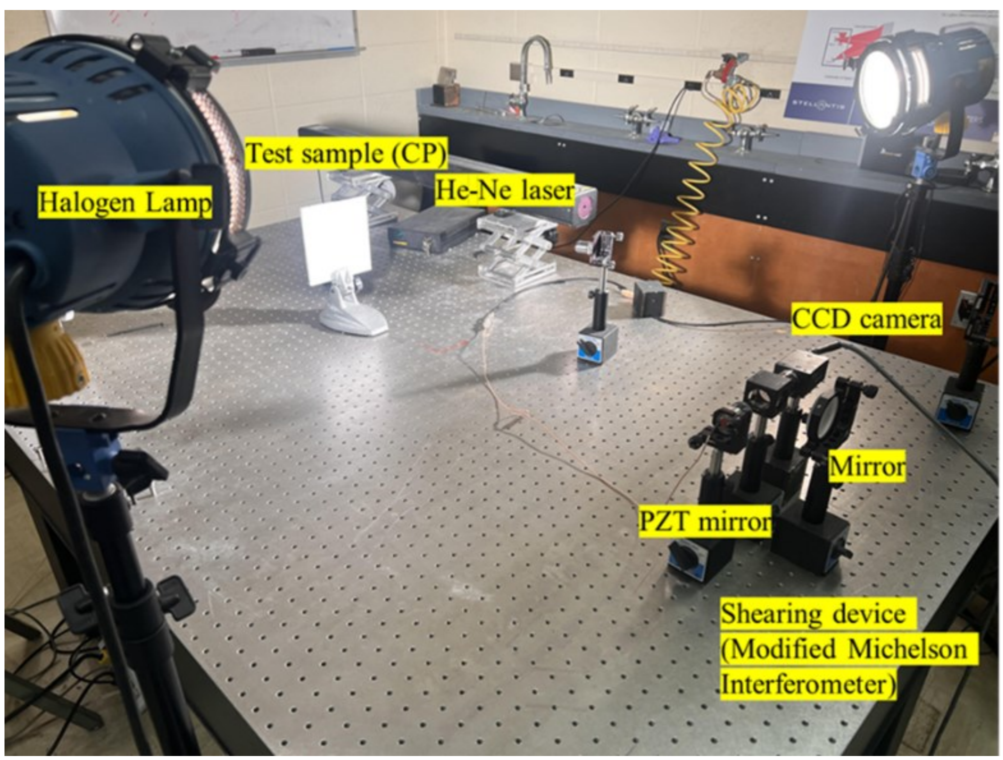

(b) Thermal loading setup

Figure 6.10. The setup of digital shearography for the experimental validation

6.4.3 Results

In this section, the information from global deformation on the vacuum-loaded AL05 and the thermally-loaded CP specimens is removed by using (a) the experimental point coefficient method, (b) the experimental surface coefficient method, and (c) conventional fitting techniques. The results are then compared.

The large-load and small-load shearograms of the AL05 specimen during the loading process are displayed in Figure 6.11 (a) and 6.11 (b), respectively. Figure 6.11 (a) shows two “butterfly” patterns on the upper left and lower left corners of the image, corresponding to the two largest defects, with diameters of 5.9 and 8.2 mm. The three smaller defects cannot be detected without eliminating the information caused by global deformation, even with a pressure differential of $\Delta p = 88$ kPa.

When using an averaging window size of 5 x 5 pixels, the correlation coefficient C is calculated as 4.9177. The information caused by global deformation is then eliminated using the experimental point coefficient method, and the resulting shearogram is displayed in Figure 6.12. The background fringes visible in Figure 6.11 (a) are removed, improving the clarity of the defect information. Figure 6.13 shows the shearogram obtained by using the experimental surface coefficient to remove the information caused by global deformation. The red circles indicate the location of the defects.

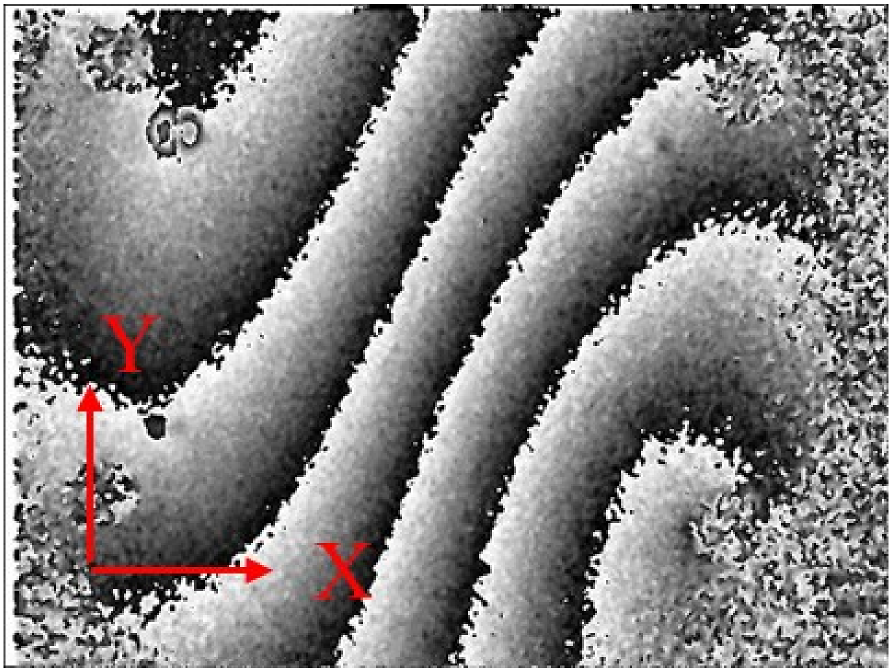

(a) AL05 fringe pattern under Δp=88kPa

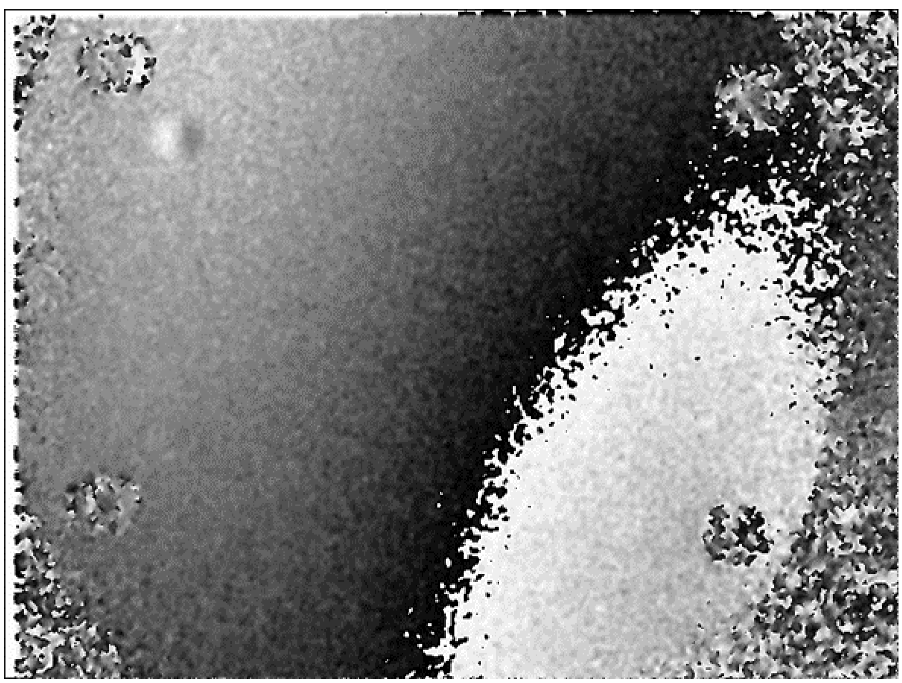

(b) AL05 fringe pattern under Δp=18 kPa

Figure 6.11. AL05 shearogram

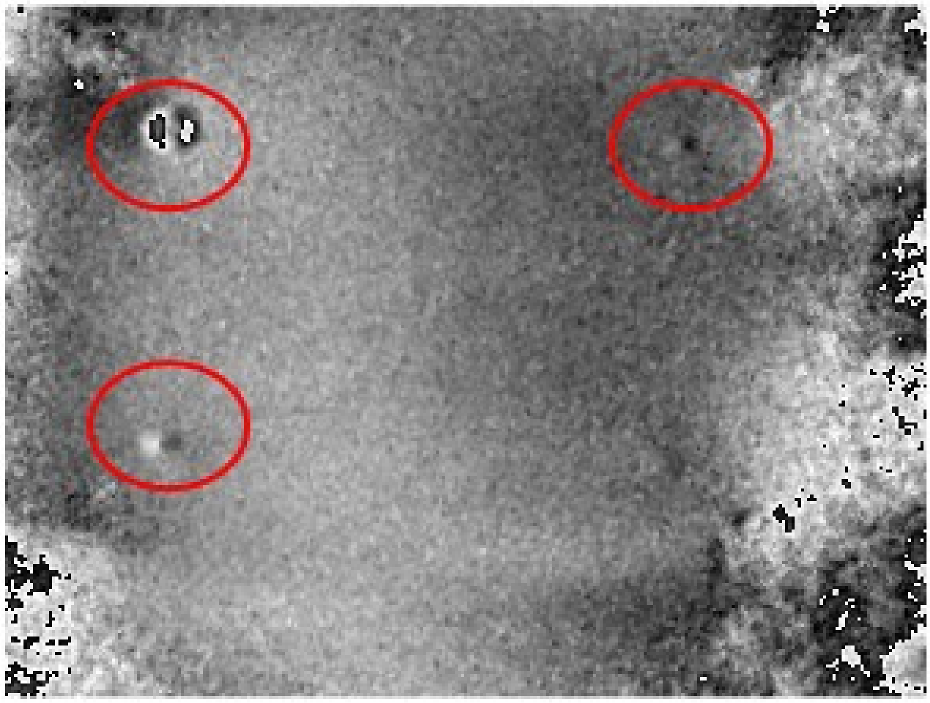

Figure 6.12. The processed shearogram using the experimental point coefficient method

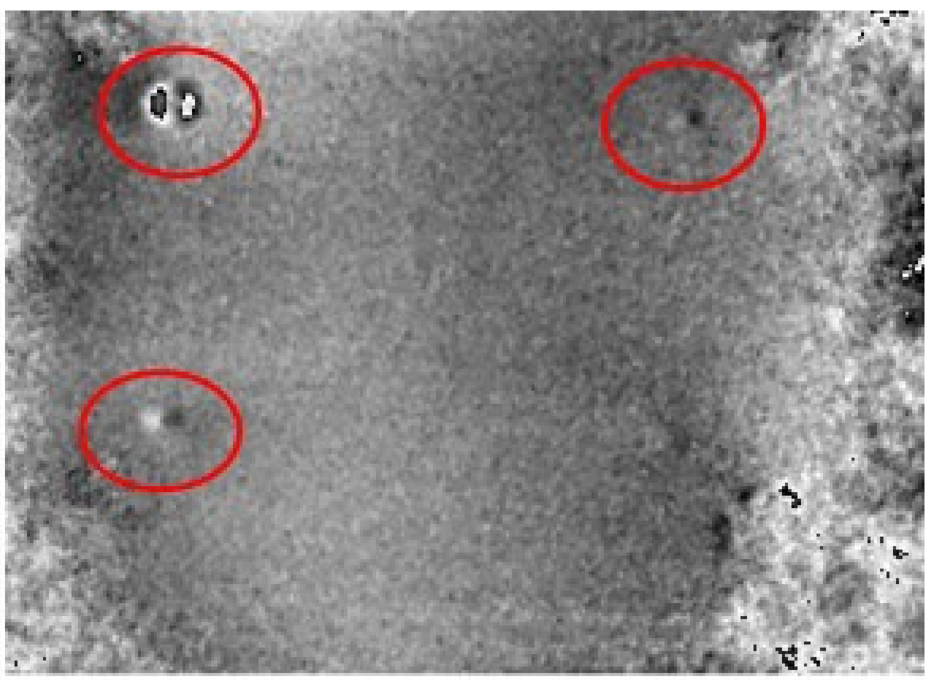

Figure 6.13. The processed shearogram using the experimental surface coefficient method

The large-load and small-load shearograms for the CP specimen are shown in Figures 6.14 (a) and 6.14 (b), respectively. The shearing amount is 3 mm and the shearing is in the x direction. The determination of the shearing amount is based on the size of the smallest defect. According to previous studies [12, 16], once the shearing amount reaches half of the defect size, it has reached its maximum measuring sensitivity (in terms of shearing amount). The smallest defect is 6 mm in diameter; therefore 3 mm was selected for the shearing amount. Regarding the shearing direction, the defect has a circular shape, thus, the shearing direction does not play an important role. Figure 6.14 (a) demonstrates that the larger defects (10 mm and 20 mm in diameter) can be identified prior to the elimination of the information caused by global deformation at the temperature difference $\Delta t = 25$ ºC. Furthermore, smaller defects (6 mm in diameter) are nearly invisible on the thinner portion, barely recognizable at the step junction, and visible but overshadowed by the global deformation (and therefore can be easily missed) in the thicker portion. Figure 6.15 shows the information caused by global deformation removal results for the experimental point coefficient approach. The smaller (6 mm-diameter) defects are visible across the entire sample, regardless of the specimen thickness. However, extra fringes are generated in the thicker portion, masking the 20 mm-diameter defect in the lower left corner. Figure 6.16 displays the results for the experimental surface coefficient approach. All defects are clearly detected and no extra fringes are formed.

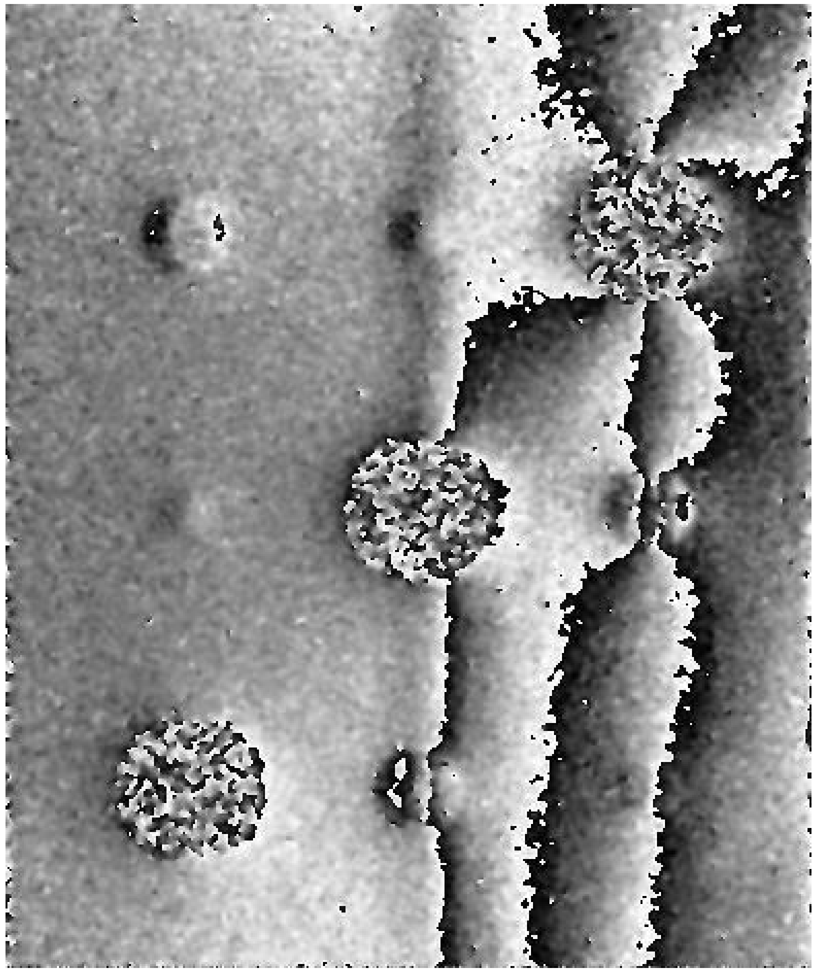

(a) Large-load phase map

(b) Small-load phase map

Figure 6.14. Phase maps for CP specimen during the test

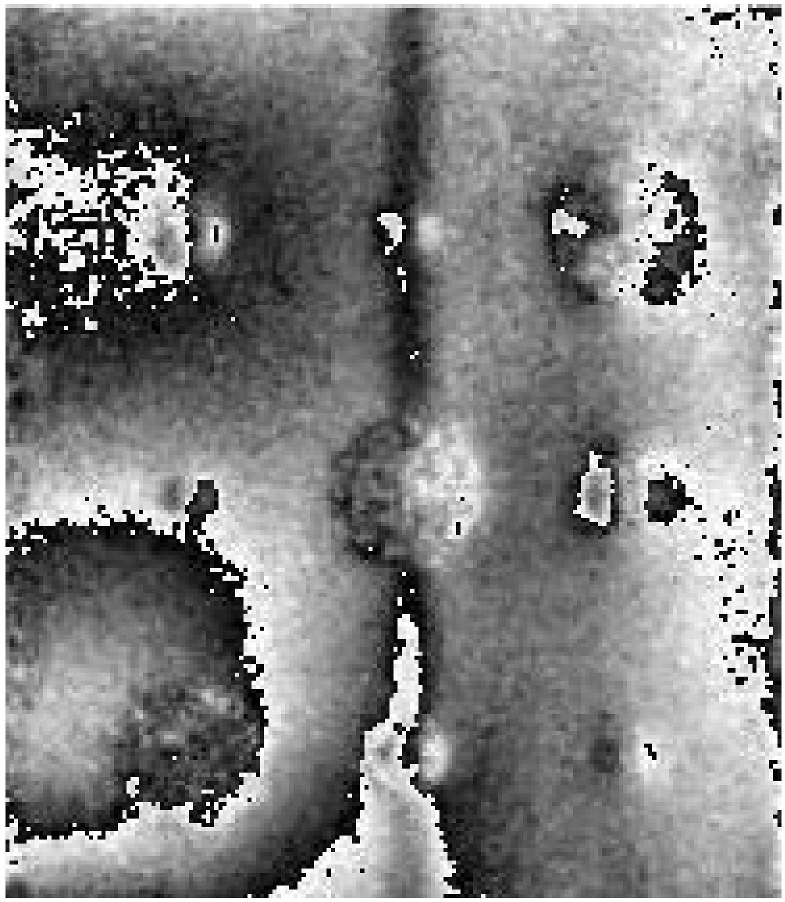

Figure 6.15. Shearogram of CP specimen obtained with the experimental point coefficient method

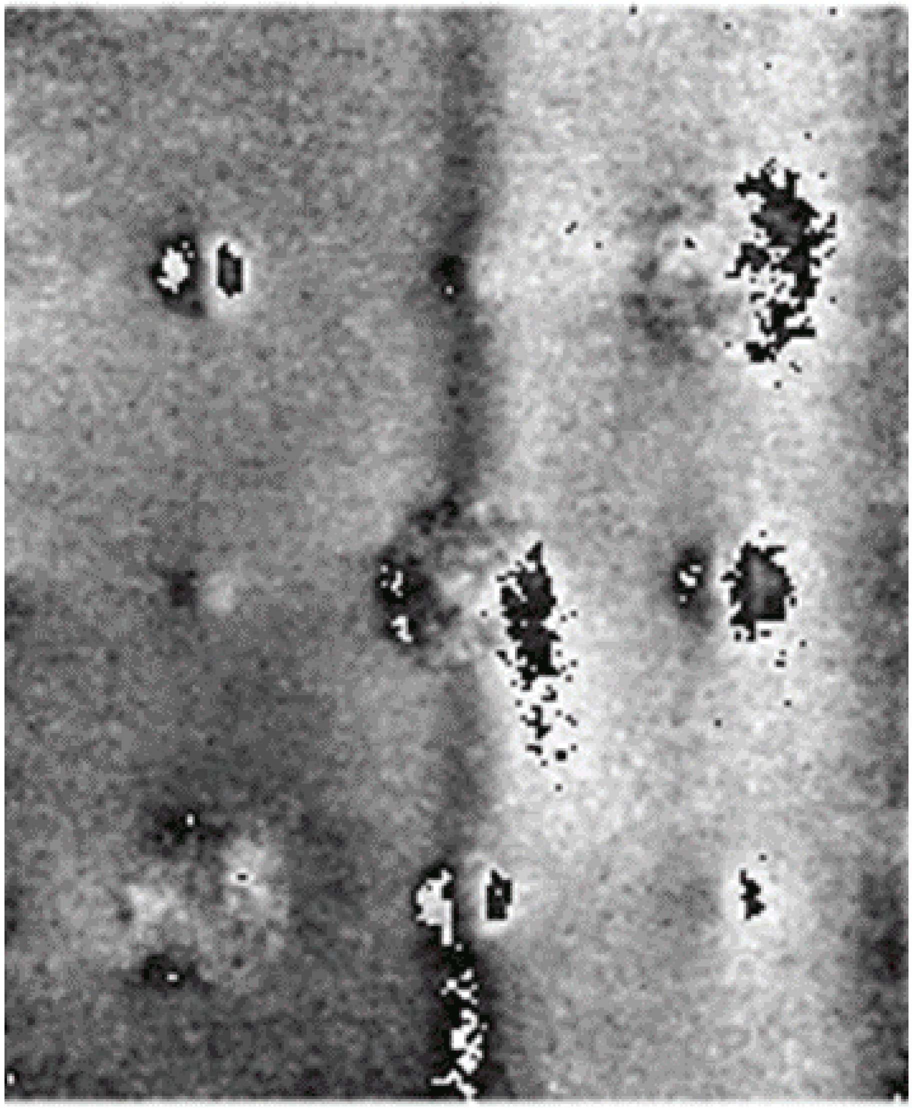

Figure 6.16. Shearogram of CP specimen obtained with the experimental surface coefficient method

6.5 Result and discussion

The two novel experimental coefficient approaches described in this section are validated by experimental testing, which showed a significant enhancement of the sensitivity of digital shearography through the elimination of the information caused by global deformation. In this Section, the application scope and the results of the two novel experimental coefficient methods are discussed under various deformation conditions.

6.5.1 Difference between experimental surface and point coefficient methods

In this section, the difference between the two novel approaches is analyzed, and the appropriate applications for each method are discussed.

6.5.1.1 Comparison between experimental point and surface coefficient methods for specimens of uniform thickness

Both methods effectively eliminate the fringes representing the information caused by global deformation of the AL05 specimen, as shown in Figures 6.12 and 6.13. Furthermore, both methods enhance the visibility defects with diameters of 8.2 mm, 5.9 mm and 5 mm. Please note that there are noises on the left and right sides of Figures 6.12 and 6.13. These are caused by backgrounds of air or other materials because these areas are out of test sample as shown in Figure 6.11 (a) and (b). If the test area is observed, Figure 6.13 is more uniform in the phase distribution than Figure 6.12, this is because Figure 6.13 uses the surface coefficient method which is more accurate than the point coefficient method. However, the surface coefficient method is more complicated than point method. Although a slight variation in phase distribution can be seen from Figure 6.12, it does not affect the identification of the defects.

In summary, if the specimen to be tested has uniform structure with same thickness, the experimental point coefficient approach can effectively eliminate the information caused by global deformation, while being computationally more efficient than the surface coefficient approach, easy to use, and practical. Although both methods can be used, the experimental point coefficient method is recommended.

6.5.1.2 Comparison between experimental point and surface coefficient methods in complex deformation conditions

When specimen to be tested has a nonuniform structure with different thickness, as shown the CP specimen shown in Figure 6.9. The experimental surface coefficient approach is recommended. As shown in shearograms of Figure 6.14, thinner areas produce more fringes due to the larger deformation. In the large-load shearogram (Figure 6.14a), the smaller (6 mm-diameter) defect on the thicker stage (left middle) is hard to be found, because the magnitude of deformation caused by the defect is small compared with the other areas. Similarly, on the thinner stage the smaller defect (lower right corner) is difficult to be found either because of the intense global deformation fringing. The information caused by global deformation is almost eliminated in the thin portion when using either approach. All smaller defects are clearly demonstrated on both the thinner and thicker stages after the information caused by global deformation is removed using both experimental point and surface coefficient methods, but the results shown in surface coefficient method demonstrates clearer and more direct. Figure 6.15 show that additional fringes are generated by the point coefficient method in the thicker area which obscures the 20 mm-diameter defect in the lower left corner. The true correlation coefficient is affected by the sample's geometry. The experimental surface approach, with its location-dependent coefficient, can account for multiple areas of different thicknesses, while the experimental point method uses a single value for the correlation coefficient. Using point approach, the maximum phase frequently occurs in the thinner portion of the CP specimen, which results in extra fringes generated on the thicker side.

The results show that both experimental coefficient methods are suitable for most cases, but the efficacy of the experimental point coefficient method is limited in the case of more complex deformation conditions. Although more computationally intensive, the experimental surface coefficient method is recommended when dealing with complex.

6.5.2 Effect of the proposed methodology on the visibility and size of defects

In this section, the effect of the proposed experimental coefficient methods on the visibility and size of defects is discussed. It is important to remark that the main objective of this novel methodology is to facilitate the non-destructive detection of small defects in substrates with both uniform (point method) and non-uniform (surface method) material properties (or thickness), rather than to improve the visibility of already-detectable defects.

These new approaches assume that the loads (both the small and the relatively large loads) are within the elastic range and that the deformation is linear. This is true because of the nondestructive nature of the testing. According this assumption, a linear coefficient C (in the point method) or $C_{(i,j)}$ (in the surface method) should exist. Starting from the two shearograms corresponding to the small and relatively large loads, the information from global deformation is removed by subtracting the phase of the shearogram generated with the small load Δ_S multiplied by the coefficient C from the one obtained by the relatively large load Δ_L, as shown in the equation (6.4)

$$\Delta_{\text{defect}} = \Delta_L - \Delta_s \cdot C \qquad (6.4)$$

Taking the point method as the example, C is the coefficient of the sample in the global deformation area. The area of a defect has its own coefficient, let's denote it as C_d. C_d could be liner or nonlinear depending the strain concentration severity, but it is different from C due to different characteristics caused by the defect. When the operation as shown in equation (6) is conducted, the global deformation is removed, but the defect information in the defect area is not eliminated because the global deformation coefficient C is used, which is different from the coefficient C_d of the defect area. This subtraction does not change the size of the defect shown in the large-load shearogram, but it could reduce the density of the fringes shown in the large-load shearogram. When the novel approaches are used in real applications, two different scenarios may arise.

6.5.2.1 Scenario 1 – Moderate and Small Defects

In the first case, the defect in the large-load shearogram is identified by a distinct fringe pattern, while it may be barely visible (in the form of a subtle phase change) in the small-load shearogram. This is the case for defects in the upper left corner and lower right corner in large and small-load shearograms of Figure 6.14a and 6.14b. However, even after multiplication by the experimental coefficient and subtraction from the large-load shearogram, the defect information is retained, as shown in Figure 6.16. Obviously, the developed experimental methods are well suited for the visualization of small defects.

6.5.2.2 Scenario 2 - Severe Defects

In the second case, due to the size and severity of the defects, distinct fringes already appear in the small-load shearogram. Multiplying the small-load shearogram by the experimental coefficient enhances the fringes; once it is subtracted from the large-load shearogram, the density of the fringe pattern decreases, but without negatively affecting the detectability of the defects. That is why the three largest defects in the diagonal direction (Figure 6.14a) show fringe patterns with decreased density in Figure 6.16. This phenomenon becomes more obvious for large defects that already appear in the small-load shearogram. Therefore, the novel approaches are suited for nondestructive testing, especially for visualization of small defects, but not for quantitative strain measurement in defect areas.

6.6 Conclusion

Two novel experimental methods capable of removing the information caused by global deformation in digital shearographic NDT are developed. The detection of small defects is improved and the sensitivity of digital shearography is successfully enhanced. The experimental point and surface coefficient methods significantly streamline the detection process of small and large defects that are typically masked fringe patterns by the substrate's global deformation or by more complex deformation. Both novel approaches generate reliable and repeatable results, facilitating defect detection also for less experienced operators. To validate the proposed methods, defects of various sizes are fabricated on two samples: an aluminum disc of uniform thickness and a composite laminate with a 3 mm-thick step. The study's findings demonstrate that the proposed methods is an effective and practical method in terms of (a) detection of smaller defects and (b) applicability to samples with more complex deformation. Furthermore, the experimental point and surface methods are verified using pressure and thermal loading, proving that the suggested approaches are not limited to a specific loading method or material type. The results show that the experimental point coefficient method is suitable for most situations but is relatively insensitive to delaminations because it uses a single value of correlation coefficient. In contrast, the experimental surface coefficient method is more suitable for processing complex deformations because its coefficient varies across the surface, but it is more computationally intensive. Finally, the methodology developed in this study is also applicable to digital holography, electrical speckle pattern interferometry, and other technologies that rely on fringe patterns to record information from deformation.

CHAPTER SEVEN

CONCLUSION

This article reports on a series of new developments in digital shearography to determine and improve defect detection capability. Although digital shearography technology has conventionally been best known for its application in non-destructive testing of composite materials, with the recent development of the technology itself for different application purposes, the application of digital shearography technology is no longer limited to non-destructive testing or only suitable for composite materials. At present, the application of digital shearography technology has been widely used in non-destructive testing of non-composite materials, strain measurement, vibration measurement and other fields. Digital shearography is detection technology with full-field, non-destructive and non-contact advantages. Compared with digital holography technology, it has better anti-interference performance. At present, this technology has been widely used to detect internal defects of various materials and components and surface stress and strain of materials. It is reasonable to predict that digital shearography technology will see more and more developments in the near future, both in terms of the technology itself and its applications.

This research studies the defect detection capabilities of digital shearography. Aiming at improving the sensitivity and visibility of defect of digital shearography by eliminating global deformation under fixed conditions. The research work of this article mainly includes the following contents:

First, the development history of digital shearography interference technology is introduced, and its value and importance in practical applications are introduced. The current research status of information processing technologies such as phase acquisition of digital shearography is introduced and put forward the problems existing in digital shearography, as well as new technical requirements. Secondly, the speckle generation and its distribution characteristics are introduced, the principle of digital shearography is introduced in detail, and two commonly used phase extraction methods are analyzed, namely the temporal phase shift method and the spatial phase shift method. It also introduces common methods for processing detection results obtained by digital shearography optical paths and introduces the advantages and disadvantages of these methods. Next, the elastic deformation theory of thin plates is described, the relationship between deformation and magnitude of loading is introduced in detail, and the differences in the relationship between deformation and loading of thin plates of different shapes are described.

In the following step, the numerical and experimental study of digital shearography for determining the size of the smallest detectable defect and the relationship with different parameters has been conducted. Numerical models to detect defects close to surface (usually, the defect depth t is smaller than 1/5 to 1/8 size of defect) and to determine the size of the smallest detectable defect by shearography under a vacuum and a pressure loading have been developed which provides experimental background information for testing engineers before starting their investigations. The comprehensive numerical models developed show that higher sensitivity for deformation measurement by shearography, less rigid material, larger loading magnitude, and shallower defects can lead to finding smaller defects. Of these four parameters, the most significant impact on defect inspection is the depth of the defect. An increase in the depth of the defect will obviously lead to more difficulty in finding the defect. The other three parameters: sensitivity for measuring deformation, material properties, and load magnitude, have the same weight for defect inspection and less impact than the defect depth t. This is because the size of the smallest detectable defect S is proportional to one-quarters power of each of the three parameters, but three-quarters the power of the defect depth t. The experimental validation of shearography demonstrated a very good agreement with the numerical models developed, which shows that the numerical models are a promising method to provide useful estimation for NDT by digital shearography. The models established can be used to assist in the shearography inspection by estimating the size and depth of the smallest detectable defect with the corresponding load magnitudes.

Afterwards, to improve the visibility of small defect of digital shearography technology under fixed conditions, various conventional methods for eliminating global deformation are summarized, and the deficiencies of each method and the direction for improvement are proposed. Also, based on the conventional polynomial regression equation fitting method, a segmented fitting method is proposed. This method proves that defective information can be effectively preserved by fitting the global deformation in the fringe pattern. After verification by the acting method, the method is reproducible and allows non-expert operators to find defect information through visual defect inspection. Furthermore, the proposed method is not limited by loading method or material type. However, this method does not work well when the fringe quality is not clear, and a more accurate pre-filtering algorithm is needed. Finally, a feasible method is provided to use digital shearography to quickly determine the location of defects and the scope of non-destructive testing defects.

After that, two novel experimental methods capable of removing the information caused by global deformation information recorded by digital shearography are developed. The detection of small defects is improved and the sensitivity of digital shearography is successfully enhanced. The experimental point and surface coefficient methods significantly streamline the detection process of small and large defects that are typically masked fringe patterns by the substrate's global deformation or by more complex deformation. Both novel approaches generate reliable and repeatable results, facilitating defect detection also for less experienced operators. To validate the proposed methods, defects of various sizes are fabricated on two samples: an aluminum disc of uniform thickness and a composite laminate with a 3 mm-thick step. The section's results demonstrate that the proposed methods outperform the conventional numerical fitting method in terms of (a) small defect information accuracy, (b) defect detection capability, and (c) applicability to samples with more complex deformation. Furthermore, the experimental point and surface methods are verified using pressure and thermal loading, proving that the suggested approaches are not limited to a specific loading method or material type. The results show that the experimental point coefficient method is suitable for most situations but is relatively insensitive to delaminations because it uses a single value of correlation coefficient. In contrast, the experimental surface coefficient method is more suitable for processing complex deformations because its coefficient varies across the surface, but it is more computationally intensive. In summary, the novel experimental coefficient methods take one more measurement than conventional digital shearography during the loading process, thus preventing errors brought on by different loading techniques and/or substrate materials. This technology captures defective information quickly, accurately, and practically. Moreover, also due to its direct processing of the shearograms, rather than of the unwrapped phase diagram, it greatly outperforms conventional methods, while offering an effective way to rapidly (and non-destructively) determine the position and extent of defects. Also, the methodology developed in this study is also applicable to digital holography, electrical speckle pattern interferometry, and other technologies that rely on fringe patterns to record information from deformation.

In conclusion, due to the rapid development of fast and simple defect detection capabilities based on digital shearography, it is believed that digital shearography technology will be favored by more and more industries. Also, it can be reasonably predicted that digital shearography technology will see more and more developments in the near future, both in terms of the technology itself and its applications.

REFERENCES

1. Hyetch, M., et al., Nanoscale holographic interferometry for strain measurements in electronic devices. Nature, 2008. 453(7198): p. 1086-9.

2. Mohanty, R.K., et al., Speckle interferometric measurement of displacement, slope, and curvature (A). Proceedings of the National Academy of Sciences, 2001. 98(6): p. 3410-3415.

3. Ding, H., et al., Warpage measurement comparison using shadow Moire and projection Moire methods. IEEE Transactions on Components & Packaging Technologies, 2003. 25(4): p. 714-721.

4. R. Zoughi, Microwave Non-Destructive Testing and Evaluation, Kluwer Academic Publishers, the Netherlands, 2000.

5. L.J. Bond and M. Punjani, Review of some recent advances in quantitative ultrasonic NDT, IEE Proceedings A (Physical Science, Measurement and Instrumentation, Management and Education, Reviews), 1984, Volume 131, Issue 4, p. 265 –274, DOI: 10.1049/ip-a-1.1984.0039.

6. S.I. Ganchev, R.J. Runser, N. Qaddoumi, E. Ranu, G. Carriveau, Microwave nondestructive evaluation of thick sandwich composites, Materials Evaluation, 1995 Volume 53, Issue 4, p. 463-467.

7. J.N. Butters, Application of ESPI to NDT, Optics & Laser Technology, 1977, Volume 9, Issue 3, p. 117-12s.

8. Y. Y. Hung, Shearography: A New Optical Method for Strain Measurement and Nondestructive Testing, Optical Engineering, 1982, 21(3), 213391; https://doi.org/10.1117/12.7972920.

9. W. Steinchen, L. Yang, G. Kupfer, Digital shearography for nondestructive testing and vibration analysis, Experimental techniques, 1997, 21 (4), p. 20-23.

10. L. Yang, W. Steinchen, M. Schuth, and G. Kupfer, Precision measurement and nondestructive testing by means of digital phase shifting speckle pattern and speckle pattern shearing interferometry, Measurement, 1995, 16 (3), p. 149-160.

11. Clemente Ibarra-Castanedo, Stefano Sfarra, Dario Ambrosini, Domenica Paoletti, Abdelhakim Bendada, and Xavier Maldague, Diagnostics of panel

paintings using holographic interferometry and pulsed thermography, Quantitative InfraRed Thermography Journal, 2010, Volume 7, Issue 1, p. 85-114.

12. D. Balageas, X. Maldague, D. Burleigh, V. P. Vavilov, B. Oswald-Tranta, J. M. Roche, C. Pradere, G. M. Carlomagno, Thermal (IR) and Other NDT Techniques for Improved Material Inspection, J Nondestruct Eval (2016) 35:18, DOI 10.1007/s10921-015-0331-7.

13. Xu, N., Xie, X., Harmon, G., Gu, R., & Yang, L. (2012). Quality inspection of spot welds using digital shearography. SAE International Journal of Materials and Manufacturing, 5(1), 96-101.

14. Chen, X., Yang, L., Xu, N., Xie, X., Sia, B., & Xu, R. (2014). Cluster approach based multi-camera digital image correlation: Methodology and its application in large area high temperature measurement. Optics & Laser Technology, 57, 318-326.

15. Frank Chen, G. M., & Mumin, S. (2000). Overview of three-dimensional shape measurement using optical methods. Optical Engineering, 39, 10-21.

16. Yan, P., Sun, F., Dan, X., Zhao, Q., Wang, Y., & Lu, Y. (2019). Spatial phase-shift digital shearography for simultaneous measurements in three shearing directions based on adjustable aperture multiplexing. Optical Engineering, 58(5), 054105.

17. Zhao, Q., Dan, X., Sun, F., Wang, Y., Wu, S., & Yang, L. (2018). Digital shearography for NDT: phase measurement technique and recent developments. Applied Sciences, 8(12), 2662.

18. Steinchen, W., Yang, L. X., Kupfer, G. A., Mäckel, P., & Vössing, F. (1998). Strain analysis by means of digital shearography: potential, limitations and demonstration. The Journal of Strain Analysis for Engineering Design, 33(2), 171-182.

19. Z.W. Liu, J. X. Gao, H. M. Xie, P. Wallace, NDT capability of digital shearography for different materials, Optics and Lasers in Engineering, Vol. 49 (12), 2011, P. 1462-1469.

20. B. Zhang, X. Zheng, W. Xu, L. Yang, Overview of digital shearography for NDT, Materials Evaluation Vol. 78 (3), 2020, p. 343-351.

21. Moore, A.J. and J.R. Tyrer, An Electronic Speckle Pattern Interferometer for Complete in Plane Displacement Measurement. Measurement Science & Jingbo and Zhang, Two-dimensional in-plane electronic speckle pattern

interferometer and its application to residual stress determination. Optical Engineering, 1998. 37(8): p. 2402-2409.

22. Rabal, H., R. Henao, and R. Torroba, Digital speckle pattern shearing interferometry using diffraction gratings. Optics Communications, 1996. 126(4-6): p. 191-196.

23. Yang, L., Digital Shearography: Theory and Application of Digital Speckle Pattern Shearing Interferometry. 2003.

24. Y.Y. Hung, Shearography: A novel and practical approach for nondestructive inspection, Journal of Nondestructive Evaluation, Vol 8, 1989, p. 55–67.

25. F. Taillade, M. Quiertant, K. Benzarti, C. Aubagnac, Chapter 20: Non-destructive evaluation (NDE) of composites: using shearography to detect bond defect, in book "Non-Destructive Evaluation (NDE) of Polymer Matrix Composites," edited by Vistasp M. Karbhari, Woodhead Publishing Series in Composites Science and Engineering, 2013, p. 542-556, 557e, ISBN 0-85709-344-4.

26. C. Petry, M. Schuth, Spatial phase shift shearography for enhanced NDT. NDT E. Int. 2018. SHM-NDT 2018. Available online: https://www.ndt.net/article/shmndt2018/papers/SHM-NDT-2018_paper_39.pdf (accessed on 4 January 2022).

27. L. Yang, F Chen, W Steinchen, MY Hung, Digital shearography for nondestructive testing: potentials, limitations, and applications, Journal of Holography and Speckle 2004, 1 (2), p. 69-79.

28. E.C. Krutul, R.M. Groves, Opto-mechanical modelling and experimental approach to the measurement of aerospace materials using shearography and thermal loading. In: Bodermann B, editor. Model. Asp. Opt. Metrol. III, vol. 8083, SPIE; 2011, p. 434–442.

29. G. De Angelis, M. Meo, D.P. Almond, S.G. Pickering, S.L. Angioni, A new technique to detect defect size and depth in composite structures using digital shearography and unconstrained optimization. NDT&E Int 2012, 45(1), p. 91–96.

30. D. Akbari, N. Soltani, M. Farahani. Numerical and experimental investigation of defect detection in polymer materials by means of digital shearography with thermal loading. Proc Inst Mech Eng Part B J Eng Manuf, 2013, 227(3), p. 430–442.

31. X. Chen, M. Khaleghi, I. Dobrev, W. Tie, and C. Furlong, Structural Health

Monitoring by Laser Shearography: Experimental and Numerical Investigations, Experimental and Applied Mechanics, Volume 6, 2015, pp 149–155, Proceedings of the 2014 Annual Conference on Experimental and Applied Mechanics.

32. F. Yang, X. Ye, Z. Qiu, B. Zhang, P. Zhong, Z. Liang, et al. The effect of loading methods and parameters on defect detection in digital shearography. Results Phys, 2017, 7, p. 3744-3755.

33. J.F. Vandenrijt, H. Xiong, C. Lequesne, P. Blain, Georges M. Shearography inspection of monolithic CFRP composites: finite element modeling approach for assessing an adequate strategy of artificial defects representing delamination. In: Lehmann P, Osten W, Jr. AAG, editors. Opt. Meas. Syst. Ind. Insp. XI, vol. 11056, SPIE; 2019, p. 107–13.

34. Zheng, X., Guo, B., Fang, S., Sia, B., & Yang, L. (2023). Development of Digital Shearography for Dual Sensitivity Simultaneous Measurement Using Carrier Frequency Spatial Phase Shift Technology (No. 2023-01-0068). SAE Technical Paper.

35. Zhang, B., Zheng, X., Guo, B., Fang, S., Sia, B., & Yang, L. (2022). Sagnac interferometer based digital shearography for simultaneous dual sensitivity measurement. Optics and Lasers in Engineering, 152, 106984.

36. Guo, B., Zheng, X., Gerini-Romagnoli, M., & Yang, L. (2023). Digital shearography for NDT: Determination and demonstration of the size and the depth of the smallest detectable defect. NDT & E International, 139, 102927

37. Lopes, H., Ferreira, F., Dos Santos, J. A., & Moreno-García, P. (2014). Localization of damage with speckle shearography and higher order spatial derivatives. Mechanical Systems and Signal Processing, 49(1-2), 24-38.

38. Pandey, A. K., Biswas, M., & Samman, M. M. (1991). Damage detection from changes in curvature mode shapes. Journal of sound and vibration, 145(2), 321-332.

39. W. Lestari and P.Z. Qiao, "Damage detection of fiber-reinforced polymer honeycomb sandwich beams". Composite Structures. 67(3): 365-373, 2005.

40. W. Lestari, P.Z. Qiao, and S. Hanagud, "Curvature mode shape-based damage assessment of carbon/epoxy composite beams". Journal of Intelligent Material Systems and Structures. 18(3): 189-208, 2007

41. N.M.M. Maia, J.V. Araújo dos Santos, R.P.C. Sampaio, and C.M.M. Soares. "Damage Identification Using Curvatures and Sensitivities of Frequency

Response-Functions". in The Third European Workshop On Structural Health Monitoring. Granada, Spain: 547-554, 2006.

42. Hofmann, D., Pandarese, G., Revel, G. M., Tomasini, E. P., & Pezzoni, R. (2008). Optimization of the excitation and measurement procedures in nondestructive testing using shearography. Review of Scientific Instruments, 79(11).

43. Tao, N., Anisimov, A. G., & Groves, R. M. (2022). Shearography non-destructive testing of thick GFRP laminates: Numerical and experimental study on defect detection with thermal loading. Composite Structures, 282, 115008

44. Deepan, B., Quan, C., & Tay, C. J. (2016). Determination of slope, curvature, and twist from a single shearography fringe pattern using derivative-based regularized phase tracker. Optical Engineering, 55(12), 121707-121707.

45. Fomitchov, P., Wang, L. S., & Krishnaswamy, S. (1997). Advanced image-processing techniques for automatic nondestructive evaluation of adhesively-bonded structures using speckle interferometry. Journal of nondestructive evaluation, 16, 215-227.

46. Tao, N., Anisimov, A. G., & Groves, R. M. (2022). FEM-assisted shearography with spatially modulated heating for non-destructive testing of thick composites with deep defects. Composite Structures, 297, 115980.

47. Hofmann, D., Pandarese, G., Revel, G. M., Tomasini, E. P., & Pezzoni, R. (2008). Optimization of the excitation and measurement procedures in nondestructive testing using shearography. Review of Scientific Instruments, 79(11).

48. Templeton, D. W., & Hung, Y. Y. (1989). Shearographic fringe carrier method for data reduction computerization. Optical Engineering, 28(1), 30-34

49. M. Takeda, Q. Gu, M. Kinoshita, H. Takai, and Y. Takahashi. “Frequencymultiplex Fourier-transform profilometry: a single-shot three-dimensional shape measurement of objects with large height discontinuities and/or surface isolations.” Appl. Opt., 36(22), 5347-5354 (1997).

50. E. Kolenovic, W. Osten, R. Klattenhoff, S. Lai, C. V. Kopylow, and W.Juptner.“Miniaturized digital holography sensor for distal three-dimensional endoscopy.” Appl. Opt., 42(25), 5167-5172 (2003).

51. X. L. Gong, S. Toyooka. “Investigation on mechanism of plastic deformation by digital speckle pattern interferometry.” Exp Mech, 39(1), 25-29 (1999).

52. G Restivo, G. L. Cloud, R. Beaudry, and B. B. Raju., “3-D Strain fields using embedded DSPI: pilot study.” Proceedings of the 2004 SEM X International Congress and Exposition on Experimental and Applied Mechanics, 178-185 (2004).

53. S. H. Baik, S. K. Park, C. J. Kim, and S. Kim. “Two-channel spatial phase shifting electronic speckle pattern interferometer.” Opt. Commun., 192(3), 205-211 (2001). 170

54. J. Burke, H. Helmers. “Performance of spatial vs. temporal phase shifting in ESPI.” Proc. SPIE, 3744(99), 188-199 (1999).

55. J. Burke, H. Helmers, C. Kunze, and V. Wilkens. “Speckle intensity and phase gradients: influence on fringe quality in spatial phase shifting ESPI-system s.” Opt. Commun., 152(1), 144-152(1998).

56. C. J. Tay, Y. Fu. “Determination of curvature and twist by digital shearography and wavelet transforms.” Opt. Lett., 30(21), 2873-2875 (2005).

57. T. Kreis. “Digital holographic interference-phase measurement using the Fouriertransform method.” J. Opt. Soc. Am. A, 3(6), 847-855 (1986).

58. K. A. Haines, B. P. Hildebrand. “Surface-deformation measurement using the wavefront reconstruction technique.” Appl. Opt., 5 (4), 595-602 (1966).

59. Y. Fu, M. Guo, H. Liu. “Determination of instantaneous curvature and twist by digital shearography.” Opt. Eng., 51(8), 083602-1 (2012).

60. G. Pedrini, Y. L. Zou, H. J. Tiziani. “Quantitative evaluation of digital shearing interferogram using the spatial carrier method.” Pure Appl. Opt.: Europ. Opt. Soc. P. A., 5(3), 313(1999).

61. G. Pedrini, W. Osten, M. E. Gusev. “High-speed digital holographic interferometry for vibration measurement.” Appl. Opt., 45(15), 3456-3462 (2006).

62. C. Kohler, M. R. Viotti, G. A. Albertazzi. “Measurement of three-dimensional deformations using digital holography with radial sensitivity.” Appl. Opt., 49(20), 4004-4009 (2010). 171

63. B. Bhaduri, N. K. Mohan, M. P. Koyhiyal. “Simultaneous measurement of out-ofplane displacement and slope using a multiaperture DSPI system and fast Fourier transform.” Appl. Opt., 46(23), 5680-5686 (2007).

64. G. Pedrini, Y. L. Zou, H. J. Tiziani. “Simultaneous quantitative evaluation of inplane and out-of-plane deformations by use o f a multidirectional spatial carrier.” Appl. Opt., 36(4), 786-792 (1997).

65. S. Schedin, G. Pedrini, H. J. Tiziani, and F. M. Santoyo. “Simultaneous three-dimensional dynamic deformation measurements with pulsed digital holography.” Appl. Opt., 38(34), 7056-7062 (1999).

66. B. Bhaduri, N. K. Mohan, M. P. Kothiyal, and R. S. Sirohi “Use of spatial phase shifting technique in digital speckle pattern interferometry (DSPI) and digital shearography (D S).” Opt. Express, 14(24), 11598-11607 (2006).

67. X. Xie, N. Xu, J. F. Sun, Y. Wang and L. Yang. “Simultaneous measurement of deformation and the first derivative with spatial phase-shift digital shearography.” Opt. Commun., 286(1), 277-281(2012).

68. X. Xie, L. X. Yang, N. Xu, and X. Chen. “M ichelson interferometer based spatial phase shift shearography.” Appl. Opt., 52(17), 4063-4071 (2013).

69. X. Xie, Y. Zheng, X. Li, B. Sia, P. Zhong, G. Yang, and L. Yang. “Spatial PhaseShift Digital Shearography for Out-of-Plane Deformation Measurement.” SAE Int. J. Mater. Manf., 7(2), 402-405 (2014).

70. Zhong, S., Sun, F., Wu, S., Bao, F., & Wang, Y. (2020). Multi-directional shearography based on multiplexed Mach–Zehnder interference system. Journal of Modern Optics, 67(4), 346-354.

71. Khodada, D., et al., Full-field 3D deformation measurement: comparison between speckle phase and displacement evaluation. Appl Opt, 2016. 55(27): p. 7735-7743.

72. Wang, L.S., et al., Measurement of three-dimensional surface shape and deformations using phase stepping speckle interferometry. Optical Engineering, 1996. 35(8): p. 2333-2340.

73. Yang, L. and X. Xie, Principles of Temporal Phase Shift Shearography. 2016.

74. Xie, X., et al., Review and Comparison of Temporal- and Spatial-Phase Shift Speckle Pattern Interferometry for 3D Deformation Measurement. Proceedings of SPIE - The International Society for Optical Engineering, 2013. 8916.

75. Jiancheng, et al., Algorithm for multiple-beam Fizeau interferograms with arbitrary phase shifts. Optics Express, 2008.

76. Pedrini, G., W. Osten, and M.E. Gusev, High-speed digital holographic interferometry for vibration measurement. Applied Optics, 2006. 45(15): p. 3456-62.

77. Pedrini, Zou, and Tiziani, Simultaneous quantitative evaluation of in-plane and out-of-plane deformations by use of a multidirectional spatial carrier. Applied Optics, 1997.

78. Pedrini, G., Y.-L. Zou, and H.J. Tiziani, Quantitative evaluation of digital shearing interferogram using the spatial carrier method. Pure & Applied Optics Journal of the European Optical Society Part A, 1996. 5(3): p. 313.

79. Tang, C., et al., Denoising by coupled partial differential equations and extracting phase by backpropagation neural networks for electronic speckle pattern interferometry. Applied Optics, 2007. 46(30): p. 7475-84.

80. Aebischer, H.A. and S. Waldner, Simple and effective method for filtering speckle-interferometric phase fringe patterns. Optics Communications, 1999. 162(4): p. 205-210.

81. Bracewell, R.N. and Bracewell, R.N., 1986. The Fourier transform and its applications New York: McGraw-Hill.1999, Vol. 3. pp. 267-272

82. M. R. Viotti, G. Albertazzi Jr,"Robust speckle metrology for stress measurements outside the lab", Proc. SPIE Optical Metrology, International Society for Optics and Photonics, 95250T-95250T(2015)

83. Tang, C., et al., Denoising by coupled partial differential equations and extracting phase by backpropagation neural networks for electronic speckle pattern interferometry. Applied Optics, 2007. 46(30): p. 7475-84.

84. Aebischer, H.A. and S. Waldner, Simple and effective method for filtering speckle-interferometric phase fringe patterns. Optics Communications, 1999. 162(4): p. 205-210.

85. Da′vila and Abundio, Scale-space filter for smoothing electronic speckle pattern interferometry fringes. Optical Engineering, 1996. 35(12): p. 3549-3554.

86. Wang, J., Mao, Y. Q., Li, S. J., & Wu, C. H. (2012). Frequency domain reciprocal-aussian cascade low-pass filtering denoising method of image. Jisuanji Yingyong Yanjiu, 29(12), 4775-4778.

87. Bone, D.J., Fourier fringe analysis: the two-dimensional phase unwrapping problem. Applied Optics, 1991. 30(25): p. 3627-32.

88. Flynn, T.J., Two-dimensional phase unwrapping with minimum weighted discontinuity. Journal of the Optical Society of America A, 1997. 14(10): p. 2692-2701.

89. Xin Xie "Development of michelson interferometer based spatial phase-shift digital shearography" Oakland University

90. Lowe, P. G. (2012). Basic principles of plate theory. Springer Science & Business Media

91. L. Yang, W. Steinchen, M. Schuth, G. Kupfer, Noch präziser zerstörungsfrei Prüfen-Anwendung der Phasenschiebetechnik in der elektronischen Shearografie, Technica 11, 1995, p. 19-22.

92. D. Francis, R.P. Tatam, and R.M. Groves, Shearography technology and applications: a review, Measurement Science and Technology, 2010, Volume 21, Number 10, 102001.

93. Y. K. Zhu, G.Y. Tian, R.S. Lu, and H. Zhang, A Review of Optical NDT Technologies, Sensors, 2011, 11(8), 7773-7798; https://doi.org/10.3390/s110807773.

94. M.A. Abou-Khousa, A. Ryley, S. Kharkovsky, R. Zoughi1, D. Daniels, N. Kreitinger, and G. Steffes, Comparison of X-Ray, Millimeter Wave, Shearography and Through-Transmission Ultrasonic Methods for Inspection of Honeycomb Composites, AIP Conference Proceedings 894, 999 (2007); https://doi.org/10.1063/1.2718076.

95. L. Yang, and Y.Y. Hung, Digital shearography for nondestructive evaluation and application in automotive and aerospace industries, Proceedings of the 16th WCNDT, Montreal, Canada, 2004; http://www.ndt.net/article/wcndt2004/pdf/optical_techniques/534_yang.pdf.

96. W Steinchen, L. Yang, G Kupfer, P Mäckel, Non-destructive testing of aerospace composite materials using digital shearography, Proceedings of the Institute of Mechanical Engineers, Part G. Journal of Aerospace Engineering, Vol. 212 (1), 1998, p. 21-30, https://doi.org/10.1243/0954410981532108.

97. L. Yang and X. Xie, Digital Shearography: New developments and Applications, SPIE Press, 2016, Bellingham, WA, USA.

98. L. Yang and T. Siebert, Chapter 22: Digital Speckle Interferometry in Engineering, p. 405-440, in the book entitled "New Directions of Holography and Speckles," edited by H. J. Caulfield and C. Vikram, American Scientific

Publishers (ASP), 2008, ISBN: 1-58883-101-9.

99. D. Francis, Chapter 4: Non-destructive evaluation (NDE) of composites: introduction to shearography, in book "Non-Destructive Evaluation of Polymer Matrix Composites," edited by Vistasp M. Karbhari, Woodhead Publishing Series in Composites Science and Engineering, 2013, p. 56 – 83, ISBN 0-85709-344-4.

100. M. Y. Hung, L. Yang and Y.H. Huang, Chapter 5: Nondestructive evaluation (NDE) of composites: Digital Shearography, in book "Non-Destructive Evaluation of Polymer Matrix Composites," edited by Vistasp M. Karbhari, Woodhead Publishing Series in Composites Science and Engineering, 2013, p. 84-115, ISBN 0-85709-344-4.

101. John W. Newman, 7.13 Shearography Nondestructive Testing of Composites in book "Reference Module in Materials Science and Materials Engineering: Comprehensive Composite Materials II," Elsevier, Volume 7, 2018, Pages 270-290, https://doi.org/10.1016/B978-0-12-803581-8.10046-3.

102. L. Yang and J. Li, Chapter 13: Shearography, in "Handbook of Advanced Non-Destructive Evaluation," edited by N. Ida, N. Meyendorf (eds.), Springer International Publishing AG, 2019, p. 383 – 420.

103. S. Timooshenko and W. S. Krieger, Theory of plates and Shells, McGraw-Hill Book Company, Inc., New York (1959).

104. Longfu Wang, Elastic Mechanics, Science Press of China, 137 Chaoyangmen Inner Street, Beijing (1979) (Chinese)

105. L. Yang, Grundlagen und Anwendungen der Phasenschiebe-Shearografie zur Zerstorungs-freien Werkstoffprufung, Dehnungsmessung und Schwingungsanalyse, PhD thesis, University of Kassel, Germany; Fortschritt-Berichte VDI, 1998, 8, 682

106. C. W. Bert, A Critical Evaluation of New Plate Theories Applied to Laminated Composites, Composite Structures, 1984, Vol 2(4), pp. 329-347

107. Y. Y. Hung and H. P. Ho, "Shearography: an optical measurement technique and applications" Materials science and engineering R-Report 49(3), 61-87 (2005).

108. B. Liu, Q. Wei, J. Tu, D.D. Arola, D. Zhang, Inspection of the interior surface of cylindrical vessels using optic fiber shearography, Meas. Sci. Technol. (2017), https://doi.org/10.1088/1361-6501/aa70d6.

109. C. Dong, K. Li, Y. Jiang, D. Arola, D. Zhang, Evaluation of thermal expansion

coefficient of carbon fiber reinforced composites using electronic speckle interferometry, Opt. Express. (2018), https://doi.org/10.1364/oe.26.000531.

110. W.L. Lai, S.C. Kou, C.S. Poon, W.F. Tsang, S.P. Ng, Y.Y. Hung, Characterization of defects embedded in externally bonded CFRP on concrete beams by infrared thermography and shearography, J. Nondestruct. Eval. 28 (2009) 27–35, https:// doi.org/10.1007/s10921-009-0044-x.

111. Y. Ye, K. Ma, H. Zhou, D. Arola, D. Zhang, An automated shearography system for cylindrical surface inspection, Meas. J. Int. Meas. Confed. (2019), https://doi.org/ 10.1016/j.measurement.2018.11.085.

112. Nsengiyumva W, Zhong S, Lin J, Zhang Q, Zhong J, Huang Y. Advances, limitations and prospects of nondestructive testing and evaluation of thick composites and sandwich structures: A state-of-the-art review. Compos Struct 2021;256:112951.

113. Ibrahim ME. Nondestructive evaluation of thick-section composites and sandwich structures: a review. Compos A Appl Sci Manuf 2014;64:36–48.

114. J. Gryzagoridis, D. Findeis, N.B. Vukeya, Vacuum excitation in shearographic NDT, Insight Non-Destructive Test. Cond. Monit. 49 (2007) 98–101, https://doi.org/ 10.1784/insi.2007.49.2.98.

115. Mallick, P.K.: Composites Engineering Handbook. M. Dekker, New York (1997)

116. Silberschmidt, V.: Dynamic Deformation, Damage and Fracture in Composite Materials and Structures. Woodhead Publishing, Duxford (2016)

117. Karbhari, V.M.: Non-Destructive Evaluation (NDE) Of Polymer Matrix Composites. Elsevier Science, Burlington (2013)

118. Kelly, A.: Comprehensive composite materials. Elsevier, Amster- 13 dam New York (2000)

119. Wang, B., Zhong, S., Lee, T.L., Fancey, K.S., Mi, J.: Nondestructive testing and evaluation of composite materials/structures: A state-of-the-art review. Adv. Mech. Eng. 12(4), 1687814020913761 (2020). https://doi.org/10.1177/1687814020. 913761

120. L.M. Lobanov, S.A. Bychkov, V.A. Pivtorak, V.Y. Derecha, V.O. Kuders'Kyi, O.M. Savyts'Ka, I. V. Kyyanets', On-line monitoring of the quality of elements of aircraft structures by the method of electron shearography, Mater. Sci. (2009). https://doi. org/10.1007/s11003-009-9186-3.

121. H. Feng, J. Zhang, X. Liu, Studies on digital shearography for testing of aircraft composite structures and honeycomb-based specimen, Appl. Mech. Mater. (2012), https://doi.org/10.4028/www.scientific.net/AMM.121-126.1264.

122. D.C. Ghiglia, M.D. Pritt, Two-Dimensional Phase Unwrapping: Theory, Algorithms, and Software, Wiley, New York, 1998, p. 493, Chapter XIV.

123. Deepan, B., Quan, C., & Tay, C. J. (2016). Determination of slope, curvature, and twist from a single shearography fringe pattern using derivative-based regularized phase tracker. Optical Engineering, 55(12), 121707-121707.

124. Guo, B., Zhang, B., Zheng, X., Fang, S., Fang, Y., Sia, B., & Yang, L. (2022). Review of shearography for dual-directional measurement. Optics, 3(2), 117-137.

125. Tay, C. J., & Fu, Y. (2005). Determination of curvature and twist by digital shearography and wavelet transforms. *Optics letters*, *30*(21), 2873-2875.

126. Blain, P., Michel, F., Piron, P., Renotte, Y., & Habraken, S. (2013). Combining shearography and interferometric fringe projection in a single device for complete control of industrial applications. *Optical Engineering*, *52*(8), 084102-084102.2

127. Abdo, M. B., & Hori, M. (2002). A numerical study of structural damage detection using changes in the rotation of mode shapes. Journal of Sound and vibration, 251(2), 227-239.

128. Steinchen, W., Yang, L., Schuth, M., & Kupfer, G. (1994). Precision measurement and nondestructive testing by means of the speckle and speckle-shearing interferometry. VDI BERICHTE, 1118, 27-27.

129. Yang, L., Zhang, P., Liu, S., Samala, P. R., Su, M., & Yokota, H. (2007). Measurement of strain distributions in mouse femora with 3D-digital speckle pattern interferometry. Optics and lasers in engineering, 45(8), 843-851.

130. Yang, L., Xie, X., Xu, N., & Chen, X. (2019). Spatial phase-shift shearography system for non-destructive testing and strain measurement." U.S. Patent No. 10,330,463. 25.

131. Shearography, Chapter 13 of “Handbook of Advanced Non-Destructive Evaluation (ISBN 978-3-319-30122-8)” By Lianxiang Yang and Junrui Li published in 2019 by Springer Nature Switzerland AG, Switzerland.

132. Zheng, X., Fang, S., Guo, B., Sia, B., & Yang, L. (2023). Development of Simultaneous Dual-Resolution Digital Holography System. Applied Sciences, 13(5), 2856.